Calculation and Measurement of the Rayleigh Scattering Length of the Scintillation Wavelength of Liquid Argon for Dark Matter and Neutrino Detectors

by

Emily Grace

Supervised by: Professor Jocelyn Monroe and Dr. James A. Nikkel

A thesis submitted to the
Department of Physics
in conformity with the requirements for
the degree of Master of Science

Royal Holloway University of London
Egham, United Kingdom
November 2017

Abstract

There is wealth of evidence that the majority of the matter in the universe is composed of non-baryonic dark matter. One candidate for dark matter is weakly interacting massive particle (WIMP). There are many detectors searching for evidence of WIMP particle interaction. A common active medium is liquid argon. Argon, like all noble elements is a scintillator, meaning it produces light when exposed to radiation. Within these large, liquid argon detectors, one method of determining the significance of the event is by determining the event location. This involves a deep understanding of how the scintillation light optically propagates through the detector, including the Rayleigh scattering length. The Rayleigh scattering length of liquid argon was formerly contention, as experimental results did not agree with a theoretical calculation. We will discuss an update calculation of the wavelength dependent scattering in argon using historical measurements. These calculations were tested using an experimental test stand, designed and constructed at Royal Holloway. This will show that the scattering length of the scintillation light of liquid argon is 58 cm.

Dedication

For my daughter Esther Grace and my husband Piper Williams.

Acknowledgments

What started as an innocent curiosity grew into a consuming passion. Then I was overtaken by the darkest nightmare. Each breath contained dejection. Every exhale left me only a shadow. Still, I did not stop. Driven no longer by passion, no longer by curiosity, but by insanity. To those who loved me in my self inflicted sorrow, I thank you. Anything I have managed to accomplish would not have been possible without your support. Anything which results in failure is entirely my own doing.

I would like to first thank the teachers who invested in me all throughout my life. Good education changes the world and good educations comes from committed teachers, of which I have known many. I am especially thankful to the science and math department at Hillsborough High School who insisted I take physics and taught me not to give up in math. Your words of encouragement provide motivation for me to this day.

I am thankful for my years at Bethel College. To all those professors, especially Dr. Alan Young, who wondered why I was not studying physics, you were right. Dr. Stephanie Carlson, thank you for continued academic support and encouragement. I first learned how to do research from you.

My time at Indiana University South Bend that made me a physicist. I believe I could not have studied at a better place or with a better department. First I would like to thank the faculty, who have continued to support me though I am no longer a student. Thank you Dr. Monika Lynker for walking me through my first year of uncertainty and tears. Thank you for then pushing me to better. Thank you Dr. Jerry Hinnefeld, Dr. Henry

Scott, and Dr. R. Schimmrigk for your excellent lectures and advice. Thank you Dr. Ilan Levine, if it was not for you, I would never have studied dark matter. Thank you for giving me a chance to do research. Thank you for sending me to so many conferences. Thank you for continuing to advise me. I feel honored to be colleague.

I would like to thank the faculty at Royal Holloway for working with me. Thank you Dr. James Nikkel for teaching me the value of independence and strength in adversity.

I would also like to thank Professor Jocelyn Monroe. Thank you coming to my talk at MIT. Thank you for making it possible for me to attend RHUL and to work with DEAP. Thank you for seeing me to the end. Thank you for all of your input. I am truly grateful for all your time, input and encouragement.

I would also like to thank the support staff at RHUL. Andy, Carmella, and Gill, you all are amazing. Thank you for all your work. Thank you Ian and Michele for everything you have done. Thank you for the technical support, the emotional support, and your friendship. I can honestly say, I would not have gotten this done without you.

I would like to thank my physics friends. Thank you also to the office at RHUL for all the good times. Thank you Alistair, Gabriella, Ric, Navin, Will, Ian, Franco, and Jochem. You all are incredible at what you do and I am excited to follow your careers.

Thank you also to my students who were patient with me as combined my first year of teaching with finishing a doctoral program.

Kayleigh, you are strong, amazing woman and my physics partner in crime. You held me together when I was falling apart. I am so glad we met at IUSB. I think back of our long nights studying together so fondly. I am glad we got to do graduate school together, albeit on separate, continents and be moms together. Thank you for being my colleague and friend.

Thank you also to my home group and friends at St. John's Egham.

I would also like to thank the women who have been my friends and my support during this time. Thank you Jacquelyn for going with me to the UK. Thank you for

all the conversations. Thank you Sue for your correspondence and then later our weekly prayers. Thank you Elise for our talks. Thank you for listening to me when I was surely losing my mind.

Thank to family for putting up with me. Thank you Mom for your support. Thank you Mary for becoming one of my friends. Thank you Katherine for your prayers.

To my beloved Piper. I do not think you knew what marriage to me would entail. You followed me across the ocean. You watched me go through hell. You never stopped loving me. Then you followed me to Kansas. You cared for our daughter so that I could live in an office and travel to labs in other countries. This PhD is as much yours as it is mine.

My sweet, little daughter Esther. You are the surprise I never expected and best thing to come out of my time in England. Thank you for coos and smiles. I only wish I could have been the mother you deserved in your first year and a half of life instead of a tired, and mostly absent mess. I pray that my efforts will make me able to provide for you and my sacrifices were not in vain. Please forgive me and I will work on forgiving myself. I love you so much. Keep smiling, my strong girl.

To the Lord God, creator of all that is known and unknown and keeper of knowledge.

I praise you for seeing fit to reveal Yourself to us through the universe.

When I consider your heavens, the work of your fingers, the moon and the stars, which you have set in place, what is mankind that you are mindful of them, human beings that you care for them?

Psalm 8:3-4

Declaration of Originality

I confirm that the work presented in this thesis is my own. Where information has been derived from other sources, I confirm that this has been indicated in the document.
Signed:

Date:

Contents

List of Tables

List of Figures

Chapter 1

Dark Matter

Science progresses best when observations force us to alter our preconceptions.

- Dr. Vera Rubin

1.1 Introduction

Sir Isaac Newton is widely considered to be the father of classical physics. It has been 289 years since his death and still his formulations and concepts dominate physics classrooms throughout the world. In 1687, Newton published *PhilosophiæNaturalis Principia Mathematica* in which he described the force of gravity as the attraction between two masses [2]. This revolutionized our understanding of the Universe and cosmology. In 1702, Newton followed this with his publication *Opticks* in which he described the paths light takes through media and laid the foundation for the present field of optical physics [3]. In modern physics both these concepts are part of the search today for the mysterious dark matter particle whose presence in the Universe is indirectly detected by gravity. A particle which some search for with light-producing detectors.

The direct detection of a dark matter particle would solve one of the great mysteries in modern physics. At present there are several experiments racing to be the first to make

this historic discovery. Some of these experiments rely on sensitive detector media that might be capable of capturing a dark matter interaction by observing a particle collision. One choice for a detector media is argon, a light-producing scintillator. The original research presented in this thesis focuses on an improved calculation and measurement of the optical parameters important for understanding how scintillation light travels through argon. This knowledge is relevant for modeling and reconstructing events in liquid argon detectors employed in the search of dark matter. This includes DEAP-3600 [4], DarkSide-50 [5], ArDM [6] and the future DarkSide-20k experiments [7]. This is also relevant for experiments being developed for the DUNE long baseline neutrino oscillation program [8].

Chapter 1 is a synopsis of the evidence for dark matter in the Universe and reviews the experimental search for dark matter with a focus on experiments that utilize liquid argon as a detector medium. Chapter 2 is a detailed description of the physics of liquid argon scintillation and the propagation of scintillated light through argon. Chapter 3 details previous optical measurements in liquid argon and provides updated calculations for the attenuation length based on these previous experiments. Chapter 4 is an overview of the scattering length experiment to measure the attenuation length of the scintillation light of liquid argon conducted at Royal Holloway. Chapter 5 is an overview of the conditions of the three argon runs. Chapter 6 describes the analysis process for analyzing the data obtained from the scattering experiment. The implications of the research presented in this thesis are discussed in chapter 7.

1.2 Historical Evidence of Dark Matter

1.2.1 Galaxy Cluster Velocities

The first published evidence of an unknown mass in our Universe came from Fritz Zwicky in the 1930's [9] [10] where he proposed two different methods of measuring the mass of the Coma Cluster of galaxies, Figure 1.1. His goal was to determine the ratio of dark matter to luminous matter in a nebula. In this work, he was describing dark matter as cold stars, gasses, and solid bodies. Using Hubble's [11] work on the luminosity curves of nebulae and photographs taken with an 18 inch Schmidt telescope, he determined the amount of luminous mass. Next, he observed the velocity dispersion of the galaxies in the Coma cluster using the rotational data obtained by [12] and applying the virial theorem which is an equation that yields the time average kinetic energy of a stable system consisting of particles bound by potential forces [13]. The virial theorem is expressed mathematically as

$$\langle T \rangle = -\langle V_{tot} \rangle, \tag{1.1}$$

which relates the average kinetic energy $\langle T \rangle$, to its total graviational potential energy $\langle V_{tot} \rangle$. The model for this data is show in Figure 1.2. From this Zwicky observed that the velocity of galaxies was too large to be caused by luminous matter alone. According to his calculations, the mass-to-light ratio was around 400 solar masses per unit of solar luminosity. This finding was two orders of magnitude higher the the observation in the solar neighborhood. This indicates a large presence of dark matter.

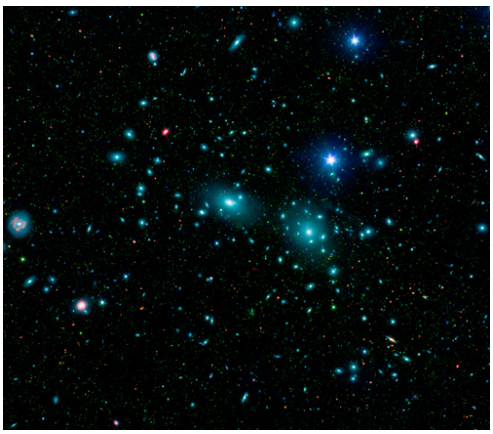

Figure 1.1: An NASA image of the coma cluster of galaxies [14].

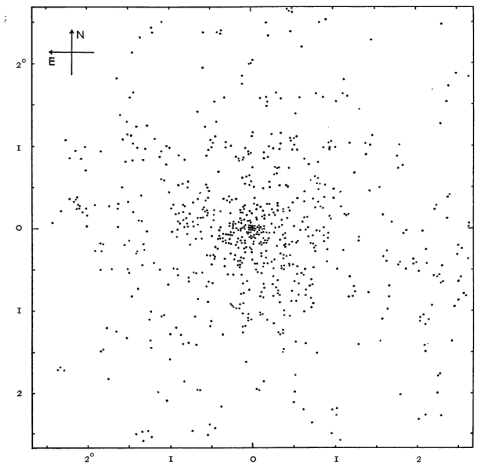

Figure 1.2: Image of the Coma Cluster from Zwiki's paper used to model the virial theorem. Each point represents a nebula [9].

1.2.2 Rotational Curves

After the observations and calculations made by Zwicky [9], there was a lull in dark matter research until Vera Rubin's work starting in the 1970's. In galaxies, luminous matter (stars) are clustered towards the center and become more sparse as one approaches the galactic edges [15] [16] [17]. Using Newtonian mechanics, the relation between rotational velocity and distance from the center of mass is

$$v(r) = \sqrt{\frac{GM}{r}}, \tag{1.2}$$

where v is rotational velocity, G is Newton's gravitational constant, M is the center of mass, and r is the distance from the center of mass. The majority of the baryonic matter in galaxy is clustered in the center and becomes sparse towards the galatical edges. One

would expect that the gravity dependent rotational curves would decrease as a function of distance from the center. Instead Rubin discovered the opposite. The rotational curves of galaxies remained constant and even extended beyond the region of visible matter, see figure 1.3. These studies re-ignited scientific interest in this unknown mass. Since this finding, thousands of galaxies have been studied, each with their own dark matter halo that extends beyond the region of visible matter [16] [17].

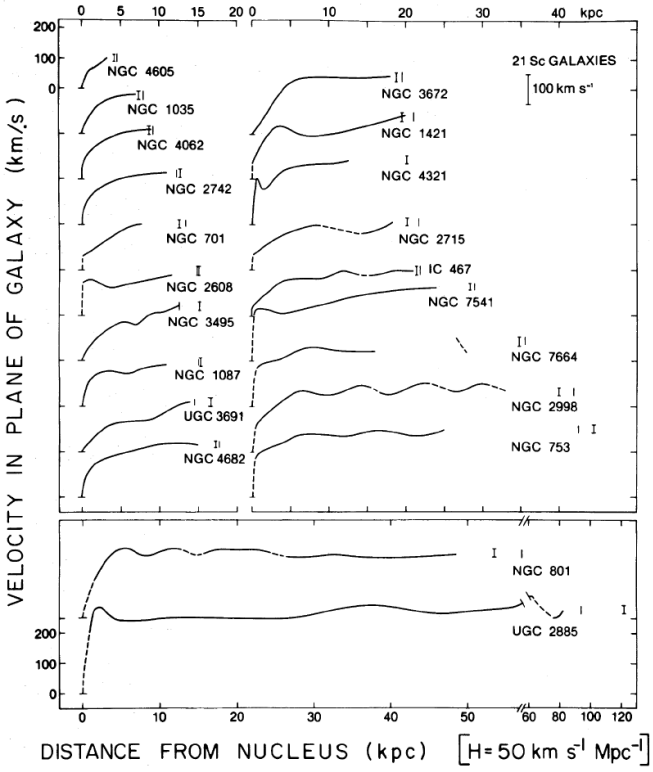

Figure 1.3: The mean velocities of 21 spiral galaxies in the plane of the galaxy as a function of distance from the center of the galaxy (nucleus). The x axis is distance in kpc and the y axis is velocity in km/s. Note that none of the galactic curves diminish at large radii. This runs contrary to what one would expect from observing the distribution of luminous matter of a galaxy [16].

1.2.3 Gravitational Lensing

Gravitational lensing describes the gravitation effects due to the distribution of matter between a distant, light-producing object and an observer. The matter between the observed and the observer is a great enough mass such that the light from the observed is distorted before reaching the observer. The distortion of the object is related to the strength of the gravitational potential. This was first theorized by Einstein in the year 1916 as a part of the theory of general relativity [18]. The first indirect observation of the this effect was documented in 1919 [19], where the gravitational pull of the sun was observed to bend the light of stars passing by during eclipse, causing the stars to appear out of position. It was further shown in 1979, that gravitational lensing responsible for the quasar QSO 0957+561A/B appearing as two separate objects [20]. This came to be known as the Twin Quasar and is considered to be the first direct observation of the effects of gravitational lensing.

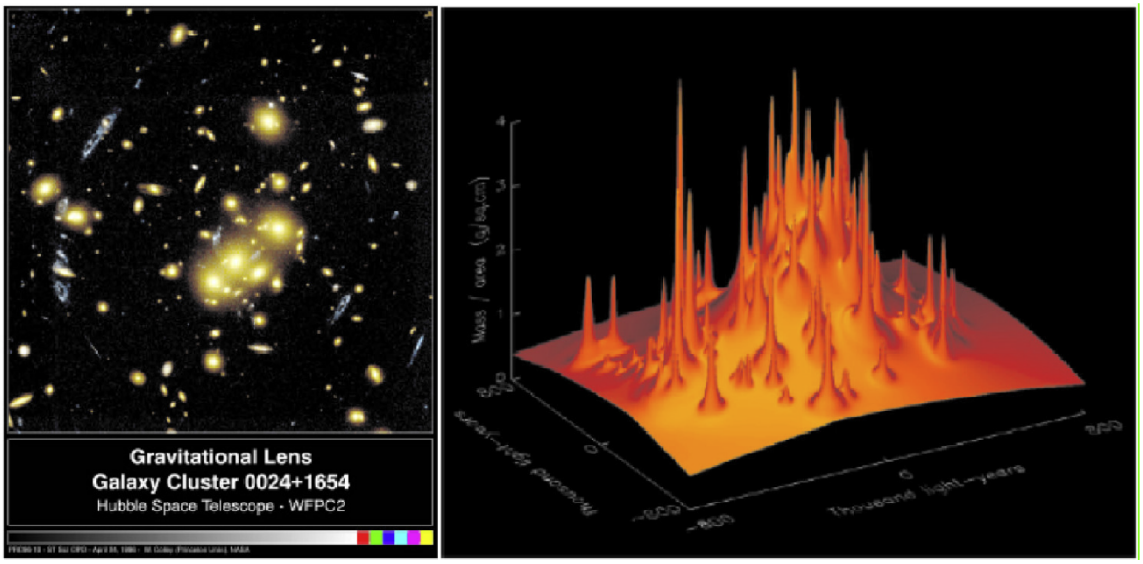

Figure 1.4: The image on the left is an example of lensing of a quasar (the blue arcs) by the 0024+1654 cluster. The image on the right is a reconstruction of matter distribution of the same cluster. The spike are individual galaxies rising above a smooth dark matter halo [21].

As in the case of the Twin Quasar, some gravitational lenses are strong enough to produce clear arcs or multiple images. This can be described by

$$\theta_E = \left(\frac{4GM}{c^2} \frac{D_{ds}}{D_s D_d} \right) \tag{1.3}$$

where θ_E is the Einstein angle, is M is the mass of the lens, D_d is the distance between the observer and the lens, D_s is the distance between the observer and the source, and D_{ds} is the distance between the lens and the observer. As shown in Figure 1.4, gravitational lensing is used to locate the distribution of dark matter through galaxies by observing geometric distortion.

Bullet Cluster

One of the most exciting, recent pieces of evidence of dark matter came through the observation Bullet Cluster collision [22]. The X-ray band from the collision was observed using the Chandra X-ray Observatory [23]. The visible band was observed by the Hubble Space Telescope. The majority of the baryonic matter in a cluster of galaxy is composed of X-ray emitting gasses [24] [25]. Measuring X-ray emissions of the collision is an effective method for tracking the locations of baryonic matter throughout the collision. Gravitational lensing occurs as result of any type of massive matter, including dark matter. A false color image of this collision is shown in Figure 1.5. In Figure 1.5, there is a clear separation between the X-ray band (baryonic matter) and the gravitational lens (dark matter and other matter). One can see that the hot gas and baryonic matter (shown in blue) from the two clusters are interacting with each other and slowing down. The majority of the matter (shown in red) has passed straight through, without interaction. This is consistent with dark matter models.

Figure 1.5: This is a false color image of the Bullet cluster collision. The baryonic matter and hot gas, as observed by the Chandra X-ray Observatory, are pictured in red the mass inferred through gravitational lensing by the Hubble Space Telescope in blue [26].

1.2.4 The Cosmic Microwave Background

A further piece evidence for dark matter comes from the earliest moments of Universe. After the Big Bang, the Universe was in a state that was too hot for hydrogen to form. Photons, frequently scattered by free charges, lost directional information from whence they originated. Approximately 378,000 years after the Big Bang, the Universe was cool enough for electrons and protons to bind. Photons created at this time had a mean free path essentially larger than the size of the Universe and have been propagating through space ever since, though slowed from universal expansion. These photons are the Cosmic Microwave Background (CMB) and take the form of a blackbody distribution with a temperature of approximately 2.73 K. Since they have not scattered since formation, their fluctuations provide information about the structure of the early Universe. See Figure 1.6

for an image of the Wilkinson Microwave Anisotropy Probe (WMAP). The WMAP is the culmination of temperature measurements made across the visible universe of the CMB. The Lambda Cold Dark Matter (ΛCDM) model contains predictions for the angular distribution of these photon fluctuations that depend on the presence of early dark matter, dark energy, and baryonic matter concentrations. The temperature anisotropies of the CMB have been measured by COBE [27], WMAP [28], and the Planck satellites [29]. The findings further support the existence of dark matter and dark energy in the Universe [30].

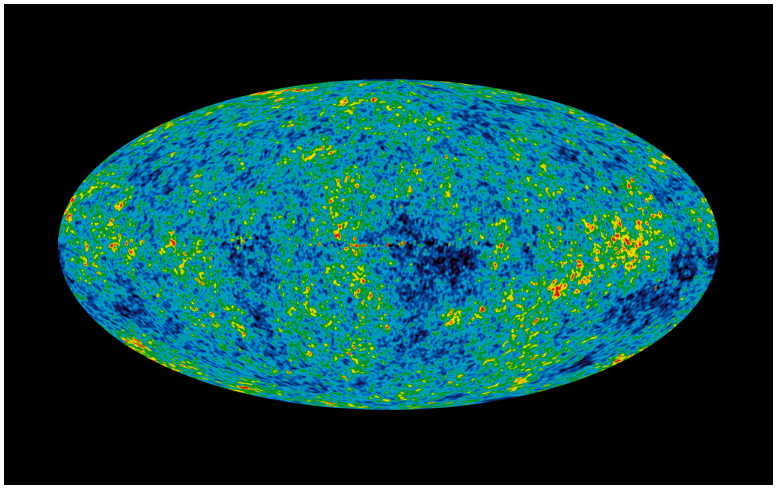

Figure 1.6: The cosmic microwave background temperature fluctuations from 9 years of WMAP data [30].

1.3 Models for Dark Matter

What cannot be determined from the studies listed above is that there is prevalence of mass in our Universe that can be accounted for by baryonic matter alone. The mass-energy composition of the Universe is 71.4% dark energy, the force responsible for the acceleration of the expansion of the Universe [31], 24% is dark matter, theorized to be particle that

interacts gravitationally and possible via the weak nuclear force, and 4.6% of matter is atoms or baryonic matter [30]. Figure 1.7 depicts this distribution.

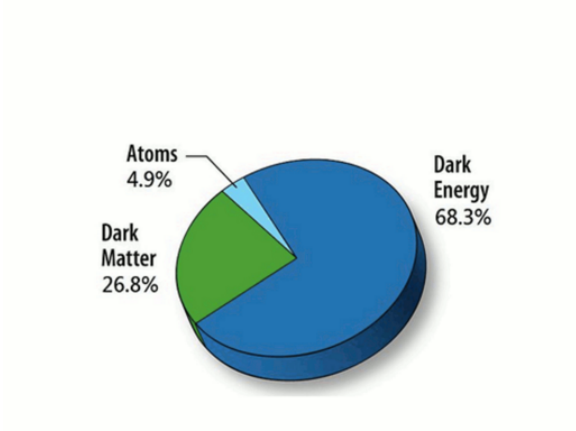

Figure 1.7: A pie chart representing the energy distribution of the Universe into dark energy, dark matter, and atoms [30].

There are variety of theories attempting to explain this missing mass. A selection are reviewed below.

1.3.1 Alternate Dark Matter Theories

MOND

One alternative theory to the problem of missing mass is to adjust Newton's equations of motion so as to account for the observed rotational galactic curves [32]. This theory is called Modified Newtonian Dynamics (MOND). It has had a small measure of success in reflecting the observed rotation curves [33]. However, it is not successful in explaining the CMB or the distribution of dark matter throughout galaxies [34].

MACHOS

Another explanation for dark matter is the prevalence of Massive Compact Halo Objects (MACHOS). These are large structures composed of baryonic matter that emit no or very little light. Black holes, brown dwarfs, and neutron stars and counted as possible suspects. Their presence might explain part of the dark matter problem. The collaborations EROS and MACHO search for these objects using micro-lensing signatures when these objects pass in front of a bright star [35] [36] [37]. There is some evidence for MACHO's [38], but their existence alone cannot account for all dark matter.

1.3.2 Dark Matter Models

The currently favored idea for non-baryonic dark matter is that it is composed of particles that originated in the hot stage of the universe and survived the passage of time to the present day [39].

Neutrinos

One candidate for dark matter comes in the form neutrinos. Neutrinos were first theorized by Pauli [40] in the 1930's. The first direction detection was made in the late 1950's [41]. Neutrinos are leptons that interact only via the weak nuclear force and gravity. These particles were produced in great numbers in the early universe and exist today in relative abundance [39]. Three types of neutrinos have been detected, along with their subsequent anti-particles. These are ν_e, ν_μ, and ν_τ. (These are also called electron neutrino, muon neutrino, and tau neutrino respectively.)

Originally neutrinos were assumed to be massless and have only one helicity state. This changed when Ray Davis reported on the first experiment to measure neutrinos from

the sun [42]. This experiment measured solar neutrinos detected in a large container of chorine. This works by

$$\nu_e + {}^{37}Cl \rightarrow {}^{37}Ar + e. \tag{1.4}$$

The total accumulation was only about a third of the predicted amount [43], which was puzzling the scientific community at the time and several members of the physics community dismissed the findings as an experimental error.

Bruno Pontecorvo suggeted an alternative solution to this issue of the Davis experiment; electron neutrinos produced by the sun are transformed into a different type of particle to which the Davis experiment could not detect [44]. This process is now called neutrino oscillations. This can be understood using the quantum mechanics of mixed states.

Let us consider a case with two neutrino types ν_e and ν_{mu} [45]. If these can convert to one another, then neither is an eigenfunction of the Hamiltonian. Therefore the stationary states or some orthogonal linear combinations:

$$v_1 = cos\theta\nu_{mu} - sin\theta\nu_e \tag{1.5}$$

and

$$v_2 = sin\theta\nu_{mu} + cos\theta\nu_e. \tag{1.6}$$

t/ Using the Schrödinger equation, the time dependence for these eigen states is $e^{-iE_1t/\hbar}$. So $v_1(t)$ and $v_2(t)$ are expressed

$$v_1(t) = v_1(0)e^{-iE_1t/\hbar} \tag{1.7}$$

and

$$v_2(t) = v_2(0)e^{-iE_2t/\hbar} \tag{1.8}$$

If the particle began as an electron neutrino then $\nu_e(0) = 1$, $\nu_{mu}(0) = 0$. This means

$$v_1(0) = -sin\theta \tag{1.9}$$

and

$$v_2(0) = cos\theta. \tag{1.10}$$

Using this we can express $v_1(t)$ and $v_2(t)$ as

$$v_1(t) = sin\theta e^{-iE_1t/\hbar} \tag{1.11}$$

and

$$v_2(t) = cos\theta v_2(0)e^{-iE_2t/\hbar}. \tag{1.12}$$

We can then use this to solve Equations 1.5 and 1.6 for ν_{mu}.

$$\nu_{mu}(t) = cos\theta v_1(t) + sin\theta cos\theta(e^{-iE_1t/\hbar} + e^{-iE_2t/\hbar}) \tag{1.13}$$

We can then calculate the probability that the electron neutrino has converted into a

muon neutrino after a time t

$$|\nu_{mu}(t)|^2 = (sin\theta cos\theta)^2(e^{-iE_2t/\hbar} - e^{iE_1t/\hbar})(e^{-iE_2t/\hbar} + e^{iE_1t/\hbar}) \tag{1.14}$$

$$|\nu_{mu}(t)|^2 = \frac{sin^2(2\theta)}{4}(1 - e^{i(E_2-E_1)t/\hbar} - e^{-i(E_2-E_1)t/\hbar} + 1) \tag{1.15}$$

$$|\nu_{mu}(t)|^2 = \frac{sin^2(2\theta)}{4}\left(2 - 2cos\frac{(E_2 - E_1)t}{\hbar}\right) \tag{1.16}$$

$$|\nu_{mu}(t)|^2 = \frac{sin^2(2\theta)}{4}4sin^2\left(\frac{(E_2 - E_1)}{2\hbar}t\right) \tag{1.17}$$

or

$$P_{\nu_e\to\nu_{mu}} = \left[sin(2\theta)sin\left(\frac{E_2 - E_1}{2\hbar}t\right)\right]^2 \tag{1.18}$$

We can then see why the nomenclature is a neutrino oscillation. The ν_e will convert to ν_{mu} and then back again. Using this theory the ν_e and ν_{mu} do not have well defined masses (energies). We can address this by using

$$E^2 - |p|^2c^2 = m^2c^4. \tag{1.19}$$

We will use m_1 to be the mass eigenstate corresponding to v_1 and m_2 to be the mass eigenstate corresponding to v_2. So we see

$$E^2 = |p|^2c^2 + m^2c^4 = |p|^2c^2\left(1 + \frac{m^2c^2}{|p|^2}\right) \tag{1.20}$$

$$E \approx |p|c\left(1+\frac{1}{2}\frac{m^2c^2}{|p|^2}\right) = |p|c + \frac{m^2c^3}{2|p|}. \tag{1.21}$$

Then

$$E_2 - E_1 \approx \frac{m_2^2c^3 - m_1^2c^3}{2|p|} \approx \frac{m_2^2 - m_1^2}{2E}c^4 \tag{1.22}$$

We can then express the probability of oscillation (Equation 1.18) over a given distance using $z \approx ct$. (Neutrinos travel at relativistic speeds). This yields

$$P_{\nu_e \to \nu_{mu}} = \left(sin(2\theta)sin\left[\frac{(m_2^2 - m_1^2)c^3}{4\hbar E}z\right]\right)^2. \tag{1.23}$$

Further, after the distance

$$L = \frac{2\pi\hbar E}{(m_2^2 - m_1^2)c^3} \tag{1.24}$$

the maximum probability of conversion is attained. From this we can see the necessary ingredients for neutrino oscillations: there must be mixing (θ) and the masses must be unequal and non-zero. Further it was determined that neutrino mass very small. These observations were confirmed in solar neutrinos by Super-Kamiokande collaboration [46]. The Super-K detectors were senstive to both the muon and tau neutrinos as well as the electron neutrino.

These relativistic particles lead to the theory of dark matter known as Hot Dark Matter (HDM). Zel'dovich and others proposed that neutrinos could account for the missing in the Universe [47] [48]. These models do not accurately predict the structure of the Universe.If neutrinos were to account for all of dark matter the Universe would need to have been formed in a "top down" fashion [49]. Superclusters forming first and galaxies forming

later, the opposite of what is presently observed [50].

Axions

Axions are a theoretical particle proposed by Peccei and Quinn. This particle is a solution to problem that the strong force allows for CP violation [51], but no CP violations has been observed. Axions are Nambu-Goldstone bosons resulting from broken symmetry and therefore would be present throughout the Universe in large quantities [52]. Axions would not produce thermal radiation making them a viable candidate for dark matter.

WIMPS

Weakly Interacting Massive Particles (WIMPS) are the most popular dark matter candidate. WIMPs comprise a class of new particles, symbolically labeled with χ, that will interact via the weak nuclear force. WIMPS are thought to have to have a mass between approximately 1GeV and approximately 1 TeV.

From a cosmological perspective, WIMP particles were created at the time of the Big Bang, when the Universe was still quite hot, these particles remained in thermal and chemical equilibrium until the expansion of the Universe became comparable to the particle rate of annihilation. After this point, annihilation became a rare event. This time is referred to as the freeze out. This relic WIMP density from the big band would be present in the Universe today.

This is shown in the following equations. In order for the relic density to account for the presence of dark matter we must have

$$\Omega_{DM}h^2 = \frac{3 \cdot 10^{-27} cm^3/s}{\langle \sigma_A \nu \rangle} \approx 0.1, \tag{1.25}$$

where Ω_{DM} is the ratio of dark matter density to the critical density ($\Omega_{DM} \approx 0.22$) and h is the Hubble parameter. From this, we get

$$\langle \sigma_A \nu \rangle \approx 3 \cdot 10^{-26} cm^3/s \rightarrow \sigma_A^2 \approx \frac{\alpha^2}{M_{EW}^2}, \tag{1.26}$$

where M_{EW}^2 is the electroweak scale, approximately 100 GeV. This phenomenon is referred to as the WIMP miracle and points to a link between dark matter and the weak force. Therefore any particle with a mass of 100 GeV that interacts via the weak force becomes a dark matter candidate. These particles become non-relativistic at the time of freeze out.

1.4 Methods of Dark Matter Detection

There are three primary methods for experimental dark matter detection: dark matter production, indirect detection, and direct detection. A diagram of these three methods can be found in Figure 1.8. In all three cases, the assumption is that dark matter interacts with Standard Model matter, through so form of yet to be discovered physics.

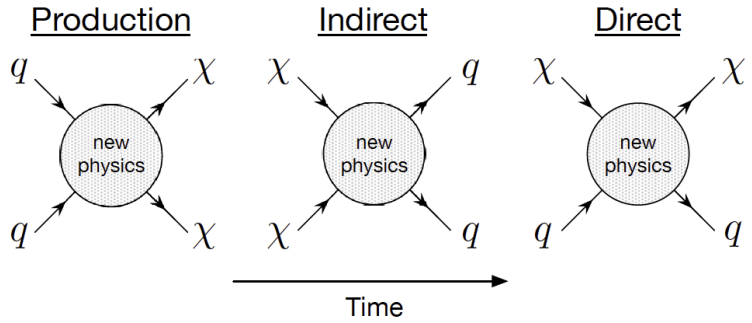

Figure 1.8: This is visual represention of three detection techniques for WIMPS, where the WIMPS are coupled to Standard Model particles (q) through some unknown new physics.

1.4.1 Indirect Dark Matter Detection

Dark matter particles may self-annihilate or annihilate with other particles such as tau leptons [53]. These annihilations would produce high energy photons or rare anti-particles. These would be evident in areas of high dark matter concentrations, such as the centers of galaxies. Detecting this signal would be indirect dark matter detection. A lack of signal could set a limit on WIMP parameters. Research groups, such as the Fermi Gamma Ray Space Telescope, look for gamma ray signals in space that could potentially indicate dark matter annihilations. This type detection is high model dependent which makes the analysis for detection complicated [53].

There is also an active field of research looking for dark matter signals in dwarf spheroidal galaxies. These are expected to contain a large volume of dark matter and with less measurement background than larger galaxies, like the Milky Way. Several searches have been underway with no discernible signal detected. These results have placed some constraints on WIMP masses below approximately 20 GeV.

1.4.2 Accelerators

Large particle accelerators, like the LHC, are searching for the elusive particles, using the dark matter production method. It is thought that if a collision within the detector exceeds the energy of a WIMP mass, a WIMP could be generated in the collision and escape before detection in the accelerator. The signal could reveal the missing energy or momentum from the generated WIMP and thus provide a detection signal [54] [55]. This method renders testing the stability of the particle discovered impossible, therefore it will be difficult to determine if a particle found using this method accounts for the dark matter found throughout the Universe [56]. This method could be useful in setting limits for

dark matter couplings with Standard Model particles [56].

1.4.3 Direct Dark Matter Detection

The Milky Way galaxy, like other galaxies is enveloped in a dark matter halo. Earth would pass through billions of WIMP particles every second. Most of the particles travel directly through the planet without interaction. However, there is the possibility that one of these particles could interact with matter on earth via WIMP-nucleon scattering process. Direct detection experiments are designed around measuring the recoil energy of such an event. The energy spectrum of a recoil depends on both the properties of WIMPS and the target material. In selecting an appropriate target material, it needs to be sensitive to the KeV energy scale, as seen by the equations below.

Let us consider a target nucleus of mass m_N. The recoil energy of a WIMP scattering is given by

$$E_r = \frac{\mu_N^2 \nu^2 (1 - cos\theta^*)}{m_N}, \tag{1.27}$$

where θ^* is the scattering angle in the center-of-mass frame, ν is the velocity of the WIMP, and

$$\mu_N = \frac{m_\chi m_N}{m_\chi + m_N}, \tag{1.28}$$

where m_χ is the mass of the WIMP. A backscattering process, where $\theta^* = 0$, deposits the maximum recoil energy. Thus,

$$E_{r,max} = \frac{2\mu_N^2 \nu^2}{m_N}. \tag{1.29}$$

In the case of a fixed recoil energy, the minimum WIMP velocity is described as

$$\nu_{min} = \sqrt{\frac{E_r m_N}{2\mu_N^2}}. \tag{1.30}$$

The average ratio of kinetic energy is expressed as

$$\frac{E_r}{E_\chi} = \frac{2\left(\frac{m_N}{m_\chi}\right)}{\left(1+\frac{m_N}{m_\chi}\right)^2}, \tag{1.31}$$

Therefore, a typically nuclear collision will deposit about 100 to 10 keV of recoil energy in liquid argon, which has nucleus mass of 37 GeV. Naturally the WIMP mass is unknown, thus the exact amount of recoil energy from such an event is still mysterious. This is measurable in low threshold detectors. If we instead consider an electron target ($m_N = m_e$), the energy transfer is less than 1 eV, an extremely challenging amount to detect.

The per kilogram of target material differential scattering rate can be expressed as

$$\frac{dR}{dE_r} = \frac{1}{m_N}\frac{d(N_\chi\langle\sigma v\rangle)}{dE_r} = \frac{\rho_0}{m_N m_{chi}}\int_{v_{max}}^{v_{min}}\left(\frac{d\sigma}{dE_r}\right) v f(\vec{v}) d^3v, \tag{1.32}$$

where N_χ is the number density of WIMPS, ρ_0 is the average WIMP mass density, $f(\vec{v})$ is the normalized velocity distribution, and $\frac{d\sigma}{dE_r}$ is the differential cross section. This differential cross section can be modeled as a point-contact interaction with a cross section σ_0. This is coupled to a nuclear for factor F. This can be expressed as

$$\frac{d\sigma}{dE_r} = \frac{\sigma_0}{E_{r,max}} F^2(q), \tag{1.33}$$

where

$$q = \sqrt{2m_N E_r} \tag{1.34}$$

is the transfer of momentum.

A 100 GeV WIMP has a deBroglie wavelength that is around the diameter for a large nucleus. This would cause a WIMP to interact coherently with the entire nucleus. The results in the standard spin-independent point-contact interaction cross section of

$$\sigma_0 = \frac{4\mu_N^2}{\pi}(Zf_p + (A - Z)f_n)^2, \tag{1.35}$$

where A is the total number of nucleons, Z is the total number of protons, f_p is the coupling strengths to protons and f_n is the coupling strength to neutrons. Supersymmetric models generally assume $f_p \approx f_n = f$, simplifying σ_0 to

$$\sigma_0 = \frac{4\mu_N^2}{\pi}A^2 f^2. \tag{1.36}$$

Equation 1.36 can be used to describe the WIMP interaction cross section per target nucleus. This is not particularly useful since different experiments use different target materials. So instead we can express the cross section per target nucleon. The normalized WIMP-nucleon cross section for a single proton is

$$\sigma_p = \frac{\mu_p^2}{A^2\mu_N^2}\sigma_0, \tag{1.37}$$

where μ_p is the WIMP-proton reduced mass. We can use this to simplify Equation 1.32 as

$$\frac{dR}{dE_r} = \frac{1}{2}\frac{\rho_0 A^2 \sigma_p}{\mu_p^2 m_\chi} \int_{v_{max}}^{v_{min}} \frac{F^2(q)}{v} d^3v \tag{1.38}$$

The differential scattering rates (spin-indpendent) for varius WIMP masses and target materials are shown in Figure 1.9.

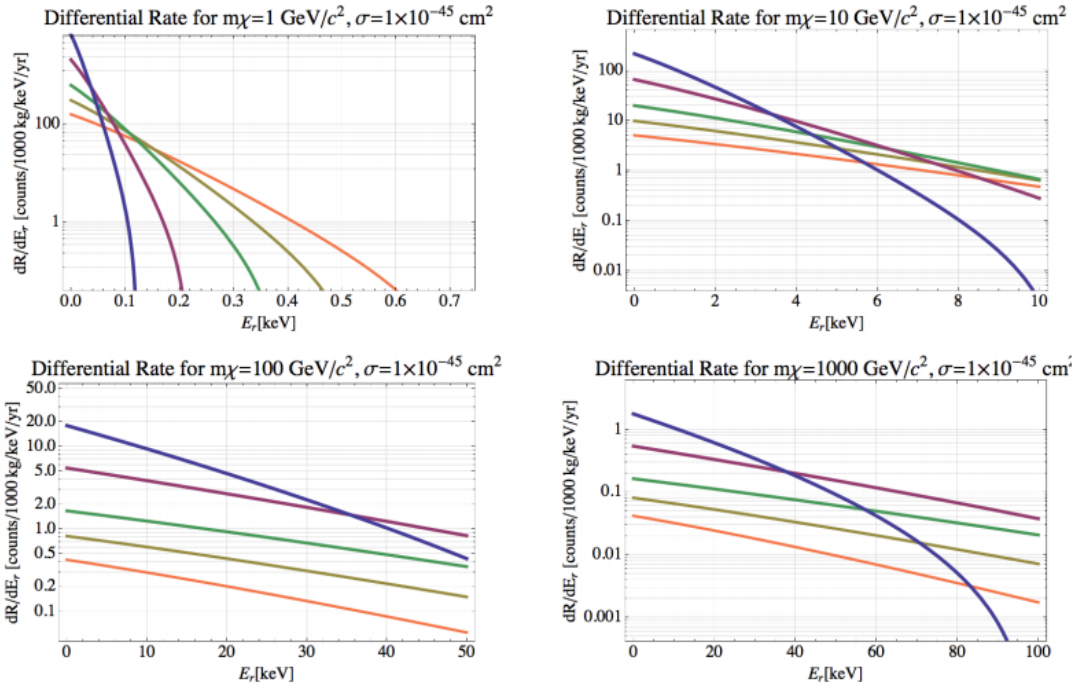

Figure 1.9: Upper left - differential scattering rate versus recoil energy for 1GeV WIMPS, Upper Right - differential scattering rate versus recoil energy for 10GeV WIMPS, Lower Left - differential scattering rate versus recoil energy for 100 GeV WIMPS, and Lower Right - differential scattering rate versus recoil energy for 1TeV WIMPS. The blue is xenon, the purple is germanium, the brown is silicon, the orange is neon, and the green is **argon** [57].

Direct Detection Dark Matter Detectors

Dark matter detectors function by using a media which makes the recoil energy from a WIMP scatter a measurable quantity. Due to the rarity of these events, these detectors

need to be large and have excellent background rejection. Most experiments are located underground to reduce the cosmic ray background contamination. All these detectors require high levels of radio-purity to prevent background radiation from contaminating the signal. Roughly speaking there are three technological categories of detectors. Figure 1.10 summarizes several detection methods.

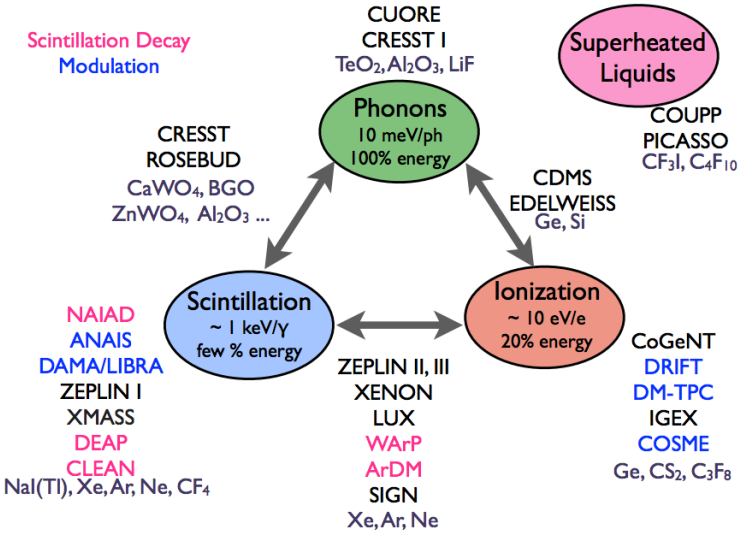

Figure 1.10: This diagram depicts various recoil energy deposition channels and how they are used in various experiments. The experiments that appear between the two channels measure both [58].

Cryogenic Semiconductor Detectors Cryogenic semiconductor detectors use crystalline substrates with a variety of sensors to measure recoil energies of particle scatters. The recoil energy is distributed by some combination of ionization, scintillation, and phonons. These detectors include CDMS [59], EDELWEISS [60], CoGeNT [61], CRESST [62], CDEX [63], and DAMA/LIBRA [64].

Bubble Chamber Experiments Bubble chambers are a less used detector technology. The detectors utilize superheated fluids and interactions generate visible bubbles that can

imaged. These detectors rely on the acoustic signal from the bubbles to differentiate alpha backgrounds. These detectors include PICASSO [65], COUPP [66], and PICO [67].

Liquid Noble Detectors Liquid noble detectors use large vessels of liquid noble elements, such as xenon or argon, as a target material. Noble elements are scintillators, meaning they produce light as a result of particle scattering. Liquid noble detectors can take the form of time projection chambers or pulse shape discriminators. A time projection chamber uses a combination of electric and magnetic fields together with a volume of gas, liquid, or mixed state, to form a three-dimensional reconstruction of a particle trajectory or interaction. A pulse shape discriminator utilizes the light output of argon to differentiate between different types of signals. (This is discussed at length in Chapter 2.) Notable experiments that use xenon as a detector medium include XENON [68], LUX/LZ [69] and ZEPLIN [70]. Liquid argon detectors are discussed in greater detail in the section below.

This is not exhaustive list of dark matter experiments. More information about the present state of direct dark matter detections can be found in [58]. As my work focuses on measuring properties in liquid argon for detector improvement. I am going focus primarily on liquid argon detectors.

1.5 Liquid Argon Detectors

1.5.1 DarkSide

DarkSide-50 is a liquid argon detector that uses a time projection chamber style of detector [5]. This iteration of the detector uses an active argon volume of 50 kg and is filled with depleted argon from underground sources [71]. This diminishes the natural background

radiation contained within atmospheric argon. Event significance is determined by the 3D event position within the detector and pulse shape discrimination. This is based on the present understanding of the optics of liquid argon at the scintillation wavelength.

1.5.2 ArDM

The ArDM experiment is another dark matter experiment that utilizes time projection chamber technology [17] [72]. The detector operates in a double phase mode (liquid-vapor). Gas is at the top of the detector and the liquid is at the bottom. When an event occurs, scintillation light and free electrons from ionization travel through the detector. The ionized electrons drift from the liquid into the argon vapor. This is accomplished by using an electric field in the kV/cm range. These electrons interact with the argon gas producing secondary scintillation light. The intensity of this light is proportional to the initial charge. Both the light from initial scintillation in the liquid argon and the secondary scintillation light are recorded. The time difference yields information about the event's location. This is based on understanding the path of light traveled through argon.

1.5.3 MiniCLEAN

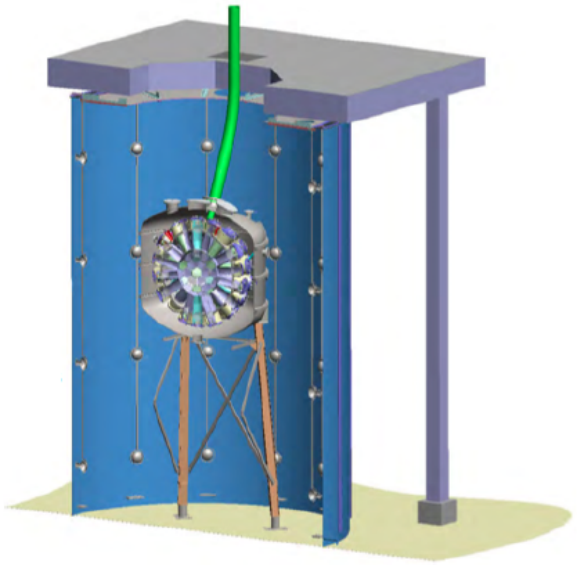

Figure 1.11: The MiniClean Experiment.

MiniCLEAN is a direct detection dark matter experiment that is currently constructed and is in the process moving towards acquiring data [73] [74]. The MiniCLEAN detector will use 360 liters of liquid argon to search for dark matter. The argon is located within the inner vessel (IV). This argon is monitored by 92 photomultiplyer tubes (PMT's), sensitive, single photon detectors, to detect scintillations within the detector. These PMT's are attached to light guides surrounding the IV to direct the signal. The scintillation light within the detector is 128 nanometers. This light range cannot be detected by the PMTs used in the experiment, so the end of the light guide is coated in tetra phenyl butadiene (TPB) which shifts the wavelength of the scintillation light to 420 nm, a wavelength that is detectable by the PMT. This IV will be placed with in the outer vessel (OV) which is under vacuum. This vacuum space is a thermal shield between the OV and the IV. The OV will then be placed in a tank and will be completely submerged in water. This set up can

be seen in Figure 1.11. Event location within the detector is determined by examining the PMT hit pattern with an understanding of the optics in the argon, including the index of refraction and Rayleigh scattering length. Event location is crucial as background events from material radioactivity are more likely to occur at the outskirts of the liquid volume, whereas a WIMP event could occur anywhere in the detector. The signal region in the center of the detector is called the fiducial volume.

1.5.4 DEAP3600

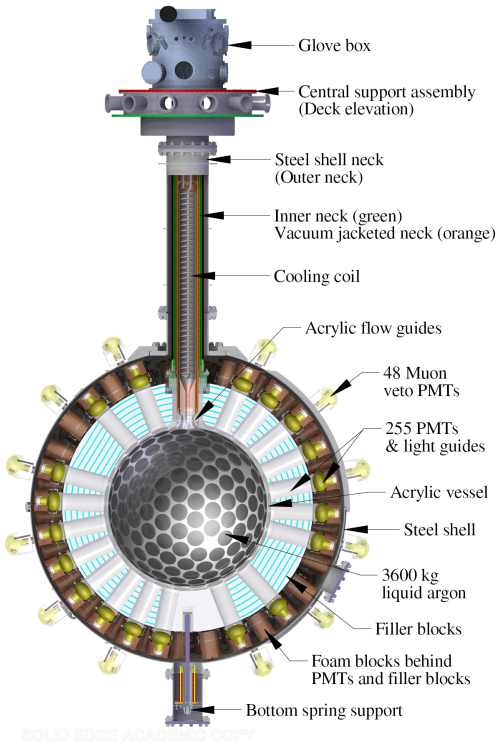

Figure 1.12: The DEAP3600 experiment.

The DEAP3600 is another direct detection dark matter experiment that is in the process of taking data [75]. This detector will use 3600 kilograms of liquid argon. This detector

has many similar properties to the MiniCLEAN detector. The largest difference is that the DEAP-3600 detector target volume is surrounded by an acrylic sphere. This acrylic sphere acts as a neutron shield. A picture of this experiment can be found in Figure 1.12. Like, MiniCLEAN, event location is one method of determining an event's significance. This involves a deep understanding of the optics of the liquid argon, the TPB coating, and the acrylic vessel.

All of the argon detectors discussed rely on a deep understanding of the optics of the scintillation light of liquid argon. The following chapter will describe the benefits of liquid argon as a detector medium in greater detail, as well describing the optics of the material.

Chapter 2

Chapter 2: Argon Scintillation Physics

Argon must not be deemed rare. A large hall may easily contain a greater weight of it than a man can carry.

- Lord Rayleigh

2.1 Introduction

Argon is an inert chemical element discovered at the end of the 18th century by Lord Rayleigh and William Ramsey [76]. It is the third most abundant gas in the Earth's atmosphere. The triple point, the state where liquid, solid, and gas coexist in thermal equilibrium, of argon is 83.8058 K at 0.6889 bar. The boiling point, the temperature at which argon gas liquifies, is 87.302 K. The melting point, the temperature at which liquid argon becomes solid, is 83.81 K. These values are needed to build a liquid argon detector that will keep argon at temperature and pressure so that it will remain in a liquid state. The phase diagram for argon around the triple point can be found in Figure 2.1.

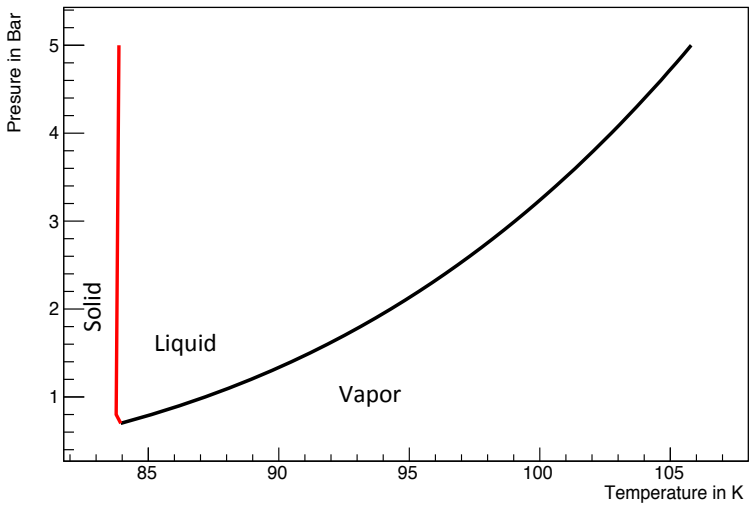

Figure 2.1: Phase diagram of argon detailing the three states of argon. The x axis is temperature in K and the y axis is pressure in bar. This was generated with values of measuring the melting line and vaporization line from [77] and [78].

Liquid noble low background detectors are used in various experiments seeking to measure low rate processes, like dark matter, and therefore require low background detectors. The primary elements used in such experiments are argon and xenon. Table 2.2 compares the properties of argon with other nobles elements. Liquid argon is relatively simple to purify, both through heated getter technologies [79] [80] [81] and charcoal traps [82]. The interaction cross section of noble scintillators is related to the square of the nuclear mass. The self shielding properties are related to the density. Self shielding improves as detectors get larger. Liquid argon has additional benefit for large detectors as it is less expensive (by an order of magnitude) than other noble elements.

Property	Helium	Neon	Argon	Krypton	Xenon
Atomic Number	2	10	18	36	54
Nuclear Mass	4.002602	20.179	39.948	83.708	131.293
Liquid Density (g/cm^3)	0.145	1.207	1.3954	2.413	2.942
Boiling Point at 1 atm (K)	4.22	27.1	87.3	119.74	165.0
Melting Point at 1 atm (K)	-	24.6	83.8	115.8	161.4
Approximate Cost/100g	$5.20	$33	$0.50	$33	$120

Table 2.1: Comparison of nuclear mass [83], liquid density [83], scintillation wavelengths [84], and approximate costs of noble elements, accurate as of 2012. [85]

2.2 Argon-39 Background

A further consideration in noble detectors is the level of natural contamination and the extent to which this contamination can be accounted for in detection techniques.

Since argon is abundant in Earth's atmosphere, most argon used in experiments is atmospheric argon. Argon does have a natural radiation contamination of ^{39}Ar, a β emitter [86], [17]. ^{39}Ar is entirely comic ray produced [86]. The half life of ^{39}Ar is 269 years [87]. The energy for ^{39}Ar is 565 keV. The rate of ^{39}Ar in atmospheric argon ind a detector is 1 Bq/kg [86]. Therefore, as these detectors grow in size, so does the rate of ^{39}Ar events increase. The energy spectrum for ^{39}Ar is in Figure 2.2.

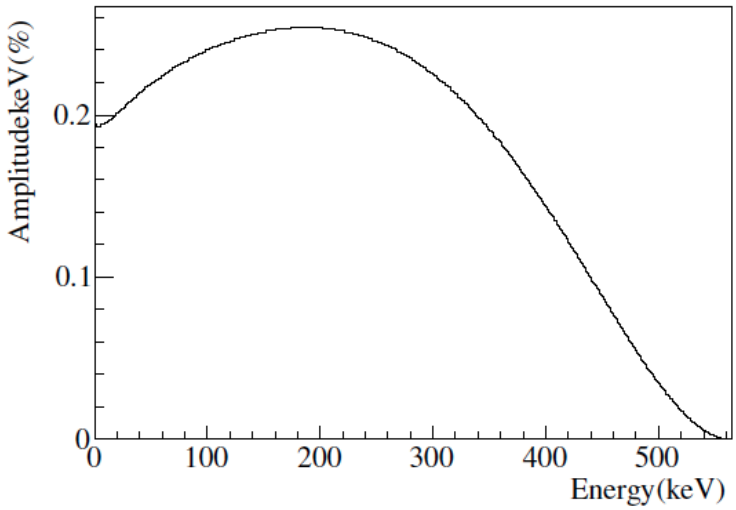

Figure 2.2: The energy spectrum of ^{39}Ar. The x-axis is energy in KeV and the y-axis is % amplitude [88].

There are two experimental methods for dealing with this background in dark matter detection. One method is to use depleted argon. There is a recently discovered source of underground argon with an activity rate of less than 5% of regular argon. This argon is used by the DarkSide Collaboration [71]. Using this method, they have reduced the activity of the ^{39}Ar background by a factor of $(1.4\pm0.2)\times10^3$ relative to the atmospheric rate [71]. The initial result shows a background free null result accumulated over 70.9 live days. They are predicting measurements over their 3 year search to yield a minimum of 5.5 tonne-year exposures free of ^{39}Ar background [71].

There is limited supply of depleted argon, so experiments, such as DEAP, which use atmospheric argon, instead rely on pulse shape discrimination to differentiate between the electronic recoils of the ^{39}Ar background and nuclear like recoil of a possible dark matter induced signal event. To understand this difference, the scintillation process is described in detail from light generation to light detection in a single phase detector such as DEAP.

2.3 Argon Scintillation

When an ionizing particle travels through liquid argon, it deposits its energy via scatters with the electrons or the nuclei of the surrounding argon atoms [83]. These atoms either ionize through the loss of of an electron (Ar^+) or enter into an excited state (Ar^*). The Ar^+ and Ar^* states then bond with other atoms forming dimer molecules (Ar_2^*), a molecule that consists of two identical atoms. The process for forming the Ar_2^* takes place in two channels. In the first, Ar^* combine with ground state atoms, directly forming Ar_2^* diamer. In the second channel, Ar^+ ions combine with other argon atoms to form Ar_2^+, ionized molecules. The Ar_2^+ combine with free electrons to form Ar_2^* . The Ar_2^* dimers, in channels are unstable and quickly disassociate, releasing a VUV photon, which corresponds to an energy of 9.7 eV [89] and wavelength of 128 nm. A diagrams of the process is found in Figure 2.3. Argon is transparent to its own scintillation light because the energy of the released photon is not high enough to excite ground state Ar atoms. Furthermore the wavelength of the light is between the UV and IR resonance wavelengths. (This will be discussed more in Chapter 3.)

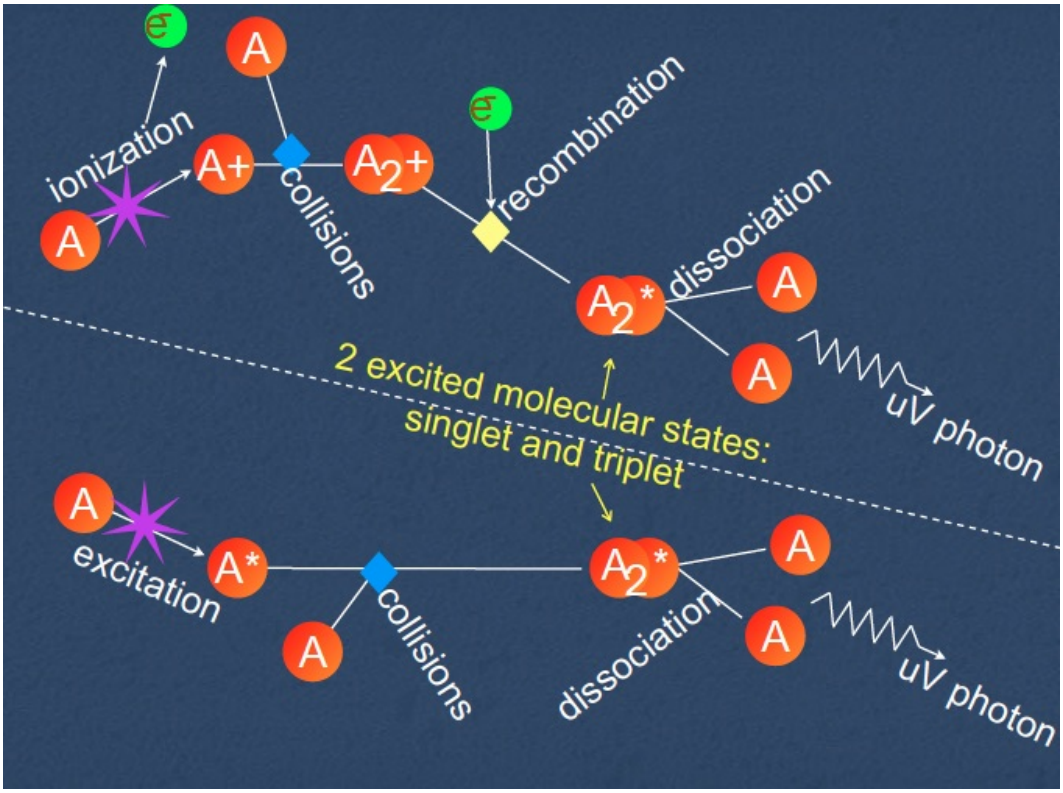

Figure 2.3: A picture showing the two types of noble element scintillation. The top portion half is pictorial representation of dimer production and disassociation via ionization. The bottom portion is a pictorial representation of dimer production and disassociation via excitation.

The process of scintillation through excitons (Ar^*) can also be described using the follow chemical equations [90],

$$Ar^* + Ar \rightarrow Ar_2^* \tag{2.1}$$

$$Ar_2^* \rightarrow 2Ar + \gamma(128\ nm), \tag{2.2}$$

where γ is the VUV scintillation photon. This combines with argon atom forming Ar_2^*, the excited molecule. This de-excites by emitting at 128 nm photon.

The process of scintillation through ions (Ar^+) is described using the following chemical

equation,

$$Ar^{+} + Ar \rightarrow Ar_2^{+} \tag{2.3}$$

$$Ar_2^{+} + e^{-} \rightarrow Ar^{**} + Ar \tag{2.4}$$

$$Ar^{**} \rightarrow Ar^{*} + heat \tag{2.5}$$

$$Ar^{*} + Ar \rightarrow Ar_2^{*} \tag{2.6}$$

$$Ar_2^{*} \rightarrow 2Ar + \gamma(128\ nm). \tag{2.7}$$

In this case, $Ar^{**} \rightarrow Ar^{*} + heat$ corresponds to transition in which light is not emitted. (Ar^{**} is an atom in an excited state that is two or more energy levels greater than the ground state.) In each type of scintillation, the lowest excited energy level de-excites by emitting a single photon [90].

2.3.1 Scintillation Decay Time Constants

The two types of dimers formed in noble element scintillation are known as singlet ($^1\Sigma_u^+$) and triplet states ($^3\Sigma_u^+$), have different decay life times. The singlet state decays very quickly (see Table 2.2 for singlets lifetimes) into two ground state atoms. The triplet state survives for much longer [91] (see Table 2.2 for triplet lifetimes) because the triplet state requires a forbidden spin flip to decay to ground state. The triplet lifetime varies according the nobel element used as a scintillator and is related to the mass of atom. This can be understood by assuming the spin flip comes from spin-orbit coupling.

Property	Helium	Neon	Argon	Krypton	Xenon
Scintillation Wavelength [λ] (nm)	78	80	128	147	178
Singlet Decay Time [τ_1] (ns)	1	22	7.0	3	4
Triplet Decay Time [τ_3]	13 s	15 μs	1.5 μs	111 ns	21 ns
$\tau_3 \times Z^4$ [s]	208	0.15	0.16	0.18	0.18
Yield (photons/kev)	15	1.5 $\times 10^4$	4.0 $\times 10^4$	NA	4.2

Table 2.2: The scintillation wavelength [84] [92], time constants and light yields [92] for noble elements. Helium yield from [93] [94].

The following using [95] to explain the relationship between atomic mass and triplet lifetime. In the classical sense, spin-orbit coupling comes from the interaction of the electron spin with the magnetic field generated by its own orbital motion around the nucleus,

$$H = -\mu \cdot \mathbf{B}, \tag{2.8}$$

μ is the magnetic moment of the electron and $\mathbf{B}$ is the magnetic field. $\mathbf{B}$ can be expressed as,

$$\mathbf{B} = \frac{\mathbf{E} \times \mathbf{v}}{c}, \tag{2.9}$$

$\mathbf{E}$ is the electric field, $\mathbf{v}$ is velocity and c is the speed of light. The relation for magnetic moment μ can be expressed as,

$$\mu = -\frac{eh}{2mc}\sigma, \tag{2.10}$$

where σ is the Pauli matrices. Further,

$$S = \frac{h\sigma}{2}. \tag{2.11}$$

The relation for $\mathbf{v}$ can be expressed as,

$$\mathbf{v} = \frac{\mathbf{p}}{m}. \tag{2.12}$$

Using the above equations, H can be expressed as

$$H = \frac{eh}{2m^2c^2}\sigma \cdot \mathbf{E} \times \mathbf{p}. \tag{2.13}$$

In the classical domain for a central field E can be written as,

$$\mathbf{E} = \frac{1}{r}\frac{\delta V}{\delta r}\mathbf{r}. \tag{2.14}$$

We can use the expression for angular moment,

$$\mathbf{L} = \mathbf{r} \times \mathbf{p}, \tag{2.15}$$

and the potential

$$V = \frac{Z_{eff}}{r}, \tag{2.16}$$

where Z_{eff} is the effective charge of the nucleus, to substitute into Equation 2.13. This shows,

$$H \propto \frac{e^2}{m^2c^2}\frac{1}{r}\frac{\delta V}{\delta r}\mathbf{L}\cdot \propto \frac{Z_{eff}}{r^3}\mathbf{L} \cdot \mathbf{s}. \tag{2.17}$$

As this does not into account relativist effects, this expression shows proportionality instead of equality. Using the relation $r \propto Z_{eff}^{-1}$, we see

$$H \propto Z_{eff}^{4} \mathbf{L} \cdot \mathbf{S}. \tag{2.18}$$

We can use this relationship to normalize the triplet lifetime (τ_3) by Z^4. From this we see that $\tau_3 \times Z^4$ is between 0.15 s and 0.18 s for all elements except for helium. In the case of helium, there is no intrinsic orbital angular moment to couple the spin. This results in a much longer triplet lifetime.These values can be seen in Table 2.2.

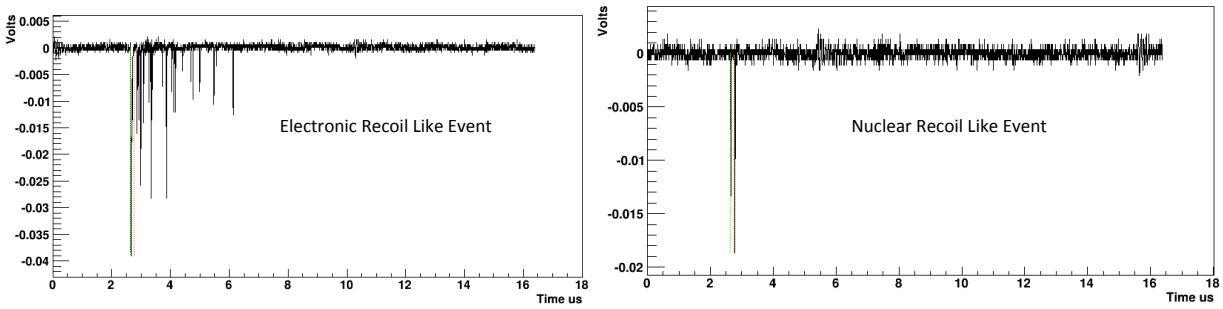

Figure 2.4: Two waveforms showing the difference between an electronic recoil event and a nuclear recoil event. For each of the above plots, the x axis is time in microseconds and the y axis is PMT voltage signal in volts. The two plot above depict waveform from test stand data showing both a nuclear recoil like event (right) and an electronic recoil like event (left). Notice that there is more fast light in the nuclear recoil event.

The fraction of singlet states to to triplet states is dependent on linear energy transfer (dE/dx) or LET of the radiation [91] [96]. More singlet states are produced as greater energy is dissipated per unit of track length. Electronic recoils have more late light, than nuclear recoils. It is this difference that provides a method for determining background. An example of a nuclear and electronic trace can be found in Figure 2.4.

The time constants between the decay times of different nobles vary according to

element. The greater difference between the time constant, the better pulse discrimination is achievable. In the case of argon the fast time constant 7 ns and the long time constant is 1.5 μs [92]. This separation makes good pulse discrimination [97]. This separation is much better than that of Krypton and Xenon where the difference between singlet and triplet states are nanoseconds instead of a microsecond. The time constants for liquid nobles can be found in Table 2.2.

One method of examining the amount of singlets (fast light) and triplets (late light) in each decay is by looking at the F_{prompt}. This is the fraction of fast light to total light generated in an event and is described by the following equation,

$$F_{prompt} = \frac{\int_0^{t_1} V(t)dt}{\int_0^{t_2} V(t)dt}, \tag{2.19}$$

where

$$V(t) = V_0 \frac{1}{\tau_1}(1 - e^{-t/\tau_1}) + \gamma \frac{1}{\tau_2}(e^{-t/\tau_2}), \tag{2.20}$$

where t_1 is the prompt window, a length of time experimentally determined for fast light, t_2 is the total length of time, τ_1 is the fast light decay constant, τ_2 is the slow light decay constant, and γ is the ratio of slow light to fast light. The pulse shape discrimination from F_{prompt} can be seen in Figure 2.5

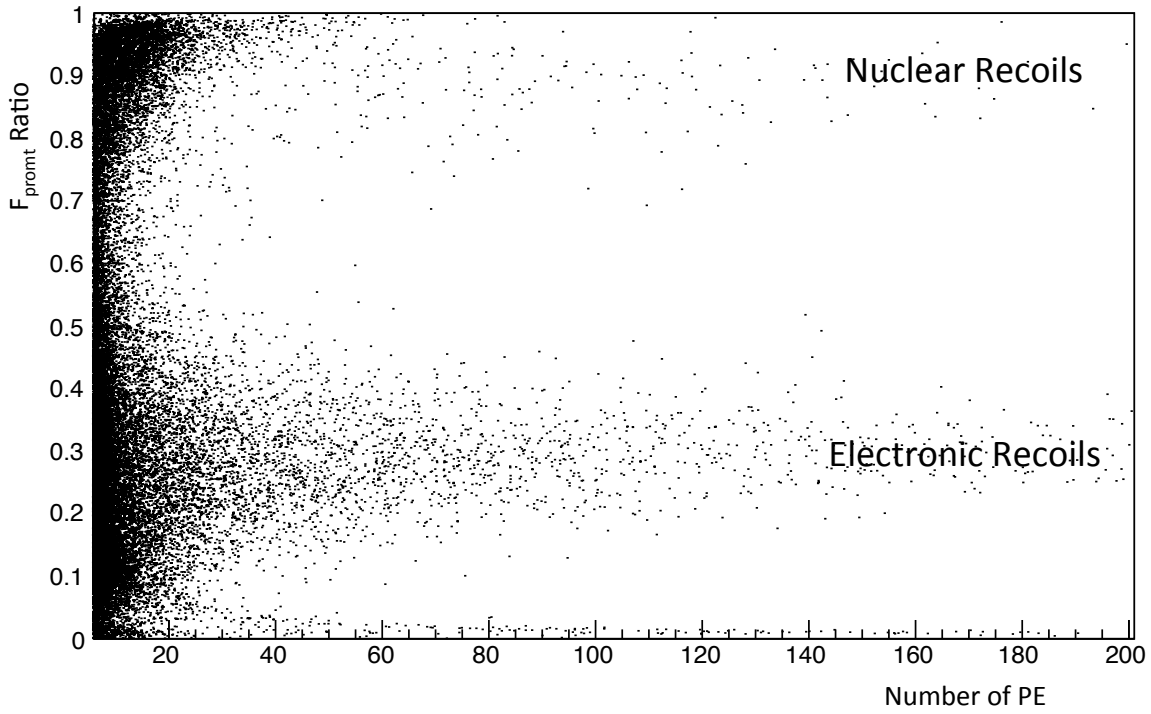

Figure 2.5: This is plot of the fraction of prompt light. The x-axis is photoelectron counts (PE) and the y-axis is the fraction of prompt light (F_{prompt}).The fraction of light arriving within the early window as a function of PE count for nuclear and electronic recoils. The two peak separation makes pulse shape discrimination possible. This figure came from data taken in the Rayleigh scattering test stand.

2.4 Light Propagation through Argon

Large, single phase detectors rely on optical event reconstruction to determine event locations within this detector. Photon detection systems in liquid noble detectors typically surround the noble liquid volume, and therefore the size and spatial distribution of the measured signal depends on the physics of photon propagation through the medium. The

next section reviews the possible optical processes that could occur with liquid argon that could impact event reconstruction within a detector and demonstrates that the dominate process within these detectors is Rayleigh scattering and the index refraction of the scintillation light.

2.4.1 Rayleigh Scattering

Rayleigh scattering was first proposed in 1899 [98]. Rayleigh scattering is the process of light elastically scattering off particles in a medium. The wavelength of the light is not changed in the scattering process. The length of of travel for a photon through a medium before Rayleigh scattering is strongly dependent on the wavelength of the light as well as the optical properties of the material. This can be seen in the Rayleigh equations that follow. The derivation of the Rayleigh scattering equation follows from [99] and [100]

In the simplest form, Rayleigh length is expressed as

$$l = \frac{1}{\sigma N}, \tag{2.21}$$

where N is the molecular density of a medium ($molecules/m^3$) and σ (m^2) is the Rayleigh scattering cross section. The cross section was first expressed as [98]

$$\sigma = \frac{24\pi^3}{N^2\lambda^4}\frac{[n^2-1]^2}{[n^2+2]^2}, \tag{2.22}$$

where N is the number density, n is the index of refraction, and λ is the wavelength of light. It was later found through experiment that this equation was not sufficient to describe the cross section of anything other than a spherical gas molecule [99]. To correct for a non-spherical particles the King's correction factor [100] [101] was added so the cross section reads:

$$\sigma = \frac{24\pi^3}{N^2\lambda^4}\frac{\left[n^2-1\right]^2}{\left[n^2+2\right]^2}F_k, \tag{2.23}$$

where

$$F_k = \frac{(6+3\rho_n)}{(6-7\rho_n)}. \tag{2.24}$$

In this equation ρ_n is the depolarization ratio that accounts for the anisotropy of non-spherical molecules [102]. However in the case of noble gases, these are spherical molecules, so the Kings correction constant is assumed to be 1. However Equation 2.23 was found to be insufficient in predicting the Rayleigh scattering length in liquids and solids [100]. Einstein proposed a modification to Equation 2.23 in 1910 to account for the thermodynamics of liquids and solids [103]. This equation reads

$$l^{-1} = \frac{16\pi^3}{6\lambda^4}\left[kT\rho^2\kappa_T\left(\frac{\partial n^2}{\partial\rho}\right)_T^2 + \frac{kT^2}{\rho c_\upsilon}\left(\frac{\partial n^2}{\partial T}\right)_\rho^2\right], \tag{2.25}$$

where l^{-1} is the inverse Rayleigh scattering length, c is the velocity of light, k is the Boltzmann's constant, T is the temperature, ρ is the liquid density, and κ_T is isothermal compressibility, and c_υ is the heat capacity. In the temperature range of solid and liquid argon, the second term is small enough to be negligible [100] [104], so the equation becomes:

$$l^{-1} = \frac{16\pi^3}{6\lambda^4}\left[kT\rho^2\kappa_T\left(\frac{\partial n^2}{\partial\rho}\right)_T^2\right]. \tag{2.26}$$

The following steps are used to estimate $(\partial n^2/\partial\rho)_T$ [104]. The Lorentz-Lorenz equation (Equation 2.27) [105] [106] relates the index of refraction to the wavelength of light can

be expressed as follows [107],

$$\frac{n^2-1}{n^2+2} = \rho\left(a_0 + \sum_i \frac{a_i}{\lambda^2 - \lambda_i^2}\right). \tag{2.27}$$

In this equation, n is the index of refraction, ρ_m is the density in moles per unit volume, λ is the wavelength of light, λ_i is the wavelength corresponding to the i^{th} resonance, a_i is the constant related to the strength of the resonance, and a_0 is a constant experimentally determined using index refraction measurements. For the sake of simplicity, we will define

$$a_0 + \sum_i \frac{a_i}{\lambda^2 - \lambda_i^2} = C, \tag{2.28}$$

where C is a constant associated with a particular wavelength. So then the Lorentz-Lorenz becomes

$$\frac{n^2-1}{n^2+2} = C\rho. \tag{2.29}$$

Next, we use this expression to get $(\partial n^2/\partial\rho)_T$

$$\left(\frac{\partial n^2}{\partial \rho}\right)_T = \frac{3C}{(1-C\rho)^2} = \frac{(n^2-1)(n^2+2)}{3\rho}. \tag{2.30}$$

Using this expression for $(\partial n^2/\partial\rho)_T$, l^{-1} becomes

$$l^{-1} = \frac{16\pi^3}{6\lambda^4}\left[kT\rho\kappa_T\left(\frac{(n^2-1)(n^2+2)}{3}\right)^2\right]. \tag{2.31}$$

This equation is satisfactory for calculating the Rayleigh scattering length of spherical molecules when n^2 corresponds to the index of refraction at the temperature, density and wavelength used elsewhere in the equation [99].

2.4.2 Mie Scattering

The intensity due to Rayleigh scattering can be expressed as

$$I = I_0 \left(\frac{1 + cos\theta}{2R^2} \right) \left(\frac{2\pi}{\lambda} \right) \left(\frac{n^2 - 1}{n^2 + 2} \right)^2 \left(\frac{d}{2} \right)^6 , \tag{2.32}$$

where I is the intensity of photons detected, I_0 is the intensity of photons generated, θ is the angle, R is the distance of the observer, λ is the wavelength of light, n is the index of refraction corresponding to the wavelength of the light and d is the particle diameter. The intensity of the light detected depends strongly on the the wavelength of light and size of the particle. The ratio of these two values determines if the Rayleigh model of scattering is sufficient to describe the system. If the wavelength of light is much greater than the particle diameter, then Rayleigh scattering is sufficient for describing extinction. In the case that the particle diameter is larger than the wavelength of light, then Mie theory will be needed to fully model scattering [108].

In the case of argon the wavelength of light is 128 nm and the diameter of an argon atom has been measured to be 71 pm (0.071nm) [109] [110]. The wavelength of light is 4 orders of magnitude greater than the argon particle diameter. In [111] Mie scattering was not observed in argon with argon droplets with a radius less than $2\mu m$. Therefore, Mie scatter should not be a significant contribution to extinction, the total amount of light due to scattering or other processes that is lost before detection.

2.4.3 Absorption

Another potential optical process that occurs to photons traveling through a media is self absorption. This occurs when a photon is absorbed by another atom with the same media. The emission spectra for argon was measured by [112] and is found in in Figure 2.6.

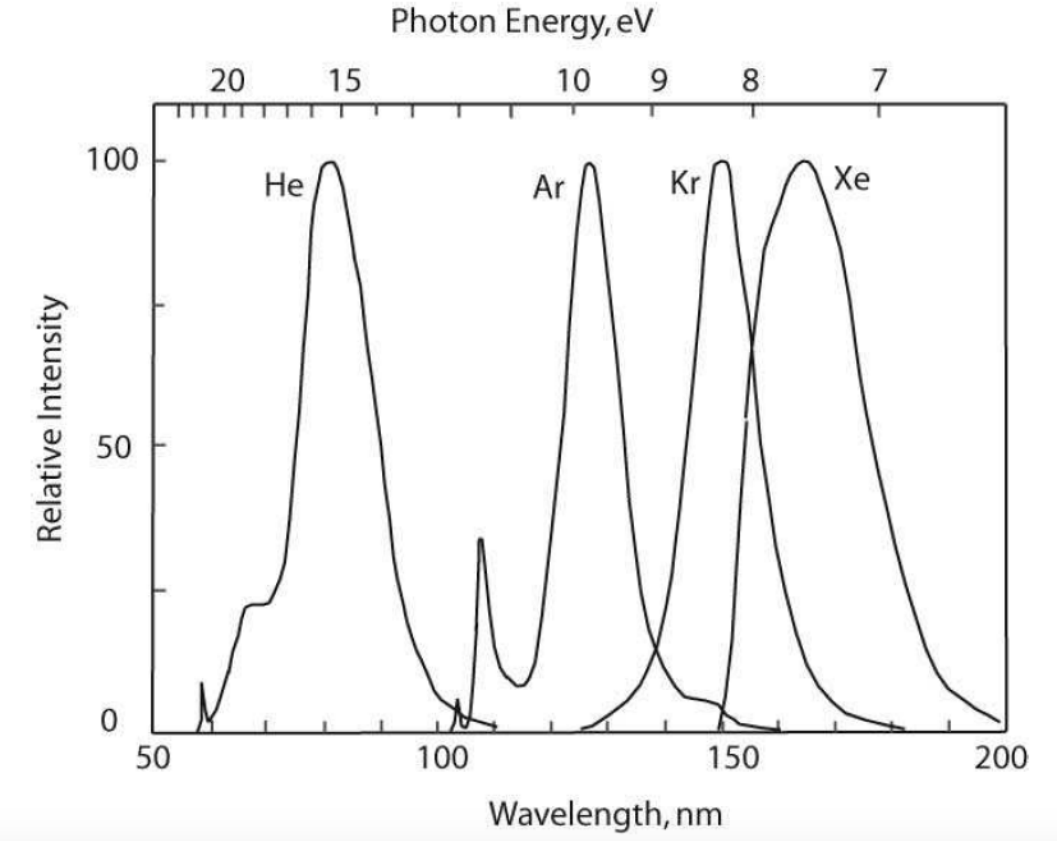

Figure 2.6: This shows the emission spectra of the helium, argon, krypton and xenon. The x axis (lower) is wavelength (nm), the x-axis (upper) is photon energy (eV), the y axis is relative intensity. The peaks have been normalized to show the same intensity at the maximum. The figure is taken from [83] using data from [112]

The absorption spectra for solid argon was measured by Baldini [113]. The results of the measurement are detailed in Figure 2.7.

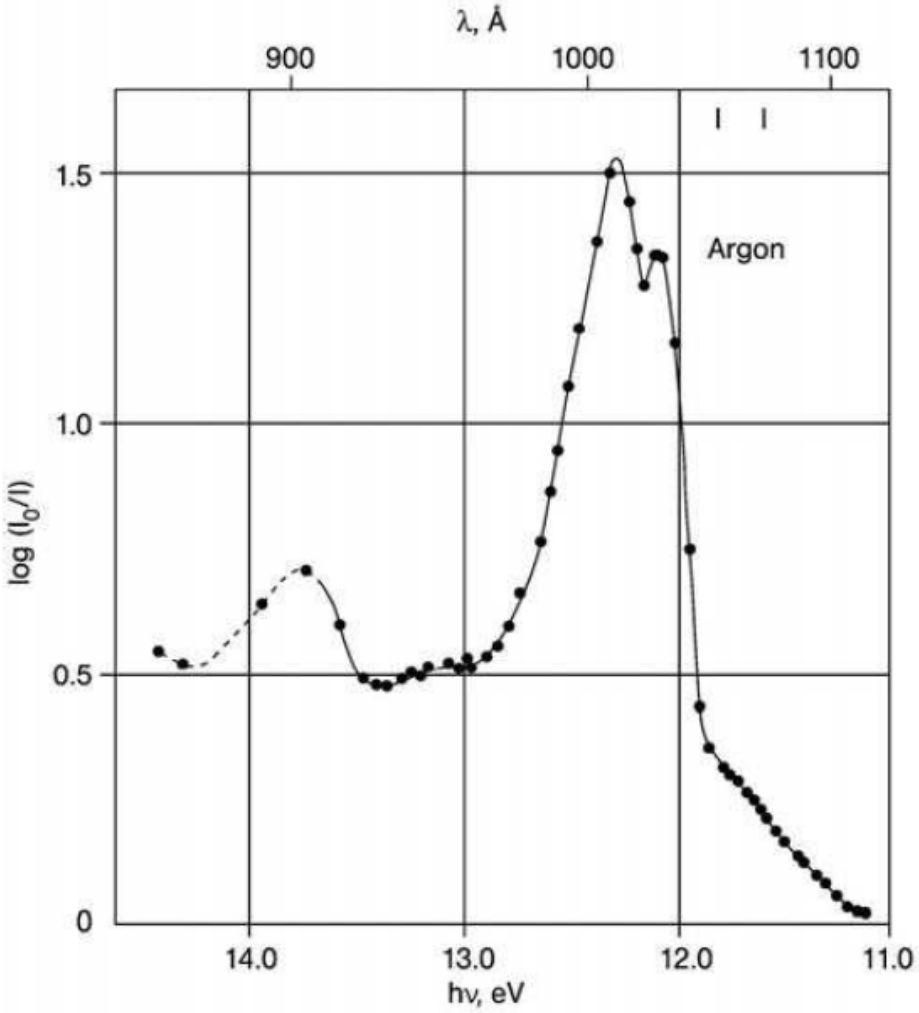

Figure 2.7: This shows the absorption spectra measured by Baldini [113]. The x axis (lower) is energy in eV, the x axis (upper) is wavelength in $\AA$. The image is taken from [83] using data from [113].

By comparing Figure 2.6 and Figure 2.7, the emission spectra of argon falls outside of the absorption spectra. This make the contribution of self absorption in pure argon negligible [83].

The self absorption within argon can be altered by the presence of impurities within the argon [114]. It was found by [115] [116] that the argon contaminated with as little as 1 part

per million (ppm) impacted the self absorption. Further, the greater the contamination, the shorter the triplet lifetime [115]. This effect can be controlled by purifying the argon used in experiments. The getters used both by the test stand step up described in this thesis as well as the getter used by DEAP3600 purify argon so that the presence of oxygen and nitrogen is less that 1 ppm [81]. Therefore, the impact of impurities upon total total extinction should be negligible. This can be determined by measuring the triplet lifetime within argon data to determine the presence of problematic impurities.

2.5 Scintillation Light Travel Through TPB

The wavelength of the scintillation light of liquid argon is too short to be efficiently detected by most photomultiplier tubes (PMT's). Therefore the wavelength needs to be shifted to a wavelength that is compatible with light detection technology. Typically this is done using tetraphenyl butadiene (TPB). TPB is a fluorescing, organic chemical compound compound that shifts VUV to 430 nm [117] [118], which is in the visible range and easily detectable by PMT's [119]. The efficiency for emission after absorption for TPB is slightly greater than 1, however the emission is isotropic [119]. Some of the scintillation light is lost in the wavelength shifting process as it could re-emitted in a direction away from the detectors.

2.6 Scintillation Light Detection

After the scintillation light has been shifted to a detectable wavelength the final journey is detection by the photon detector. Typically this is a PMT. Information about the event is discerned using the voltage output. The efficiency of detection is impacted by the quantum efficiency of a PMT as well as the temperature at which the PMT is being operated. This

temperature reduction of efficiency can be avoided by using PMT's specifically designed for low temperature operation.

2.7 Discussion

The dominate optical process within argon is Rayleigh scattering which is strongly dependent on the index of refraction of the wavelength of light (see equation 2.31). Other optical processes will have negligible contributions within pure argon. At the time of writing the index refraction of 128 nm light in liquid argon has not reached a consensus within the scientific community [120] [104]. This is discussed in the next chapter in further detail.

Chapter 3

Index of refraction, Rayleigh scattering, and Sellmeier coefficients in solid and liquid argon, xenon, and krypton

Is there a thing whereof it is said: See, this is new?–it hath been already, in the ages which were before us. -The Teacher

3.1 Introduction

Common noble element targets used in scintillation detectors are argon, krypton, and xenon. The scintillation photons in liquid noble detectors are detected using photo-sensors, and therefore knowledge of the index of refraction of the liquid noble and the photosensor cover (e.g. glass, and other materials like acrylic in the case of DEAP-3600 [121]) is required to model the transmission and reflection at such interfaces. The probability that a photon is detected by a photosensor depends on the scattering lengths in the medium, and the path-length of liquid noble it traverses. These values are wavelength dependent. The scintillation wavelength for argon, xenon, and krypton are shown in Table 3.1. At present, the values for liquid xenon have been measured and confirmed in calculations.

However, there are inconsistent values in argon and krypton from previous measurements and calculations. These parameters have not been measured for this noble target in a solid state. This chapter reviews the status of current knowledge, and calculates new values for these parameters for argon, xenon, and krypton based on previous measurements.

Element	Scintillation Wavelength (nm)
Argon	128
Xenon	147
Krypton	178

Table 3.1: The scintillation wavelength of argon, xenon, and krypton [84].

The Rayleigh scattering lengths at the scintillation wavelength in liquid argon and krypton were measured by Ishida et al [122] and were extrapolated by Seidel et al [104]. The values obtained by these two groups differ by 27% in the case of liquid argon. This a large enough discrepancy to impact event reconstruction (this will be discussed in more detail in Chapter 7). The Rayleigh scattering length and index of refraction at the scintillation wavelengths of solid argon, xenon, and krypton are not known. While there is not presently a large experiment using solid nobles, this information could be useful for future experiments.

Clarification of the Rayleigh scattering lengths is of interest to a number of low background experiments including the DEAP/CLEAN collaboration [123], [124] and MicroBooNE [125] and experiments that use liquid krypton calorimetry like Na48 at CERN [126]. The DEAP/CLEAN collaborations use large liquid argon detectors in their dark matter searches [123]. These detectors have the argon contained in a spherical detector surrounded by photon detectors to detect the light from scintillation and rely on event reconstruction to determine if a scintillation event occurs within the region of interest.

This event reconstruction depends on the Rayleigh scattering length and index of refraction for liquid argon at the scintillation wavelength. MicroBooNE will use a 170 ton liquid argon time projection chamber for neutrino research [125]. The optical model used for simulating MicroBooNe [125] takes into account Rayleigh scattering around the detector edges and uses the Rayleigh scattering length extrapolated by Seidel et al [104]. This motivates a need to further clarify the precise Rayleigh scattering length at the scintillation wavelength of liquid argon.

The following is a theoretical approach to reconciling the two predominate Rayleigh scattering lengths based on the Sellmeier dispersion relationship and a survey of previous optical measurements. While the main emphasis is on the liquid argon results, the method described below is also used to determine the index of refraction and Rayleigh scattering lengths of krypton and xenon and argon in a solid state since that the data was available to generate these numbers and they are of general interest. The scintillation wave lengths of argon, krypton, and xenon are found in Table 2.2 in Chapter 2.

3.2 Index of Refraction Calculation

The Rayleigh scattering length equation for solids and liquids,

$$l^{-1} = \frac{16\pi^3}{6\lambda^4}\left[kT\rho\kappa_T\left(\frac{(n_\lambda^2-1)(n_\lambda^2+2)}{3}\right)^2\right], \tag{3.1}$$

as discussed in Chapter 2. There is heavily dependent on the index of refraction. The index of refraction in object is dependent on the wavelength of light and the material properties of the medium. This dependency is explored in the following equations.

In its simplest form, the index of refraction is defined as [99]

$$n = \frac{c}{\nu}, \tag{3.2}$$

where c is the speed of light in a vacuum and ν is the speed of light in a medium. ν is dependent on the wavelength of light and is determined by various material and thermodynamic properties, including material phase, temperature, pressure, polarizability, and molecular structure [127]. In the case of nobel detectors, temperature, pressure, phase, and atomic structure remain fairly constant, so these calculations will only be focusing on optical models that explore the relationship between the index of refraction and light wavelength. This relationship can be further examined by using the Lorentz-Lorenz equation, a phenomena discovered independently by two researchers of similar names [105], [106]. The Lorentz-Lorenz equation is

$$\frac{4\pi\alpha}{3m} = \frac{n^2 - 1}{n^2 + 2}\frac{1}{\rho_m}. \tag{3.3}$$

In this equation, α is the molecular polarizability, m is the molecular mass, n is the refractive index, and ρ_m is the molar density. The Lorentz-Lorenz equation can be derived from Maxwell's equations [128]. This equation is sufficient to describe the molar refractivity and was a bridge between Maxwell's electromagnetism equations and atomic physics [107]. This equation was originally believed to be a constant. It was later found through experiment that the index of refraction varies with wavelength and that the molar refractivity is not constant [107]. This variance is known as dispersion. This lead to a new formation of the Lorentz-Lorenz equation that accounts for the relationship between the index of refraction and wavelength,

$$\frac{n^2-1}{n^2+2}\frac{1}{\rho_m} = a_0 + \sum_i \frac{a_i}{\lambda^2 - \lambda_i^2}. \tag{3.4}$$

In this equation, n is the index of refraction, ρ_m is the density in moles per unit volume, λ is the wavelength of light, λ_i is the wavelength corresponding to the i^{th} resonance, a_i is the constant related to the strength of the resonance, and a_0 is a constant experimentally determined using index refraction measurements. The Lorentz-Lorenz equation can be further expanded to account for density and temperature variations [127] and these formulas should be used in the case where the temperature or density can not be assumed relatively constant, however this chapter will focus only on wavelength dependence since this the model most useful for large, low background noble detectors.

3.3 Measurements

With the exception of liquid xenon at the triple point [129], the index of refraction at he scintillation wavelengths of solid and liquid argon, xenon, and krypton have not been measured. There have been few measurements of the various optical properties of solid and liquid argon, xenon, krypton.

Sinnock and Smith [1] measured the index of refraction as at function wavelength a different temperatures in solid and liquid argon, xenon, and krypton. These measurements were made between the wavelengths of 350 nmnm and 650 nm with an error of $\pm 0.5\%$. This was done by passing a beam at the required wavelengths through a cell containing the element and measuring the change in angle to measure the index of refraction (Snell's law). In these experiments the temperature and density was held constant during the index of refraction measurements at different wavelengths. A full summary of their measurements can be found in Tables A.1, A.2, and A.3 in the Appendix.

Bideu-Mehu et al [130] measured the index of refraction of room temperature argon, xenon, and krypton gas between the wavelengths of 140 nm and 174 nm and used these values to find the Sellmeier coefficients for the gas based Sellmeier equation (Equation 3.5).

Ishida et al [120] measured the attenuation length of liquid xenon, argon, and krypton at the scintillation wavelengths. This was done by scintillating a 88cm tube of argon using an external ion beam through six windows. The resulting photons were detected and the Beer-Lambert relationship was used to determine the attenuation length. They found values of 66±3cm for argon at 87 K, 29±2cm for xenon at 196 K and 82±4cm for krypton at 127 K.

Barkov et al [131] measured the index of refraction in liquid xenon at a wavelength of 180 nm and found a value of 1.565±0.01. However this measurement has been shown to be inconsistent with other index of refraction measurements made in liquid xenon [132].

Solovov et al [129] measured the index of refraction and attenuation length of liquid xenon at the triple point. The found a value of 1.69±0.02 at scintillation wavelength of 178 nm.

Calvo et al [133] measured the attenuation length in situ in the ArDM TPC. They obtained value of 52.1 cm a with variation, depending on light yield, from 47.9cm to 57.7cm.

3.4 Previous Extrapolation

Seidel et al extrapolated the Rayleigh scattering length for liquid argon, xenon, and krypton. Seidel's extrapolated values were 90 cm for argon, 60 cm for kypton, and 30 cm for

xenon. The authors did not specify what the error on the extrapolation. Their extrapolations are not within error of the measured attenuation lengths of Ishida et al [122] for liquid argon (66 cm) and krypton. The extrapolated Rayleigh scattering length uncertainty was within the measured values for xenon. However a different method of extrapolation was used for xenon. In the case of xenon, both liquid and gaseous measurements were to obtain a value. In the case of argon and krypton, Seidel et al [104] used data from from Bideu-Mehu et al [130] to extrapolate the dielectric constant at the scintillation wavelengths. Bideu-Mehu measured the index of refraction of argon, xenon, krypton, and neon gases at 275 K between the wavelength of 250 nm and 140 nm [130]. These values were fit using the simplified Sellmeier equation for gasses for the relationship between the index of refraction and wavelength. The simplified Sellmeier equation for gasses is:

$$n - 1 = \frac{Ne^2}{8\pi^2\epsilon_0 mc^2} \sum \frac{f_i}{\lambda_i^{-2} - \lambda^{-2}}, \tag{3.5}$$

where n is the index of refraction, N is the number density of atoms or molecules, e and m are the charge and mass of the electron, ϵ_0 is the vacuum permittivity, λ is the wavelength, λ_i is a resonance wavelength and f_i is the Sellmeier coefficient found experimentally that corresponds to the resonance wavelength. Seidel et al did not calculate temperature dependence and made an adjustment for the density change from gas to liquid. The reasoning for including the temperature was based on the research done by Achtermann et al [134]. This study looked at the Clausius-Mossotti equation for the dielectric constants for gasses.

The Clausius-Mossotti equation for the dielectric constant in gases of low density is

$$\frac{\epsilon - 1}{\epsilon + 2} = \frac{4\pi}{3} \frac{N_a \alpha_0}{M} \rho \tag{3.6}$$

where α_0 is the polarizability, N_a is Avagadro's number and M is the atomic mass. This is similar to the Sellmeier equation shown previously, but is used to determine the relationship between dielectric constant instead of refractive index. At higher densities the interatomic interactions can influence the polarizability of the atom, Equation 3.6 is no longer correct and can be expressed as the following expansion

$$\frac{\epsilon - 1}{\epsilon + 2} = A_\epsilon(\varpi)\rho + B_\epsilon(\varpi, T)\rho^2 + C_\epsilon(\varpi, T)\rho^3 + ..., \tag{3.7}$$

where A, B, C, etc. are the dielectric coefficients. These coefficients have been measured in noble gasses at room temperature in the visible light range by Achtermann et al. [134] and it was found that under these conditions that the second and third dielectric coefficients are small enough to be negligible. Seidel et al [104] extrapolated this coefficients down to a liquid density and determined that even in a liquid the second and third dielectric coefficients were sufficiently small enough to neglect and did not include a temperature dependence in the extrapolations. Using this method Seidel extrapolated an index of refract of 1.37 in argon and 1.50 in krypton and a Rayleigh scattering length of 90 cm in argon and 60 cm in krypton. The uncertainty on this extrapolation was not reported in the paper [104].

3.5 Method

The updated calculation utilizes the valued recorded by [1] taken under the same thermal and state conditions and described previously in the chapter. In the case of the liquid state, it was to verify or dispute previous measurements or extrapolations, in the case of the solid state, it was to provide the first numbers for index of refraction and Rayleigh scattering for this state. This was done using the following Sellmeier dispersion relation

$$n^2 = a_0 + \sum_i \frac{a_i \lambda^2}{\lambda^2 - \lambda_i^2} \text{ [107].} \tag{3.8}$$

In this case a_0 is a Sellmeier coefficient that accounts for the effect of UV resonances not included in the sum and a_i are the Sellmeier coefficients that correspond to the i^{th} resonances. The Sellmeier dispersion equation was derived from the Lorentz-Lorenz equation [107]. The data from Sinnock and Smith was fit using the first UV and IR resonance wavelength for each element. The wavelengths of the data fall between these resonance peaks(as seen in Table 3.2) so these will have the most influence on the fit. The fit equation used was

$$n^2 = a_0 + \frac{a_{UV} \lambda^2}{\lambda^2 - \lambda_{UV}^2} + \frac{a_{IR} \lambda^2}{\lambda^2 - \lambda_{IR}^2}, \tag{3.9}$$

where λ_{UV} corresponds to the closest or first UV resonance and λ_{IR} corresponds to the closet or first IR resonance. The wavelengths measured were used to determine the values of a_0, a_{UV}, and a_{IR}.

The data used for the fit was taken by Sinnock and Smith. The error reported in their original work was $\pm 0.5\%$ [128] on the index of refraction, though the authors state that this was a conservative value [1]. This data can be seen in Tables A.1 - A.2 in Appendix A.

Element	UV Resonance λ (nm)	IR Resonance λ (cm)
Argon	106.6	908.3
Xenon	146.9	827.0
Krypton	123.6	965.3

Table 3.2: The resonance wavelengths of argon [135] [136], xenon [130] [136], and krypton [130] [136]

3.5.1 Extrapolation Error Calculations and Fit Verification

The error on the extrapolation was calculated using,

$$\sigma_f^2 = G^T V G, \tag{3.10}$$

where σ_f^2 is the variance in the function f with parameters n parameters, V is the covariance matrix and G is the matrix of first derivatives [137].

Solovov et al [129] measured the index of refraction of the scintillation wavelength of liquid xenon at the triple point. The liquid triple point data from [1] was fit with Equation 3.9 and used this fit to extrapolate to the scintillation wavelength. This extrapolation was verified by comparing the extrapolated value to the value measured by Solovov. The fit from the Sinnock data agree well with the measured value taken by Solovov. This can be be seen in Figure 3.1.

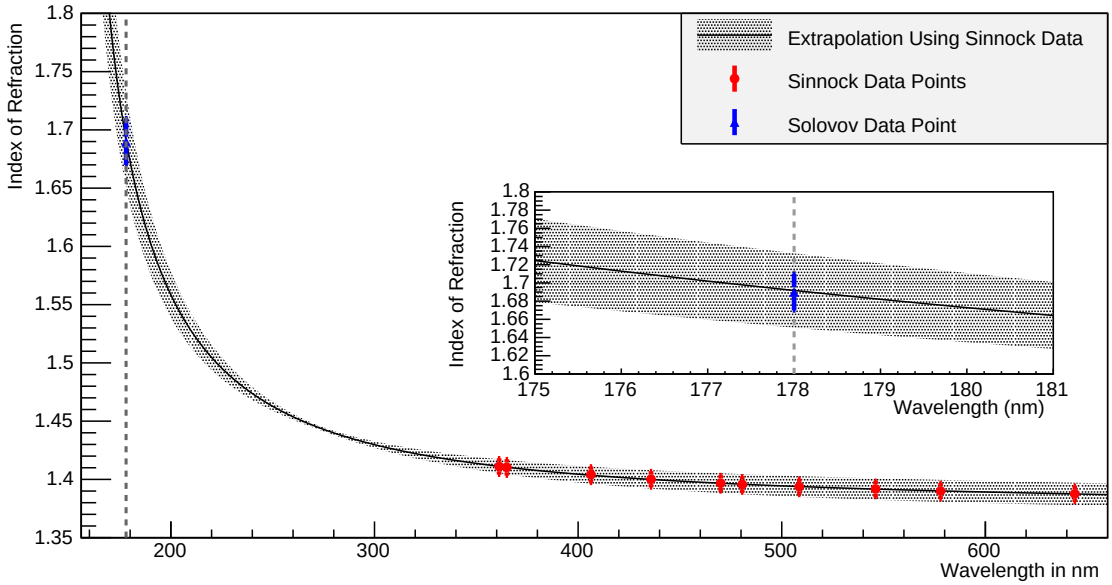

Figure 3.1: Sinnock data [1] with fit and Solovov [129] point. The x axis is wavelength in nanometers(nm) and the y axis is index of refraction. The line is the extrapolation and points corresponds to data points.

The was redone to included the points from Sinnock and the point from Solovov. This was done to improve the accuracy of the function. These fit lines can be seen in Figure 3.3.

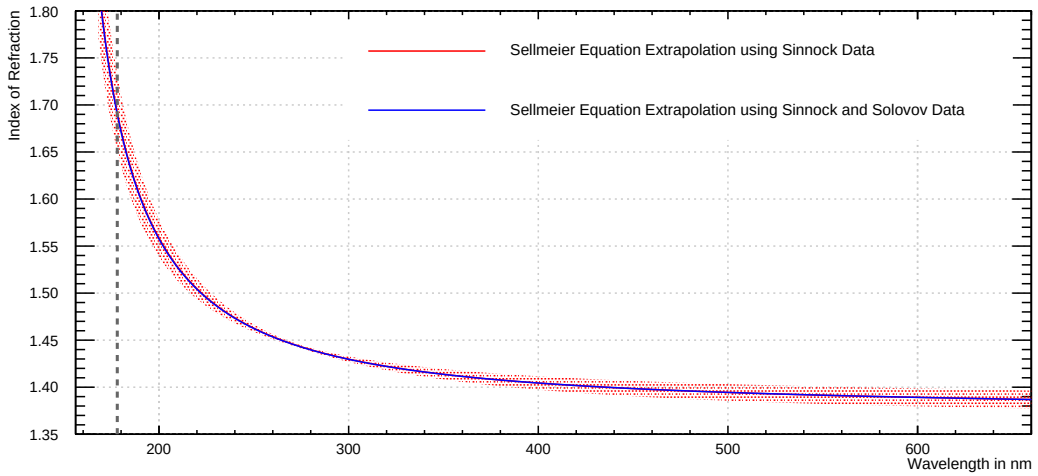

Figure 3.2: Sellmeier Fit with Sinnock data points only compared to fit with Sinnock (data shown in Table A.3) and Solovov data points. The x axis is wavelength in nanometers (nm) and the y axis is index of refraction. The red line is the Sellmeir equation extrapolation using Sinnock data only. The blue line is the Sellmeir extrapolation using both the Sinnock data point and the Solovov data point. Both fit lines have error, but the error on the blue line is too small to be seen on this plot.

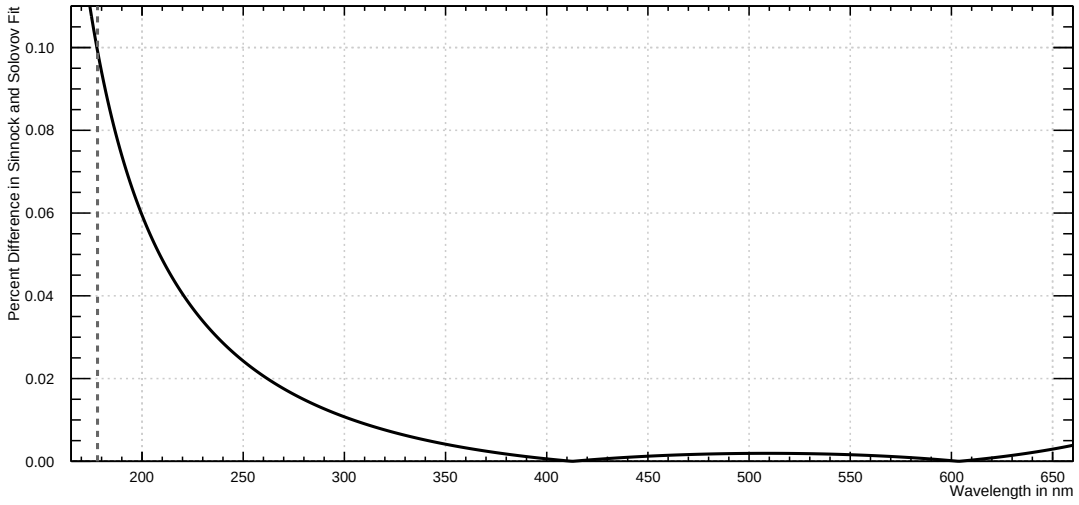

Figure 3.3: The percent difference between fit using Sinnock data points only and Sinnock and Solovov data points.

This validation test in liquid xenon is an indicator that fitting the data from Sinnock and Smith [1] with Equation 3.9 is effective in extrapolating the index of refraction from the measurements in in 660 - 350 nm to the scintillation wavelengths.

3.6 Results

3.6.1 Sellmeier Coefficients

The first step in analyzing the date from Sinnock and Smith [1] was to fit with Equation 3.9 and find the Sellmeier coefficients. (This data can be found in Table A.3, in the Appendix.)These will be useful in determining the index of refraction at any wavelength between the UV and IR resonances. The results of this fit can be found in Tables 3.3 - 3.5. In the case of liquid xenon at the triple point, the point from Solovov et al. [129] (shown in Figure 3.1)was included in the fit to improve the accuracy of the coefficients at this temperature.

T (K)	a_0	a_{UV}	a_{IR}	χ^2/ndf
Solid				
20	1.4±0.1	0.29±0.09	0.001±0.007	0.005/5
30	1.4±0.1	0.30±0.09	0.0005±0.007	0.005/5
40	1.3±0.1	0.30±0.09	0.0007±0.007	0.006/5
50	1.4±0.1	0.27±0.09	0.002±0.007	0.007/5
60	1.3±0.1	0.29±0.09	0.001±0.007	0.001/5
70	1.3±0.1	0.21±0.09	0.001±0.007	0.001/5
80	1.3±0.1	0.29±0.09	0.001±0.007	0.001/5
83.81	1.3±0.1	0.29±0.09	0.0009±0.007	0.004/5
Liquid				
83.81	1.243±0.09	0.27±0.09	0.0005±0.007	0.003/5
86	1.238±0.09	0.27±0.09	0.0008±0.007	0.003/5
88	1.234±0.09	0.27±0.09	0.0008±0.007	0.003/5
90	1.261±0.09	0.24±0.09	0.002±0.007	0.025/5

Table 3.3: Argon Sellmeier coefficients found by fitting the data (Table A.3 in Appendix) from Sinnock and Smith [1].

T (K)	a_0	a_{UV}	a_{IR}	χ^2/ndf
Solid				
80	1.6±0.3	0.6±0.2	0.001±0.03	0.0052/8
90	1.6±0.3	0.6±0.2	0.0009±0.03	0.0050/8
100	1.7±0.3	0.6±0.2	0.0009±0.03	0.0058/8
110	1.6±0.3	0.6±0.2	0.001±0.03	0.0050/8
120	1.5±0.3	0.6±0.2	0.0009±0.03	0.0051/8
130	1.5±0.3	0.6±0.2	0.001±0.03	0.0063/8
140	1.5±0.2	0.6±0.2	0.0009±0.03	0.0066/8
150	1.5±0.2	0.6±0.2	0.0008±0.03	0.0056/8
162.35	1.5±0.2	0.6±0.2	0.0008±0.03	0.0057/8
Liquid				
162.35*	1.536±0.02	0.380±0.01	0.00856±0.01	0.0040/8
166	1.4±0.2	0.4±0.2	0.001±0.02	0.0094/8
170	1.4±0.2	0.4±0.2	0.002±0.02	0.011/8
174	1.4±0.2	0.4±0.2	0.002±0.02	0.010/8
178	1.4±0.2	0.4±0.2	0.002±0.02	0.093/8

Table 3.4: Xenon Sellmeier coefficients found by fitting the data (Table A.3 in Appendix) from Sinnock and Smith [1]. *This Fit includes the point from [129]. Including this point improves the error on the fit by a factor of 10.

T (K)	a_0	a_{UV}	a_{IR}	χ^2/ndf
Solid				
67	1.5±0.1	0.4±0.1	0.004703±0.01	0.06/5
75	1.5±0.1	0.4±0.1	0.004693±0.01	0.06/5
85	1.4±0.1	0.4±0.1	0.004140±0.01	0.09/5
95	1.4±0.1	0.4±0.1	0.004479±0.01	0.09/5
105	1.4±0.1	0.4±0.1	0.004531±0.01	0.08/5
115.95	1.4±0.1	0.4±0.1	0.004214±0.01	0.06/5
Liquid				
115.95	1.4±0.1	0.28±0.08	0.004±0.01	0.05/5
118	1.4±0.1	0.28±0.094	0.004±0.01	0.05/5
122	1.4±0.1	0.28±0.09	0.004±0.01	0.06/5
126	1.4±0.1	0.28±0.09	0.004±0.01	0.07/5

Table 3.5: Krypton Sellmeier coefficients found by fitting the data (Table A.3 in Appendix) from Sinnock and Smith [1].

3.6.2 Index of Refraction and Rayleigh Scattering Lengths

The Sellemeier coefficients obtained by fitting the data from Sinnock and Smith [1] were then used to extrapolate the index of refraction and Rayleigh scattering length at the scintillation wavelengths. The extrapolations are graphically depicted in Figures 3.5 - 3.7. In the graphs of the index of refraction, the original data points from [1] are included. In the case of xenon, only the values for solid xenon were extrapolated since the values for liquid xenon have already been measured.

T (K)	n	l (cm)
Solid		
20	1.52±0.07	149±4
30	1.53±0.07	97±10
40	1.52±0.074	75±8
50	1.51±0.07	67±7
60	1.51±0.07	53±5
70	1.51±0.07	47±5
80	1.50±0.07	42±4
83.81	1.50±0.07	40±4
Liquid		
83.81	1.46±0.07	55±5
86	1.45±0.07	54±5
88	1.45±0.07	54±5
90	1.43±0.07	62±6

Table 3.6: Solid and liquid argon index of refraction and Rayleigh scattering length extrapolations at the scintillation wavelength. This uses the densities as given by Sinnock and Smith [1] were used to calculate the Rayleigh scattering length. 83.81 K is the argon triple point.

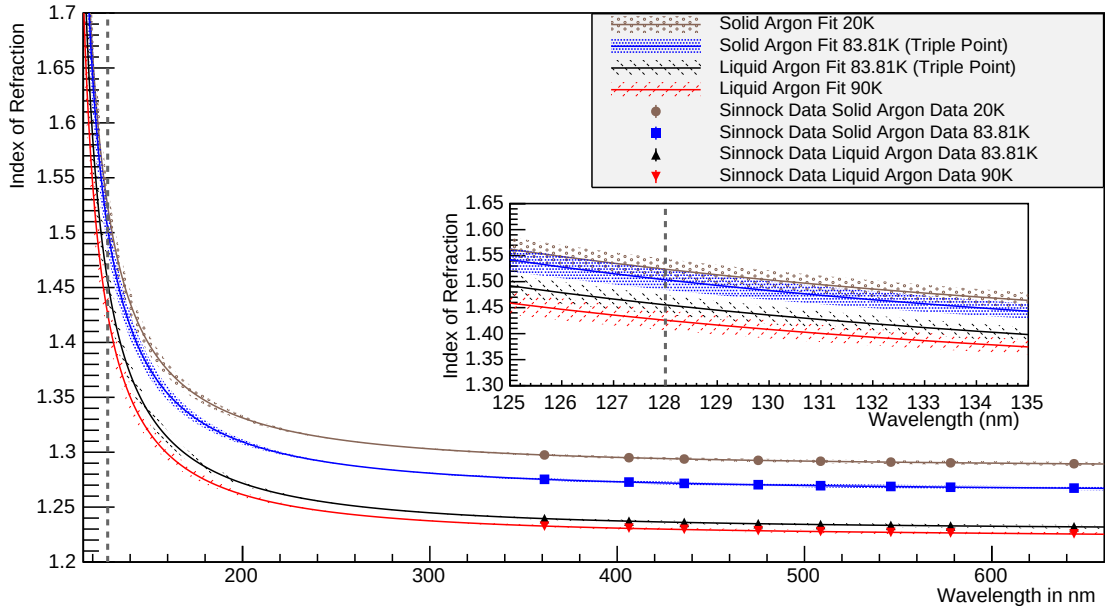

Figure 3.4: The index of refraction for argon extrapolation. The x axis is wavelength in nanometers (nm) and the y axis is index of refraction. A dashed line is placed at 128 nm, the scintillation wavelength of Argon.

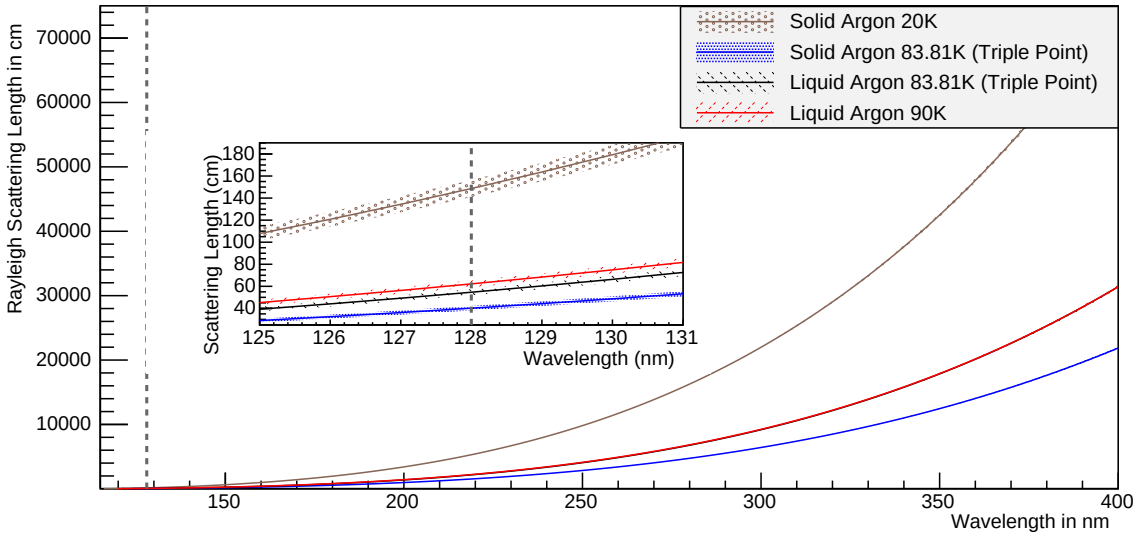

Figure 3.5: The Rayleigh scattering length of argon extrapolation. The x axis is wavelength in nanometers (nm) and the y axis is Rayleigh scattering length in centimeters. A dashed line is placed at 128 nm, the scintillation wavelength of Argon.

T (K)	n	l (cm)
Solid		
67	1.67±0.09	41±4
75	1.67±0.09	37±4
85	1.67±0.08	32±4
95	1.66±0.08	30±3
105	1.66±0.08	28±3
115.95	1.65±0.08	26±4
Liquid		
115.95	1.54±0.08	48±5
118	1.55±0.08	48±5
122	1.53±0.07	47±4
126	1.53±0.07	46±4

Table 3.7: Solid and liquid krypton index of refraction and Rayleigh scattering length extrapolations at the scintillation wavelength. This uses the densities as given by Sinnock and Smith [1] were used to calculate the Rayleigh scattering length. 115.95 K is the krypton triple point.

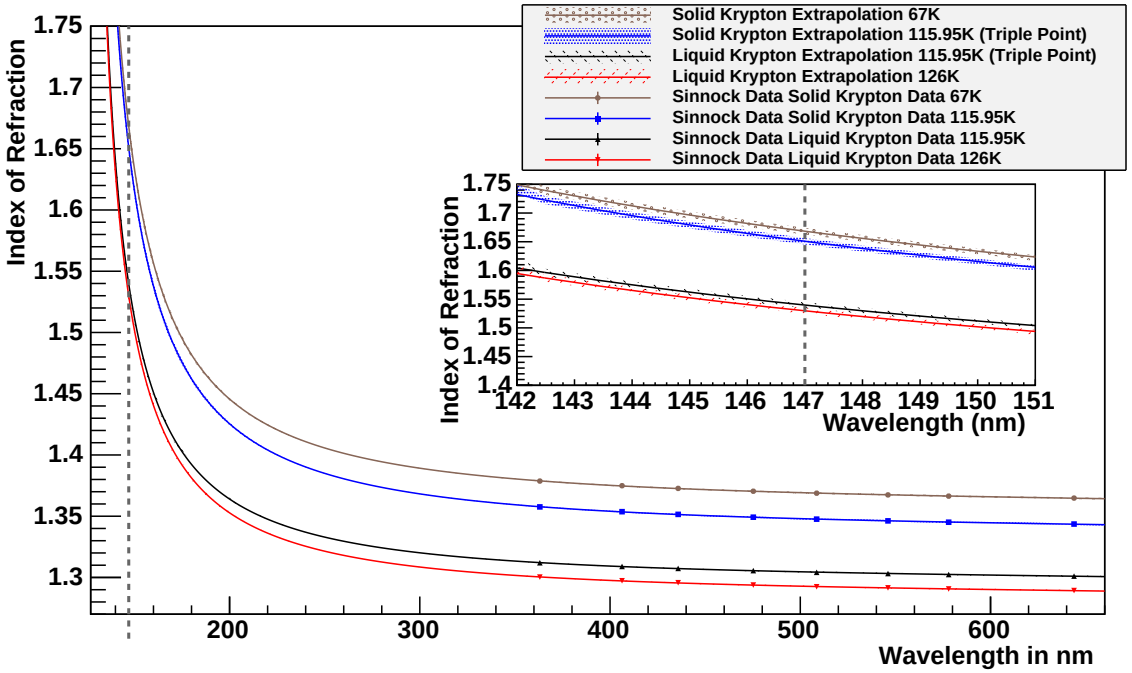

Figure 3.6: The index of refraction for krypton extrapolation. The x axis is wavelength in nanometers (nm) and the y axis is index of refraction. A dashed line is placed at 147 nm, the scintillation wavelength of krypton.

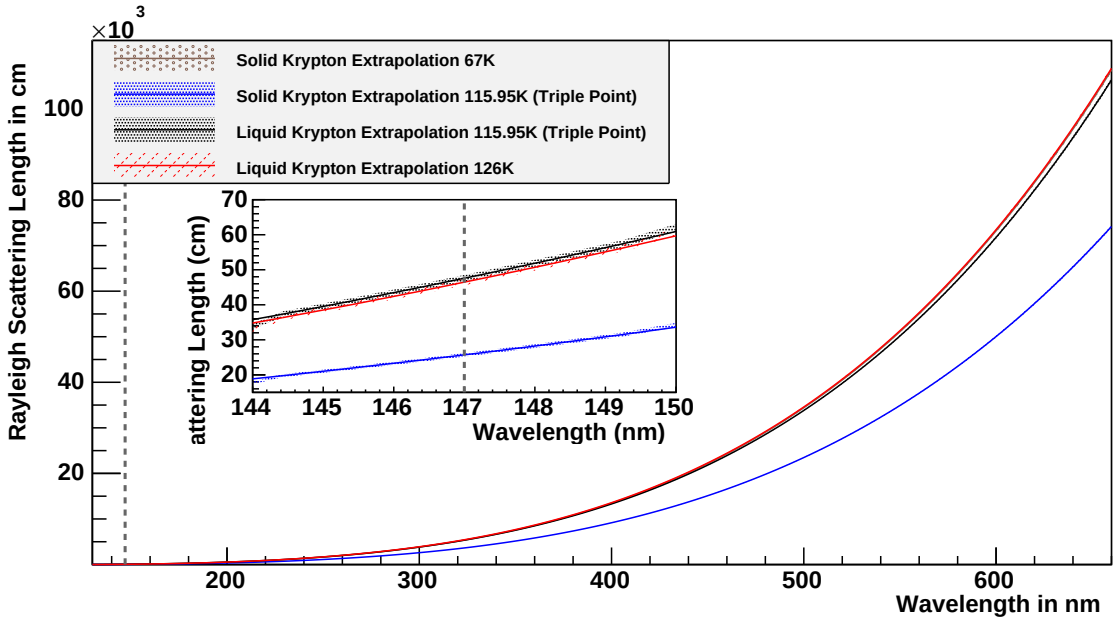

Figure 3.7: The Rayleigh scattering length of krypton extrapolation. The x axis is wavelength in nanometers (nm) and the y axis is the Rayleigh scattering length in centimeters (cm). A dashed line is placed at 147 nm, the scintillation wavelength of krypton.

T (K)	n	l (cm)
Solid		
80	1.90±0.03	25±2
90	1.90±0.04	23±2
100	1.89±0.04	21±1
110	1.89±0.04	19±1
120	1.89±0.04	18±1
130	1.88±0.03	17±1
140	1.88±0.03	16±1
150	1.87±0.03	15±1
162.35	1.87±0.03	14±1
Liquid		
162.35	1.69±0.04	35±2
166	1.69±0.03	35±2
170	1.68±0.03	36±2
174	1.68±0.03	35±2
178	1.67±0.03	35±2

Table 3.8: Solid and liquid xenon index of refraction and Rayleigh scattering length extrapolations at the scintillation wavelength. This uses the densities as given by Sinnock and Smith [1] were used to calculate the Rayleigh scattering length. 162.35 K is the argon triple point.

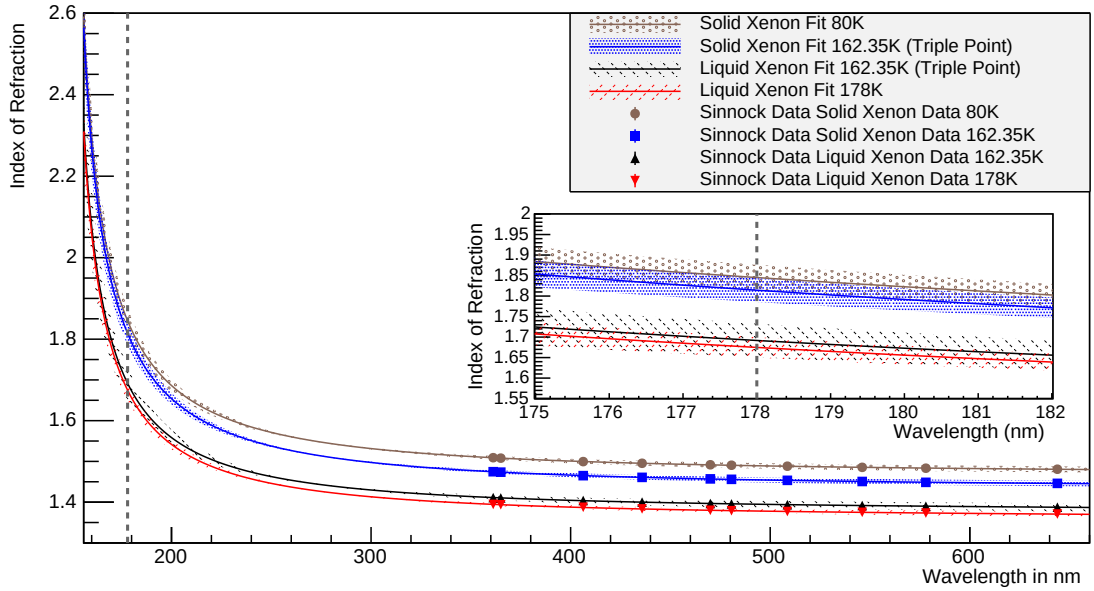

Figure 3.8: The index of refraction for xenon extrapolation. The x axis is wavelength in nanometers (nm) and the y axis is index of refraction. A dashed line is placed at 178 nm, the scintillation wavelength of xenon.

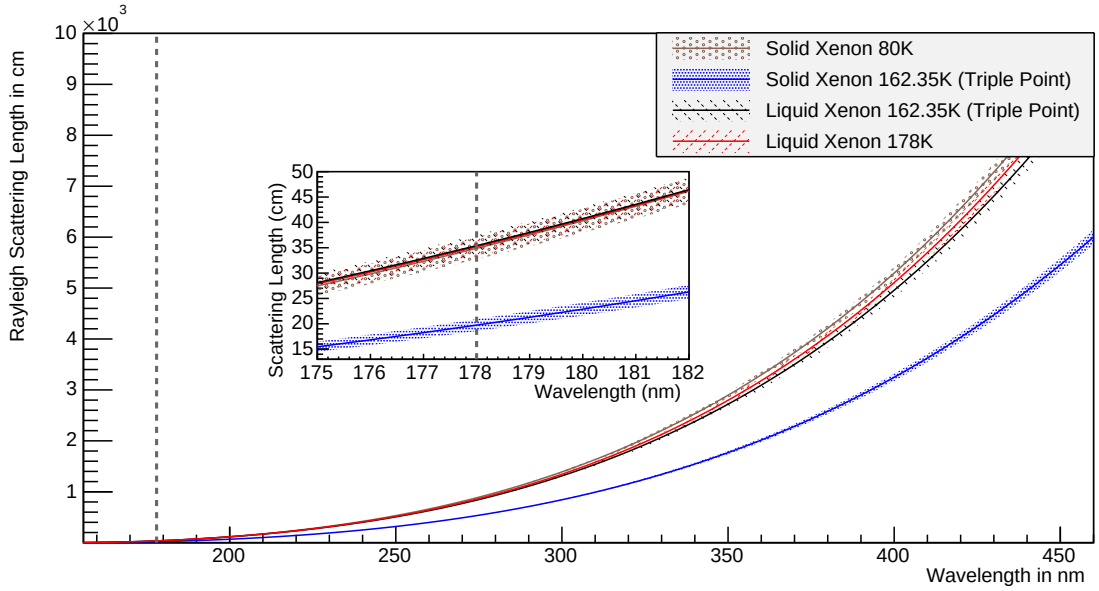

Figure 3.9: The Rayleigh scattering length of xenon extrapolation. The x axis is wavelength in nanometers (nm) and the y axis is Rayleigh scattering in centimeters (cm). A dashed line is placed at 178 nm, the scintillation wavelength of xenon.

3.7 Discussion

Large liquid noble detectors rely on precise optical information for event reconstruction. In the case of liquid argon there is a discrepancy between the measured value and Seidel et al's extrapolated value. However, the extrapolation done by Seidel et al [104] was done over a 200 K temperature change and a phase transition. The extrapolation using the data from Sinnock et al [1] extrapolated the wavelength dependency through argon at constant temperature and state. The extrapolated Rayleigh scattering length of liquid argon at 88 K is 54±5cm. This is closer to the value measured by Ishida et al [122] than the extrapolated value by Seidel et al [104] as seen in Table 7.1. The extrapolated value is within error the value measured in situ by ArDM in 2016 [133]. The accuracy of the extrapolation method was tested against a measured point in xenon and the value was

	n			l (cm)		
Element	**Updated Analysis**	Previous Calculation	Previous Measurement	**Updated Analysis**	Previous Calculation	Previous Measurement
Liquid Argon	1.45 ± 0.07	1.37	N/A	55±5	90	66 ± 3
Liquid Krypton	1.54 ± 0.08	1.51	N/A	58±5	60	82 ± 4
Liquid Xenon	1.73 ± 0.03	1.68	1.69±0.02	26±2	30	29 ± 2
Solid Argon	1.50 ± 0.07	N/A	N/A	40±4	N/A	N/A
Solid Krypton	1.65 ± 0.08	N/A	N/A	26 ± 4	N/A	N/A
Solid Xenon	1.87 ± 0.03	N/A	N/A	14±1	N/A	N/A

Table 3.9: This a summary of the results of extrapolations made by fitting the Sinnock data at the triple point with the Sellmeier equation. Both the liquid and solid triple point values are included. These values are compared with previous calculations and measurements. The previous index of refraction and Rayleigh scattering length calculation come from [104]; error bars were not included in the original work. The previous argon scattering length measurements come from [120] and the previous xenon index of refraction measurement is from [129].

predicted within experimental error.

The krypton extrapolation is not within error of either the measurement by Ishida et al [122] or the extrapolation by Seidel et al [104] as shown in Table 7.1. This could be for a number of reasons. In Ishida et al's method there were technical issue with the scintillation beam during the krypton measurements. Also, in the Sinnock and Smith measurements, [1] the authors noted anomalies in the krypton measurements which may have been related to the quality of the krypton used. The issues with krypton in the Sinnock and Smith measurement were discussed in greater detail in a thesis document on the experiment [128], but were not added to the error in the final paper with no explanation given as to the motivation behind this omission. Further measurements on krypton will need to be made in order resolve this matter.

The data taken by Sinnock *et al.* [1] also gave us the opportunity to produce values for the index of the refraction and Rayleigh scattering lengths of solid argon and xenon

at different temperatures at the scintillation wavelengths. These values may be useful in future detectors or experiments that take advantage of the scintillation properties of these elements in a solid state. All of the results for the index of refraction and Rayleigh scattering length are collected in Table 7.1.

Chapter 4

Test Stand Design and Construction

Scientific progress is the discovery of a more and more comprehensive simplicity... The previous successes give us confidence in the future of science: we become more and more conscious of the fact that the universe is cognizable. - Monsignor Georges Lemaitre

4.1 Introduction

This chapter describes the development of the Rayleigh scattering experimental concept as the construction of a test stand. The test stand was developed using simulations of potential test stand geometry models. The results of which were implemented into the design decisions for the detector stand.

The concept for Rayleigh scattering experiment is to have a long tube of liquid argon with a photon detector at one end. The argon will be scintillated a different lengths from the photon detector and the number photons that arrive at the photon detector will scale as function of the solid angle,

$$I_{\Omega}(x) = I_0 \left(\frac{d}{x}\right)^2, \tag{4.1}$$

where I_Ω is number of photons detected by the photon detector as a result of solid angle, I_0 is the number of photons produced at the scintillation event, x is the distance of of the scintillation event from the photon detector and d is the diameter of the tube. This relationship can easily be calculated and modeled. Furthermore, the number of photons detected should scale as a function of attenuation length, or Beer-Lambert Law [138][139],

$$I_l(x) = e^{-x/l}, \tag{4.2}$$

where is I_l is x is the distance of the scintillation length from the photon detector as result of Rayleigh scattering length and l is the Rayleigh scattering length. The photon count will also be impacted by the optical properties of the materials and components used in the measurement. This includes the efficiency of detectors and the transmission of any windows used. This is described by:

$$I(x) = I_0 \left(\frac{d}{x}\right)^2 e^{-x/l}, \tag{4.3}$$

For simplification, we let

$$A = I_0 d^2, \tag{4.4}$$

since $I_0 d^2$ are constants for each measurement. Thus, the fraction of photons detected as a function of scintillation distance from the photon detector is described as

$$I(x) = \left(\frac{A}{x^2}\right) e^{-x/l}. \tag{4.5}$$

This starting point in the detector design. The chapter describes the process for designing a geometric model used as a guide to construct a test stand. The discussion

of the geometric model is followed by a description of the scattering test stand built at RHUL.

4.2 Test Stand Development: Physical Detector & GEANT4 Geometric Model

4.2.1 Internal Vessel

The internal vessel (IV) is constructed of copper and is 150 cm in length. The internal diameter is 5.83 cm. One end of the IV, there is an MDC conflat flange [140] with a window installed so that the scintillation light can pass through to be detected by the PMT. At the other end, there is second MDC conflat flange [140] which connected to a stainless steel tube. This was used in the experiment for fridge and vacuum components. This tube is 1.84 cm in length and has an internal diameter of 3.33 cm. The geometric model is shown in Figure 4.1.

Figure 4.1: A visual representation of the simplest GEANT4 geometry model used to test the experimental concept. CF flanges(1), a stainless steel tube containing (2), a copper tube containing liquid argon (3), a TBP coated acrylic window coupled to a sapphire viewport (4), and a PMT (5).

When the physical vessel was installed it was wrapped in 7 layers of super insulation to maintain a constant temperature. Attached to the copper inner vessel was a stainless steel T section in which the pipes for the argon gas and vacuum system were attached. The inner vessel was supported inside of the outer steel vessel using a vacuum compatible resin collar and nylon strews. This was done to minimize conductive thermal contact with the outer vessel. An image of the physical inner vessel is shown in Figure 4.2

Figure 4.2: An image of the inner vessel before it was installed in the outer vessel. It is attached to vacuum system.

Window

An acrylic window, 4.9 cm in diameter, is coated with tetra-phenyl butadiene (TPB, $C_{28}H_{22}$) wavelength shifter, which serves to shift the VUV light generated by argon scintillation to 420 nm [141]. This is then coupled with a sapphire window viewport [142]. A sapphire window was chosen since it can withstand greater pressures than a glass window [143]. The transmission of a sapphire window is around 85% for 420 nm light (see Figure 4.3), as compared to 92% for a glass window.

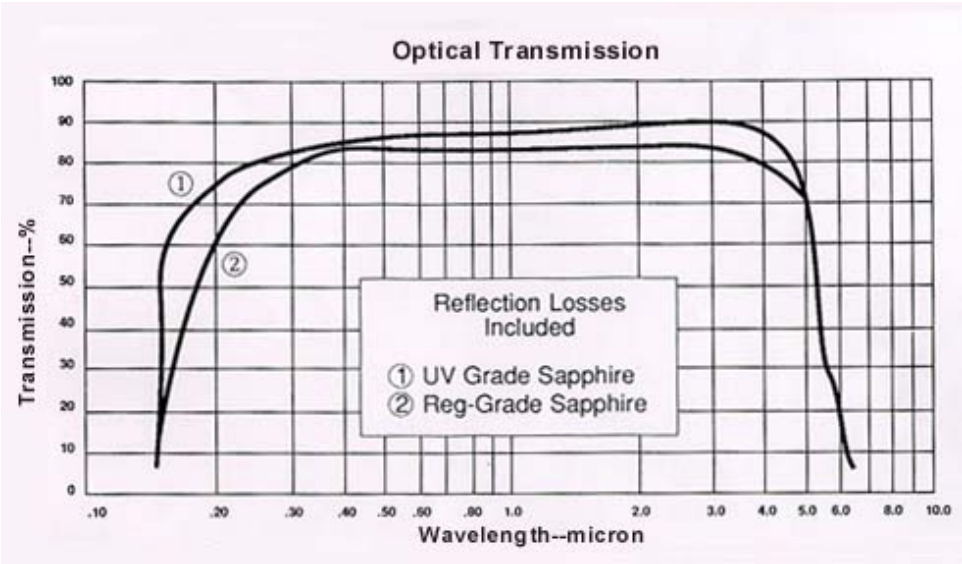

Figure 4.3: This a plot showing the transmission curve [144] of the sapphire window. The x axis is light wavelength in microns and the y axis is percent transmission. Line 2 corresponds the the sapphire used in the experiment.

The light generated in the detector would reach the TPB coating first. This shifts the wavelength to 420 nm through re-emission. The light then travels through the acrylic window, followed by the sapphire window. This light is then detected by the PMT.

The physical window used was coated using a TPB evaporation deposition system at the University of Sussex [145]. The coating was estimated to be about 0.6 microns based on previous applications of this system [145]. This widow was then placed against the sapphire window view port. The window used in simulation is shown in Figure 4.4.

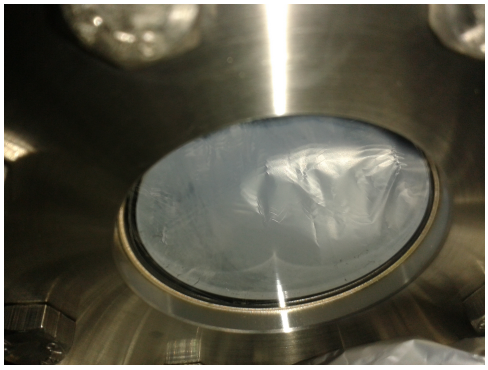

Figure 4.4: An image of the window. This has been coated with TPB.

Internal Coating

Black Sheet Coating One of the background concerns for the experiment was the impact of internal reflections from the inner vessel. Two types of internal coatings were modeled. A completely absorptive coating was modeled to understand the signal under zero reflection conditions. This is used as a baseline to understand the impact of the additional reflections contributed by the spectral black coating.

Spectral Black Coating The second internal coating that was modeled is spectral black, a coating manufactured by Aktar Limited [146]. Spectral black is a highly absorptive coating with a reflectance that is extrapolated to be under 2% reflectance at 128 nm wavelength and just over 2% at 420 nm as see in Figure 4.5. It is rated for cryogenic applications, clean rooms, and does not outgas, making it suitable for the Rayleigh test stand experiment.

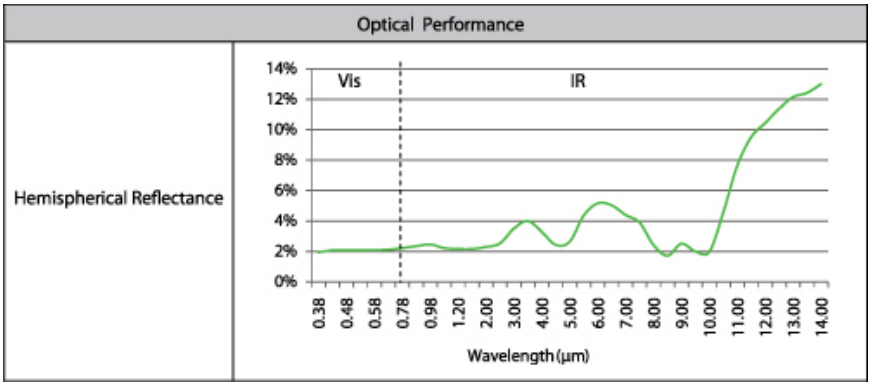

Figure 4.5: A figure from Aktar website [146]. The x axis is wavelength and the y axis is percent reflection. This information was used to generate the optical properties of spectral black in the simulation. These values were extrapolated to 128 nm.

Rear Baffles

To minimize reflections from the rear of the detector two rear baffles were simulated. These baffles had a diameter of the inner vessel and were coated in spectral black. Two baffles were simulated. These were placed at 140.0 cm and 144.0 cm away from the window. One had three 0.1 cm hole and the other and four 1 cm holes, which were intentionally misaligned. Simulations were done using an isotropic photon bomb of 10 million photons placed at 145 cm away from the window and 1 cm away from the nearest baffle. The PMT in simulation did not detect any photons generated in this region. This was sufficient to implement these baffles into the design of the detector to further reduce the contribution of photons from reflection at the rear of the detector.

4.2.2 Stainless Steel Outer Vessel and External Components

The external stainless steel vessel was composed of two parts: the PMT enclosure and the IV enclosure. The diameter of the PMT enclosure is 24.8 cm. The length of this section is 50.0 cm.

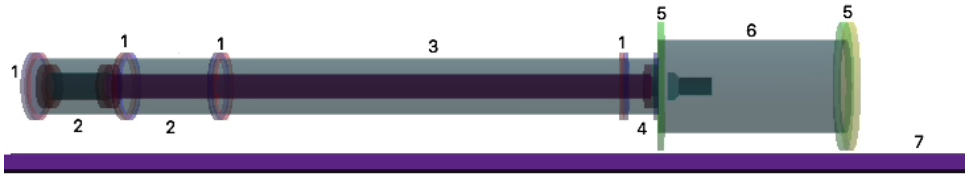

Figure 4.6: A visual representation of the simplest GEAN4 geometry model used to test the experimental concept. This is image of the outer steel vessel. This includes stainless steel flanges (1), the stainless steel (2), the stainless steel vacuum vessel that houses the argon tube (3), the internal flange that houses the window(4), the stainless steel vacuum vessel that house the PMT(5), and the PMT in the vacuum vessel (6). Internal photon bomb simulations were done through the length of the internal vessel.

The physical outer vessel is show in Figure 4.7.

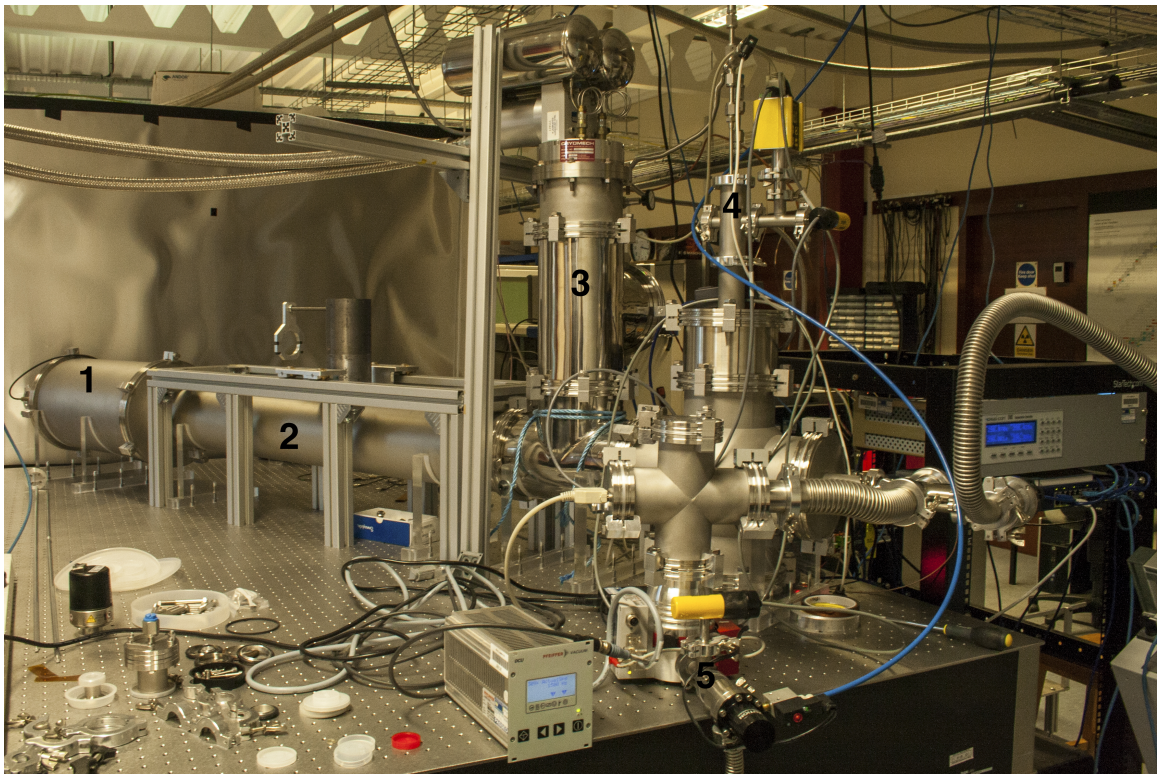

Figure 4.7: An image of the the stainless steel outer vessel. 1 is where the PMT is located. 2 is the location of the copper tube used for the liquid argon. 3, this where the cold head for the fridge is located.

Lead Collimators

Collimators in Simulation In order to determine where events occurred in the detector, the radioactive sources needed to be collimated with lead. These collimators were cylindrical with an opening in the middle. The diameter of the lead collimators was limited by the material availible at RHUL. The overall diameter could not exceed 8.0 cm and the opening could not be less than 1.0 cm. The height of the collimators was determined using the following equation,

$$I = I_0 e^{-\mu/\zeta t}. \tag{4.6}$$

Where I_0 is the intensity of the source, μ is the attenuation coefficient for lead for the gamma energy looked from NIST [147], t is the thickness of lead, ρ is the density of lead (11.34 g/cm^3) and I is the intensity. The values for μ for lead can be found in Figure 4.8.

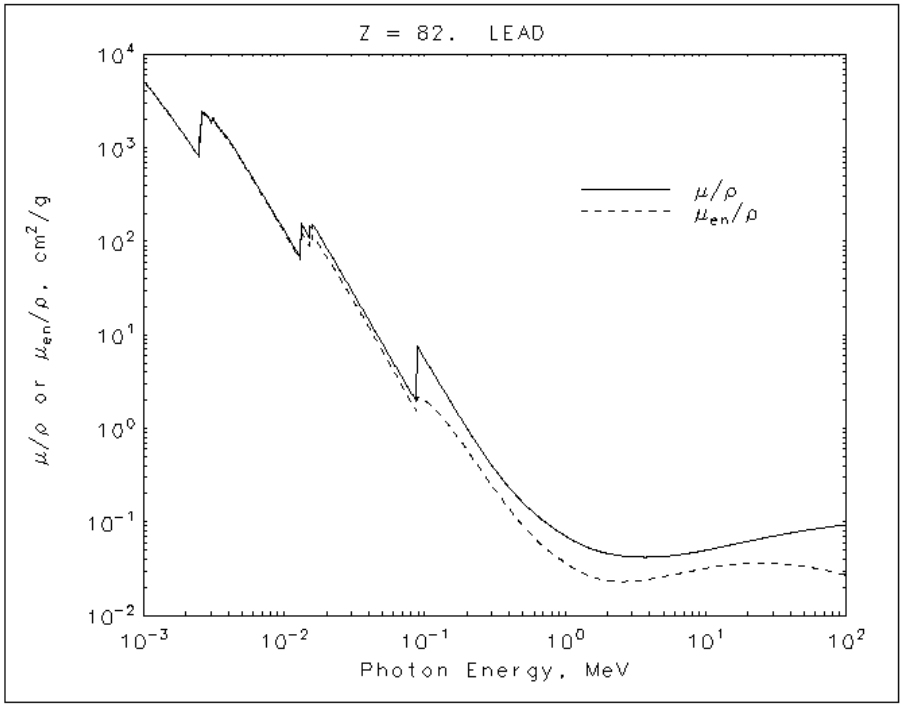

Figure 4.8: A graph of the lead attenuation coefficient as function of gamma energy from [147]. The x-axis is the coefficient and the y axis is the energy of the gamma in MeV.

	5 cm collimator height		10 cm collimator heigh	
	% Transmission	δ x (cm)	% Transmission	δ x (cm)
511 keV ^{22}Na	1.0×10^{-2} %	2.6	1.1×10^{-6} %	1.8
661 keV ^{137}Cs	8.5×10^{-2} %	2.6	7.1×10^{-5} %	1.8
1274 keV ^{22}Na	3.6 %	2.6	1.3×10^{-1} %	1.8

Table 4.1: A table comparing the effectives of different size collimators in attenuating different gamma energies. This includes the resolution of events in the x axis.

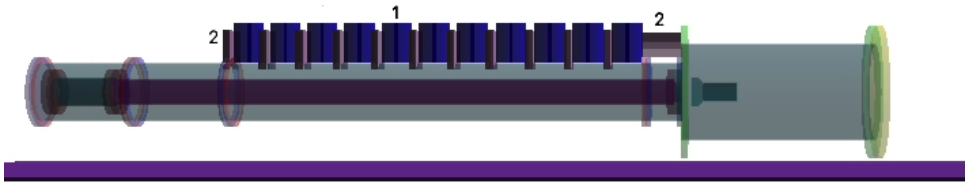

Figure 4.9: A visual representation of the simplest GEANT4 geometry model used to test the experimental concept. This is the outer vessel with the lead collimators (1) and lead shielding blocks (2) in place. The radioactive source was simulated in the center of each column.

Collimators in Experiment For the experiments, 6 cylindrical lead collimators were constructed. All of these were 8 centimeters in over all diameter. 5 collimators were 10 cm in length and 1 collimator was 5 cm in length. Each collimator had 1 cm diameter opening. A lead source cap was also fashioned to place on top of the collimators (Figure 4.10). This was 10 cm in length and had a 4.5×4.5×3.5 cm opening for the source and tagging PMT installation. This was used to further shield background radiation from the source. For the tagging system (discussed later in the chapter), the tops of the collimators were coated in black foam (Figure 4.11). This was to prevent any light leaks for the tagging PMT.

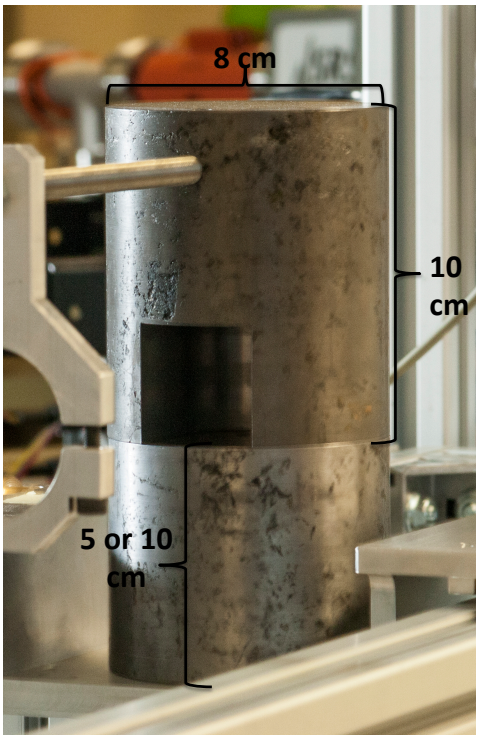

Figure 4.10: A close up of the collimator with the source cap.

Figure 4.11: The collimators with black foam used for a light seal. Between each collimator is a lead block to reduce background from the source

Lead Blocks

To prevent contamination background from using a gamma source, lead blocks were used in the simulation to attenuate radiation. In the simulation, these blocks were $50 \times 50 \times 10$ cm. These blocks were placed between the simulation collimators and on the two ends of the outer vessel. The lead used in the physical experiment was lead found in the lab. The source and purity of the lead was unknown and may have had impurities that may be altered the background reduction comparison between experiment and simulation.

4.3 Simulations in RAT

The test stand was developed through geometric modeling and simulations. The simulations were done using a custom software package called RAT. RAT is a custom software developed by Stan Seibert [148] and is used for optical simulations in DEAP/CLEAN. This software utilizes both ROOT [149] and GEANT4 [150].

Simulations followed a basic format; a simulation of events was done a different lengths along the detector and the number of photons detected by the photon detector were analyzed. In simulations, different types of simulated events were used. A simulation event a single particle in simulation (e.g. photon, gamma, beta, etc.).

4.3.1 Simulation Argon

In order to do simulation effectively, the optics for three different argon's were written. The difference between these three simulation mediums was the optical scattering length. This was done using equation 4.2. Simulated argon was developed with three scattering lengths: 66 cm, 90 cm, and zero scattering. These were chosen to reflect the previous measurement [120] and extrapolation [104], at the time of simulation. The zero scattering

was developed as control.

Isotropic Photon Bombs Detector models were tested using an ideal physics simulation. This consistent of generating isotropic photons generating from single point. These are called photon bombs in the RAT simulations. These use a predetermined wavelength. In simulations, the wavelength typically used was 128 nm, the argon scintillation light wavelength. Simulations were sometimes done using a wavelength of 420 nm, the peak wavelength for the PMT. In most simulations, each photon bomb consisted of 10,000 photons. This would be repeated a number of times according to the desired statistics needed. These simulations were used to understand the detector geometry and in studies of optical tracking.

Isotropic Gamma Sources The most realistic simulations were done using isotropic gamma simulations. These model sources most accurately. It consists of gammas being generated isotropically from a single point. These were used in simulations with the lead collimators.

4.3.2 Detecting Signal in Simulation

PMT The output of the simulations was detected by a PMT generated within the geometric model. This PMT can be found in Figure 4.5 and was based on the specs of a Hammatsu R6091. The PMT in simulation had a diameter of 7.60 cm. The quantum efficiency in simulation was 32%.

In simulation, photoelectrons were counting using the following method. The charge on the PMT was recorded. This reading was converted to photo electrons using the charge conversion listed for the PMT model. In the case of the Hammatsu R6091, the conversion

is

$$1PE = 0.8pC. \tag{4.7}$$

4.3.3 Scattering Simulations

The next test in simulation was to see the scattering length simulated could be recovered. Simulations were done using all three simulation argon settings. A cursory background subtraction was done by using the infinite scattering condition. For both the 90 cm scattering condition and the 66 cm scattering condition, the scattering length input was recovered by fitting the results with Equation 4.5. This can be seen in Figure 4.12 and 4.13.

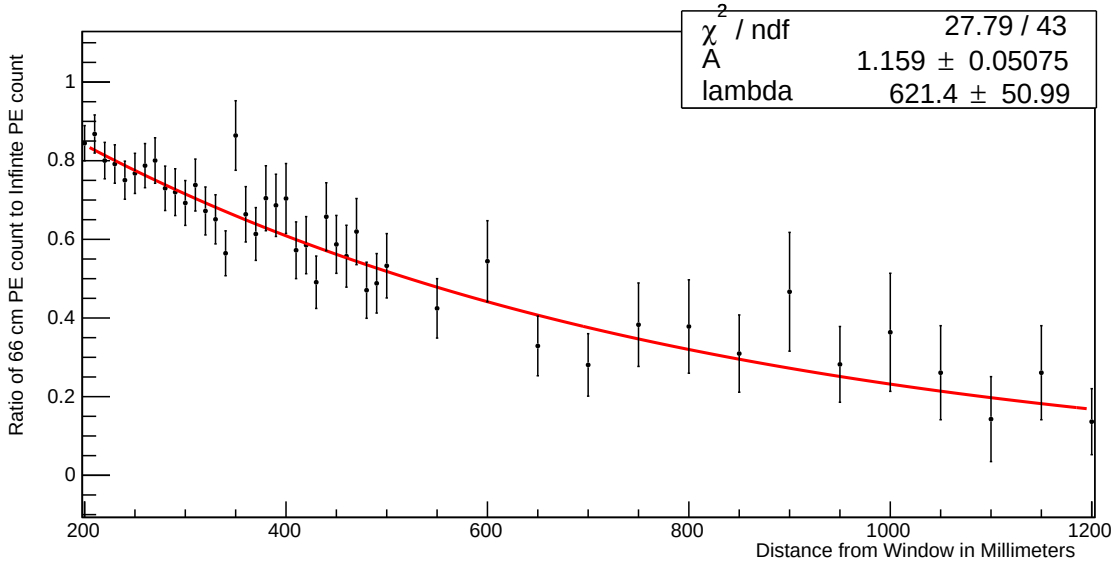

Figure 4.12: Simulation using argon with 66 cm scattering length. The x axis is position in cm and the y axis is the integral value of PE/s. This has been fit with Equation 4.5.

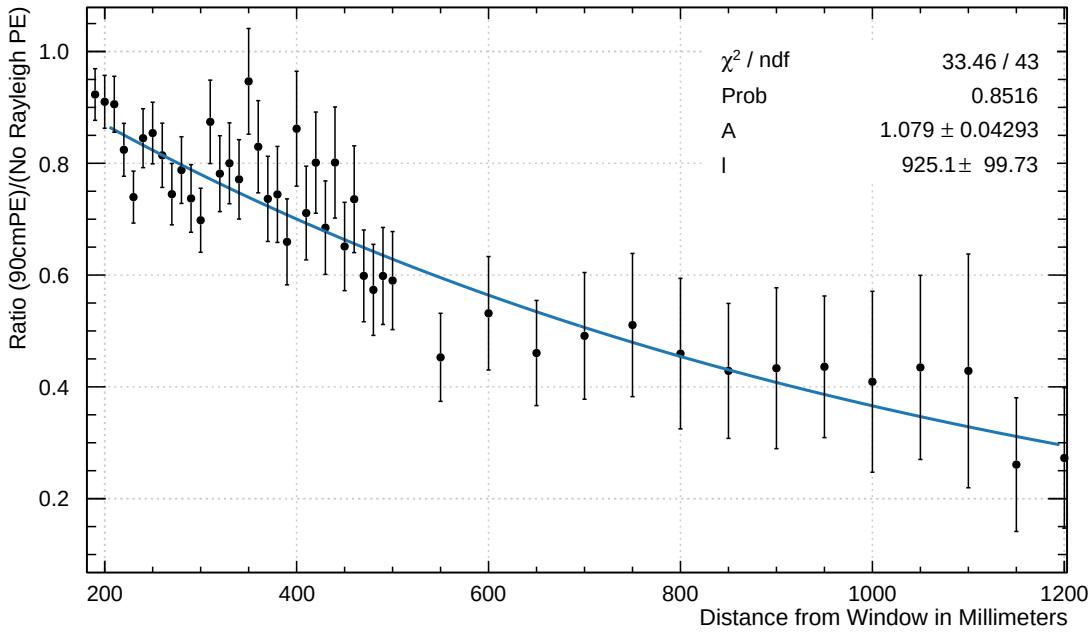

Figure 4.13: Simulation using argon with 90 cm scattering length. The x axis is position in cm and the y axis is the integral value of PE/s. This has been fit with equation 4.5.

4.3.4 Front Aperture

Front Aperture Simulation Study

An additional study that was conducted compared the percent reflection with spectral black coating as a function of aperture size. This was done to test methods of further reducing photons detected via material reflection. Apertures of sizes 4.0 cm, 2 cm, 1 cm, 0.5 cm, and 0.1 cm were used. In this study 10 million isotropic photons were simulated 50.0 cm away from the window. The path of the photons detected by the PMT in simulation were tracked. The percentage of photons that reached the window in the black sheet condition was compared to the number of photons that reached the window the spectral black setting. In black sheet, all photons on arriving at the window should be absorbed.

No photons should arrive at the window via reflection. Therefore additional photons in the spectral black condition could be attributed to reflection at the baffle. The results are found Table 4.2.

Front Aperture Size (cm)	Black Sheet Photons	Spectral Black Photons	Percent Difference
4*	4376	4591	4.9%
2*	1122	1154	2.9%
1	286	293	2.4 %
0.5	64	63	-1.6%
0.1	2	2	0%

Table 4.2: 10 million isotropic photons were simulated at a 50.0 cm distance from the window using different front aperture sizes and absorptive coatings. Black sheet is completely absorbing and spectral black is mostly absorbing. The number of photons counted are the number that have reached the window. *These are the baffle sizes used in the actual experiment.

For this study, it was determined that a 4.0 cm baffle could have as much as 5% of the photons from reflection, a 2.0 cm baffle might detect as many as 3% of photons from reflection and a baffle of 0.5 cm would minimize the percentage of photons reflected via reflection to a statistically insignificant number.

4.3.5 Front Aperture in Experiment

Three copper apertures were used throughout the experiment. The diameter sizes are as follows, 4.0 cm, 0.2 cm, and 0.5 cm. All of these apertures were coated in spectral black. This was done by folding the black foil around the apertures. An example apertures can be see in Figures 4.15 and 4.14. The folds of spectral black were then used to secure the

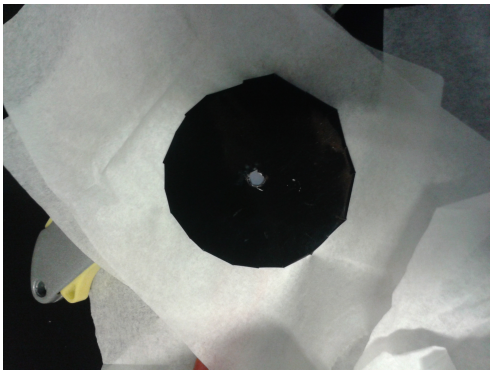

Figure 4.14: An image a baffle used in the detector. The spectral black coating has been folded around the edges to absorb stray light.

Figure 4.15: Spectral black folded around the front aperture to secure the TPB coated acrylic window.

acrylic window.

4.4 Test Stand Experimental Sensor SetUp and DAQ system

The following section goes through the various sensors used within the experiment as well as the method of data acquisition.

4.4.1 Sensors

LakeShore germanium [151] temperature sensors were placed at three places on the outside of the inner vessel. One temperature sensor was place 4cm away from the window on the outside of the copper tube. A second temperature sensor was placed in the middle of the copper tube. (This temperature sensor failed after the first argon fill.) The third sensor was placed at the far end of the internal vessel. A fourth sensor was mounted to the second stage of the refrigerator. These were monitored by a Lakeshore model 218 temperature monitor [152] as well as the slow control. The sensors were accurate with 0.001 of a degree

K [151]. A conductive level sensor meter was place placed at the far end of the inner vessel to monitor the argon fills and the level of liquid argon throughout the data acquisition process. A hornet pressure monitoring system was used to measure the vacuum pressure.

4.4.2 Slow Control

To monitor the system, a computer interface slow control was used, which could also be accessed remotely. The slow control kept a log of the temperature, pressure, level meter, vacuum pressures, as well as the state of the cryocooler throughout measurements. The DCDAQ code was used to write the average pressure and temperature from a data run to a root file using the data stored in the slow control. The temperature of the refrigerator stage could be controlled via slow control. The cryogenic pump could also be turned off remotely via the slow control.

4.4.3 Argon

The argon used for the experiment had a quality rating of N6.0 (99.9999%) [153]. It was further purified by passing through a Saes MonoTorr heated getter [81], pictured in Figure 4.16. The getter removes H_2O, O_2, CO, CO_2, H_2, N_2, and hydrocarbons to less than 1 parts per billion. The cleanliness of the argon used in the experiment was verified using the triplet lifetime shown in Chapter 5.

Figure 4.16: Image of the MonoTorr Heated gas getter used in the experiment.

Gas Handling System

A gas handing system was designed for this experiment. This system incorporated methods to clean the argon. It is designed both to fill chamber with argon and to remove the gaseous argon. (Argon flushes were used as part of the filling procedures and the argon was removed via this system in the final decommissioning.) It was also designed to pass the argon through a chiller, when in cool down mode. This began the liquefaction of the argon. The system is detailed in Figure 4.17.

The gas flow into the detector was as follows. The valve to the gas container was opened and the argon was released into the manifold. The pressure on the manifold was monitored by a gas gauge and kept at 1 bar. A valve was located after the manifold to release the gas into part of the copper gas line. The gas was released further into the gas

line by a second valve. A third valve was located before the Saes MonoTorr heated gas getter [81]. This released the gas into the getter for further purification. A fourth valve was located after the getter. This released the gas into the final line before entering the vessel. The final valve released the gas into the inner vessel.

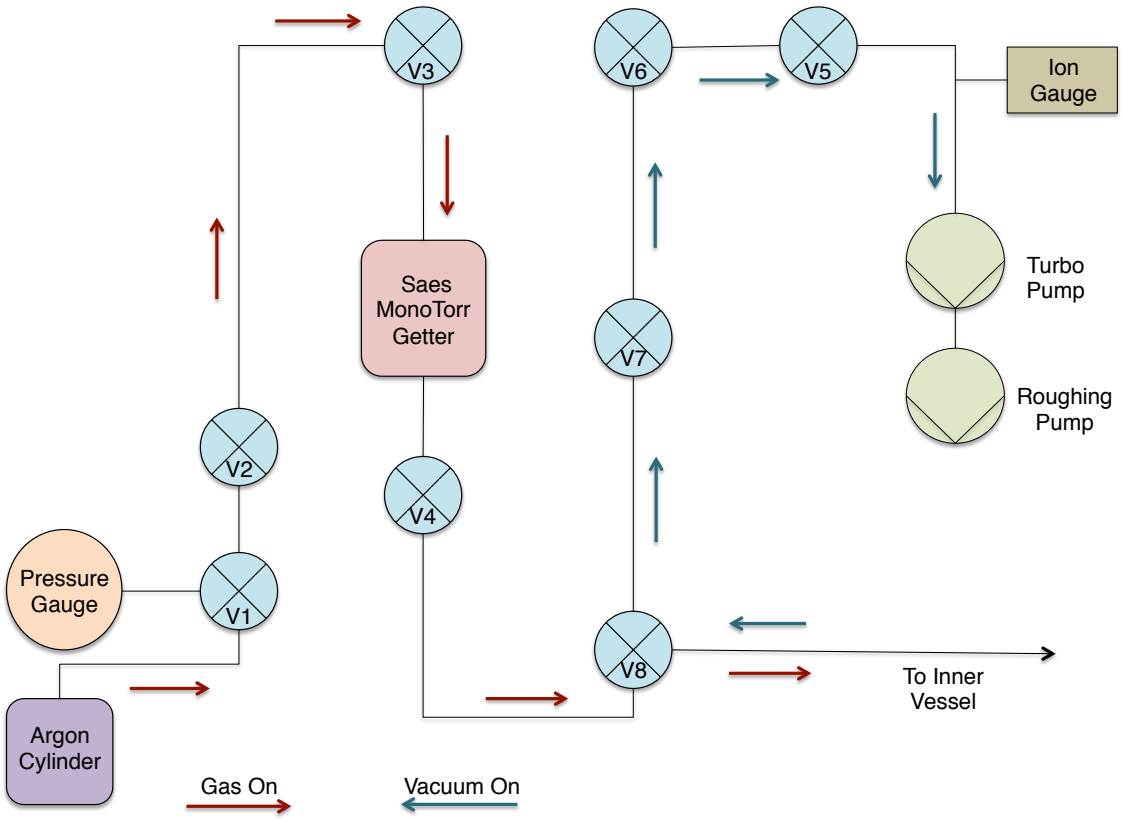

Figure 4.17: Schematic diagram of the gas handling system. The red arrows indicate the direction of flow when the gas is turned on and the vacuum is off. When the argon gas is on valves V1- V4, and V8 are turned on and valves V4-V7 are turned off. The blue arrows indicate the direction of flow when the gas is off and the vacuum is off. When the vacuum is on valves V4-V8 are turned on, and valves V1-V4 are off. Valve V1 is a part of BOC cylinder manifold [154]. Valves V2 - V8 are Swagelok ball valves [155].

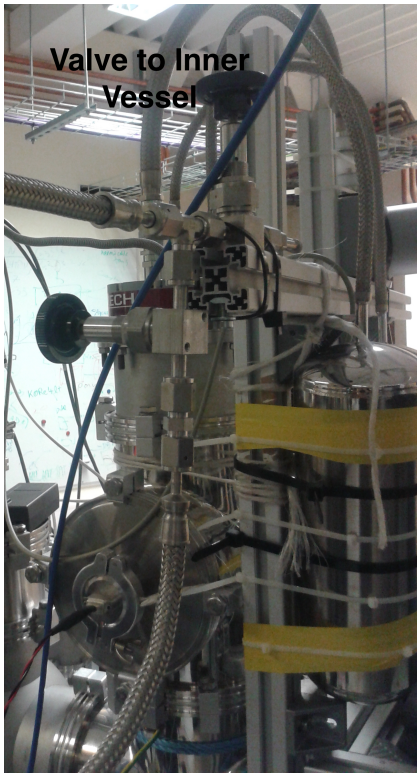

Figure 4.18: Image of the valve (attached to support structure) which is used to either put vacuum on the inner vessel or vacuum on the inner vessel.

For each argon fill, the detector was filled first with warm, room temperature argon gas until the internal pressure reached 1 bar. This gas was then vacuum purged until the internal pressure was 10^{-3} bar. This process was repeated 6 times for each fill. We called this procedure a warm flush. The purpose of this was to scrub the detector and reduce impurities. After the warm flush, the cryocooler was turned on to begin the cool down.

4.4.4 Fridge and Cryogenics

A Cryomech fridge and cold head was used to chill the argon. The inner vessel was attached to the cold head using thermally conductive copper braid. A schematic of the cold head can be found in image 4.19. This copper braid was on the far end the detector

away from the PMT. It was placed at approximately 130 cm behind the window. This braid suspended the inner vessel in the detector to further minimize thermal contact with the stainless steel outer vessel. The heat from the cold head was transferred to the inner vessel via the copper braid. The temperature of the cold head could be controlled via the Lakeview temperature controller and the slow control system.

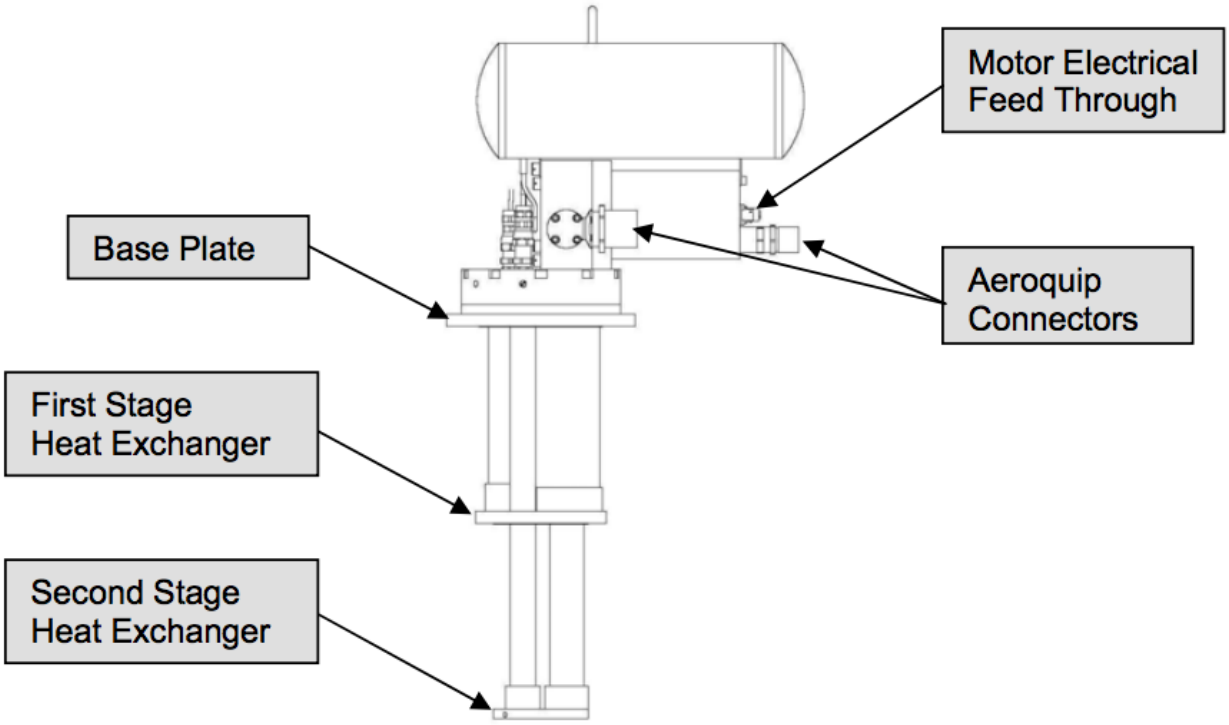

Figure 4.19: Schematic image of the cold head [156].

The argon in the system was liquified using the following steps. Following the warm flush, the inner vessel was filled with 1 bar of room temperature argon (277 K). The heater temperature was then set at 150 K. The system was then allowed to thermally stabilize. Following this, the temperature on the heater was dropped in 10 degree increments until the cold head end of the inner vessel was a temperature of 120K. At this point more

argon was added to the system until the inner vessel was at 1 bar of pressure. The heater was then gradually brought down in temperature. More argon was added throughout the process to keep the pressure at around 1 bar. Once the temperature sensors on both ends of the inner vessel read the same temperature, this signified that the argon had liquified. A cold flush of the system was then preformed 7 times to remove an impurities in the cool down. The argon was set to flow into the detector. The pressure on the argon flow line was kept at 1 atm.

4.4.5 PMT's

Argon PMT

The PMT installed in the OV is a Hammatsu R6901 Mod [157]. The R6901 window is made of borosilicate glass and has a diameter of 7.6 cm. The photocathode is made of bialkli and is 6.5 cm in diameter. The length of the tube is 13.7 cm. The R6901 is a 12 stage PMT. The gain as listed by the manufacturer is 5×10^6. The wavelength range of a R6901 is 300 nm to 650 nm with a peak wavelength of 420 nm, making it ideal to detect light coming from the TPB.

The PMT was operated at a voltage of 1500 V for argon fill 1 and 2 and 1600 V for argon fill 3. (The reason for the increased voltage in the third run was due to a power supply being swapped out and the replacement needed to be run at 1600V.)

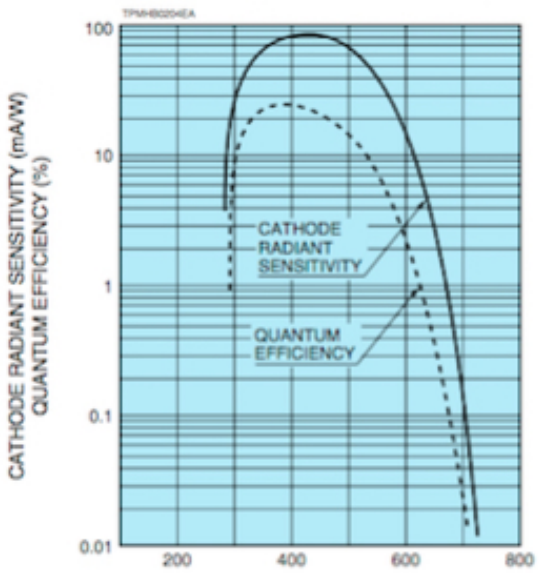

Figure 4.20: Typical spectral response of R6901 PMT. The x-axis is wavelength in nm. The solid black line on on the y-axis is cathode radiant sensitivity in mAW. The dashed black line on the y-axis is quantum efficiency percentage.

Sodium PMT

In two of the argon runs, a double PMT set up was used. The second PMT was used in conjunction with a sodium source to tag events from the source as a means of background reduction. (The DAQ set up for this experimental set up can be found in Figure 4.28). This PMT faced the sodium source on top of a collimator. The PMT used as the tagging PMT was an electron tube 9954B series [158]. The 9954B window is made of borosilicate glass and as a diameter of 5.6 cm. The photocathode is made of enhanced biakli. The 9954B has 12 BeCu dynodes. The quantum of efficiency at the peak wavelength is 28%. The gain was not listed or measured.

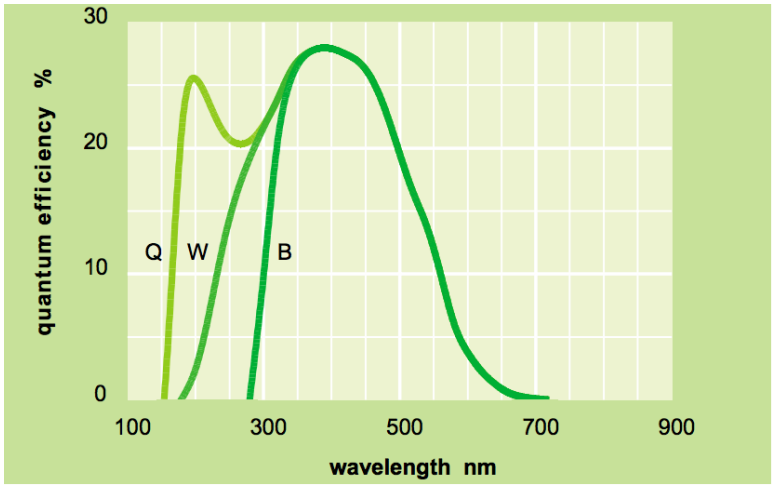

Figure 4.21: Image from citeElec:2007A. The x axis is wavelength in nm and the y axis is the quantum efficiency. This shows the quantum efficiency of the 9954B series. The dark green "B" is the quantum efficiency for the PMT used in the experiment.

A cube of plastic scintillator was coupled to the sodium PMT window using optical grease. This was wrapped with mylar to reflect scintillation light back into the PMT. This was then wrapped in the 3 layers of black tape which extended down the base.

Tag PMT Dark Box

The tag PMT (Figure 4.22) was installed in a mobile dark box (Figure 4.23) to prevent contamination from outside light as shown in Figure 4.24. The box was constructed out of corrugated paper and enforced with aluminum support. The box was covered in black paper and black duct tape. Each corner of the box had black paper baffles installed to prevent any light from directly entering. The lead collimator cap was installed inside the box and hole was cut in the bottom so the box could be placed over the radiation source. Light was prevented from entering this hole by the black foam on the top of the collimators. The tag PMT was inserted into the lead cap. The cords ran out the back

through two holes. These were covered on each side by black rubber to prevent any direct light from entering. The entire box was sealed once everything was installed. The box was place on adjustable stand to keep this box at the collimator level so that it could envelop the source and allow the tagging PMT to detect events from the sodium source (Figure 4.24).

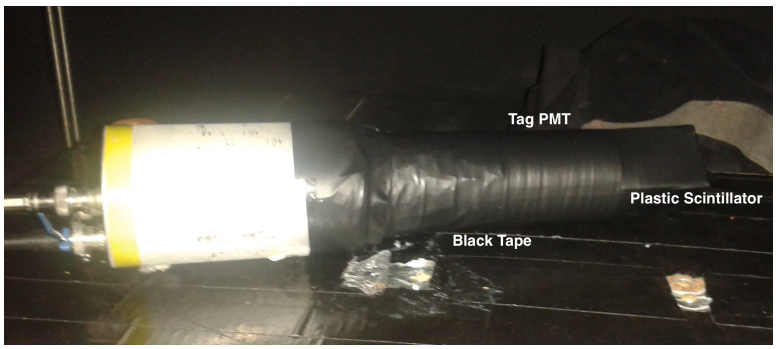

Figure 4.22: An image of the Sodium PMT. The plastic scintillator is coupled to the PMT window and this has all be wrapped in black tape.

Figure 4.23: An image of the sodium PMT dark box. This was taken before the PMT was installed. Once the PMT was installed, the box was sealed to prevent light leaks.

Figure 4.24: An image of the inside of the tag PMT dark box. This includes the source holder for the sodium source.

4.5 Data Acquisition System (DAQ)

In the Rayleigh scattering experiment, two different DAQ configurations were used. The first was the single PMT, or untagged set up. The second was the double PMT or tagged set up.

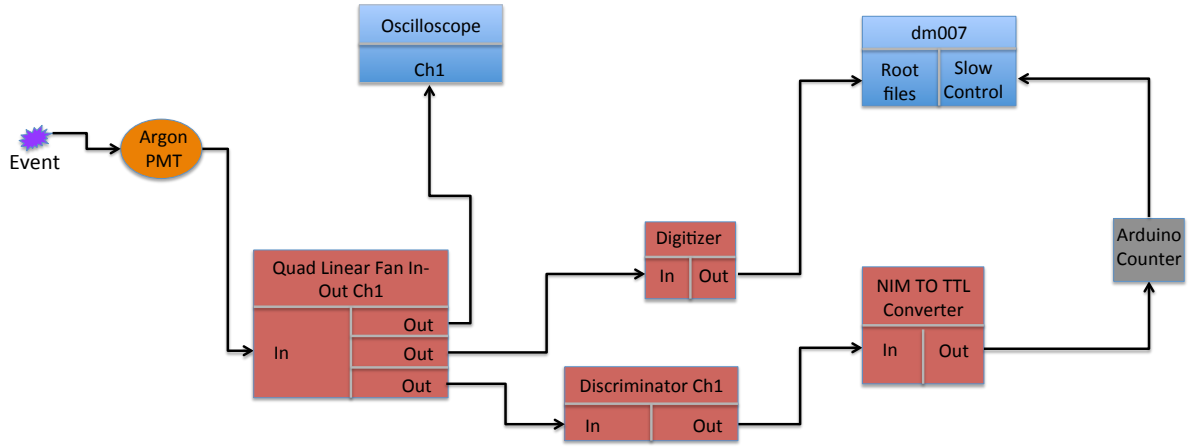

Figure 4.25: DAQ box diagram for the single PMT data set up. A signal is detected by the PMT from the argon. The diagram flows from left to right. The orange corresponds to PMT's. The red boxes are NIM logic units. The grey is the counter. The blue corresponds to computers and oscilloscopes. Dm007 is the name of the computer which stored data.

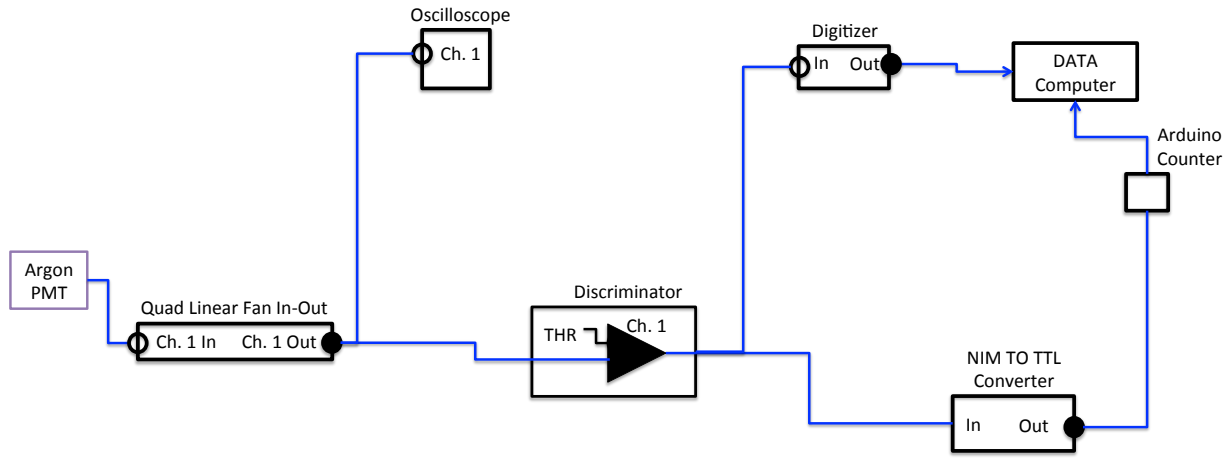

Figure 4.26: DAQ logic diagram for the single PMT data set up. The discriminator sets the voltage threshold for an event to be counted.

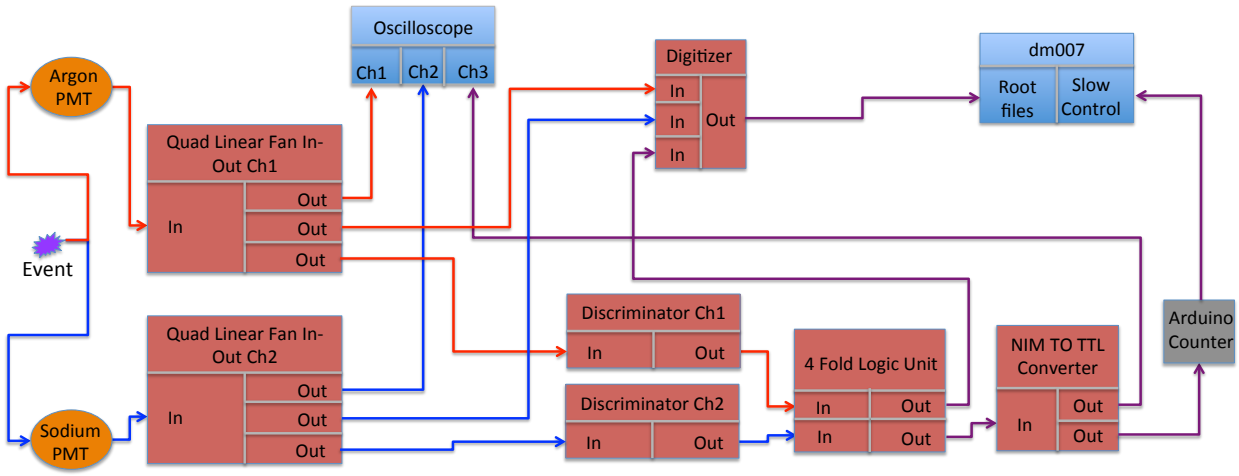

Figure 4.27: DAQ box diagram for the doublePMT data set up. The blue path is the data flow of the Argon PMT. The red path is the data flow of the Sodium PMT. The purple bath is the combined logic signal. The diagram flows from left to right. The orange corresponds to PMT's. The red boxes are NIM logic units. The grey is the counter. The blue corresponds to computers and oscilloscopes.

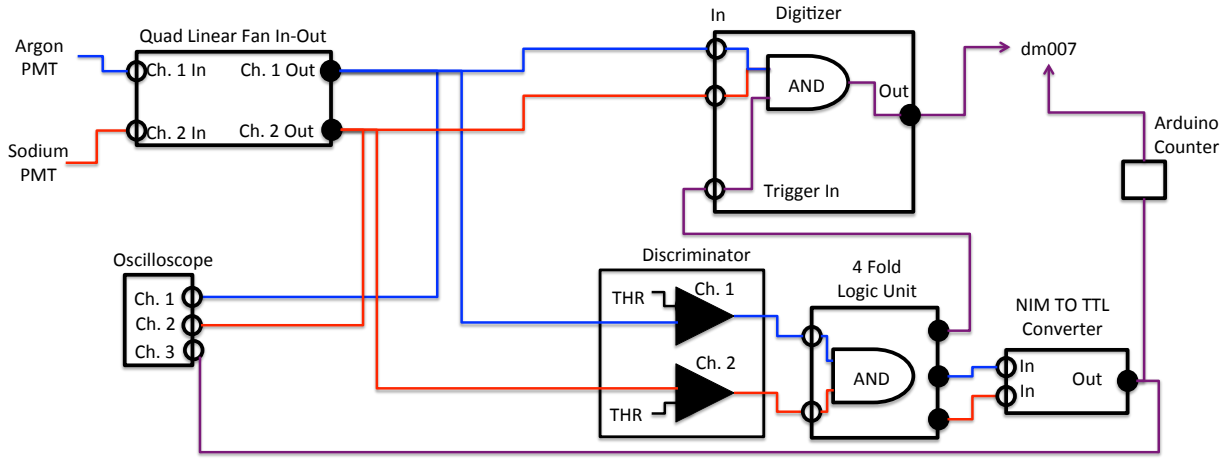

Figure 4.28: This figures shows the DAQ configuration for the double PMT set up. The blue path is the argon pmt. The red path is the sodium pmt.The discriminator sets the voltage threshold for an event to be counted. The tagged works using AND logic in the 4 Fold Logic Unit.

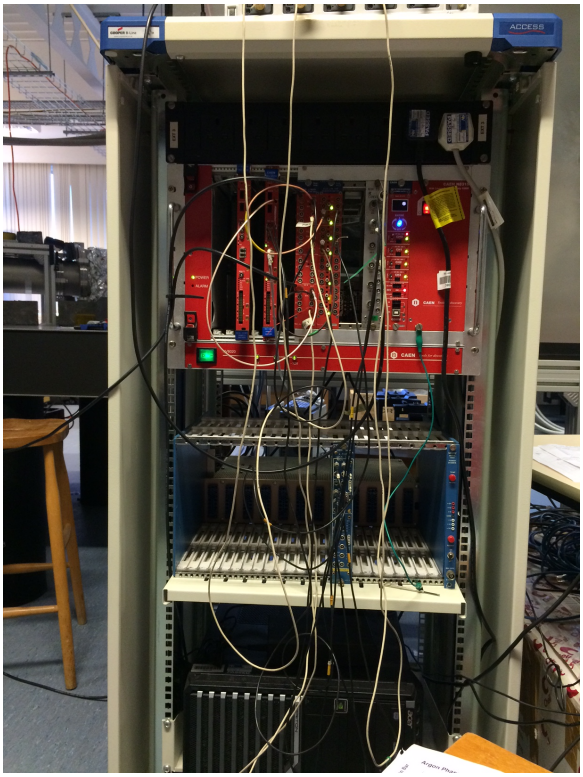

Figure 4.29: The CAEN cart used for data acquisition. At the top of the cart is the oscilloscope (not pictured). The top row of units from left to right: CAEN Mod V1720 digitizer (unused), CAEN Mod V1720 digitizer, CAEN Mod N401 Quad Linear FAN IN-OUT, CAEN Mod N417 8 Channel Discriminator, NIM to TTL Converter, and CAEN 4 Ch High Voltage supply. The second row from left to right: 4-Fold Logic Unit. The PC where data is stored for analysis (which is referred to in this thesis as dm007).

4.5.1 CAEN Modules

Fan In Fan Out The signal from the argon PMT goes in channel 1 in the CAEN Mod N401 Quad Linear Fan In Out [159]. The Quad Linear Fan In Out inputs are bipolar, DC coupled, with a 50 Ω impedance. Each output send out the combined signal of all the outputs. The delay between the input and out is 4 ns± 1ns. In our set-up, there was one input and two outputs.

In, the tagged condition, the argon PMT went to channel 1 and the sodium PMT went to channel 4. Each channel had one input and 3 outputs.

Discriminator In the tagged and untagged configurations, one of the signal output from the Fan In Fan Out argon PMT went to Channel 1 of the discriminator. A CAEN M417 8 Channel Low Threshold discriminator [160] was used. This sets the threshold voltage to accept a signal. For the argon PMT in argon fills, the threshold was set to -8 mV in argon fill 1, -12 mV for argon fill 2, and -8 mV for the argon fill 3.

In the tagged configuration, the signal output from the Fan In Fan Out from the Sodium PMT goes to Channel 2 of the discriminator. The threshold voltage was set to -150 mV, which corresponds to the voltage response of the 511 keV peak from the Sodium source. See Figure 4.30.

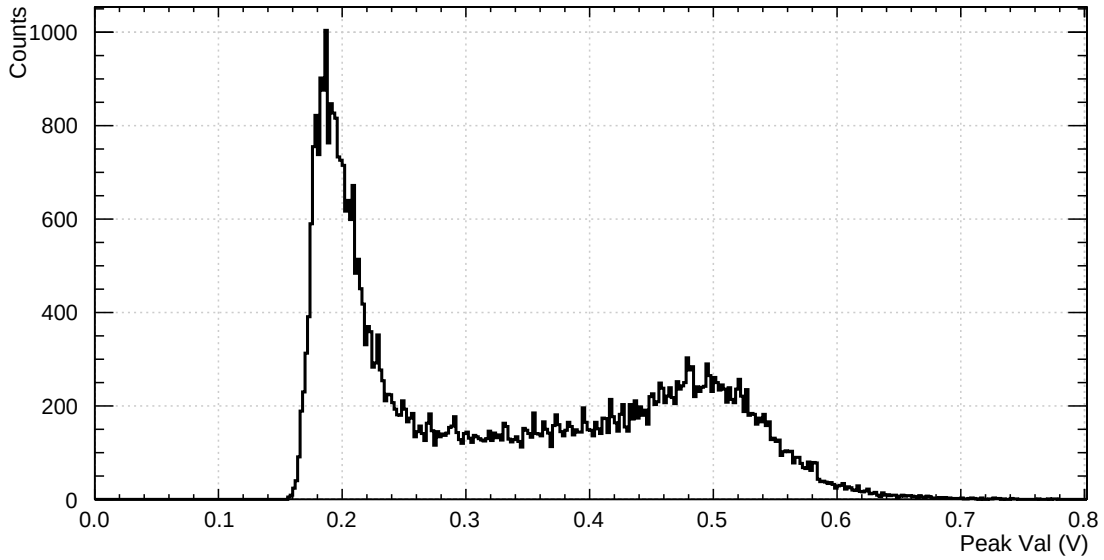

Figure 4.30: The spectrum of the ^{22}Na source using the threshold of -150mV. The x-axis is voltage on the sodium PMT and the y-axis is the number of counts. The 511 keV peak and 1274 keV peaks are clearly visible.

Digitizer The second output from the Fan In Fan Out from the argon PMT signal went to the V1720 CAEN digitizer [161]. This converted the voltage signal in ADC counts [162]. In the single PMT set-up, this used an external trigger set by the discriminator voltage. In the double PMT set up, the digitizer utilizes an external trigger set by the 4-Fold Logic Unit.

The second output from the Fan In Fan Out from the sodium PMT signal went to the V1720 CAEN digitizer. This converted the voltage signal in ADC counts.

4 Fold Logic Unit In the double PMT set up, the outputs from both the argon and sodium went from the discriminator to the LeCroy 4 Fold Logic Unit [163]. This is used to establish coincidence between the two pulses. The coincidence width was set to 150 ns. The coincidence signal was monitored by the oscilloscope. This signal was also used to trigger the digitizer to record the wave pulses from the argon and sodium PMT's.

NIM to TTL Converter In the single PMT set up, the NIM to TTL discriminator receives a signal from the discriminator. This signal is then sent to the Arduino counter which counts the number of PMT pulses. This is used to calculate a basic rate, using the slow control.

In the two PMT set up, the signal from the 4 Fold Logic Unit was then sent to the NIM to TTL Converter [164]. This signal is sent to the ardiuno counter which counts the number of coincidence pulses. This is used to calculate a basic rate using the slow control.

4.5.2 DAQ Code

To record data during the experiment a previously developed DAQ code was implemented. This code was externally triggered from the digitizer signal. In the argon PMT, this

trigger was set by the discriminator threshold. In the double PMT set up, this was set using the discriminator threshold voltages and the coincidence unit. The number of events (waveforms) that would be acquired was preset by the user. This code could modified to record data from 1 or two PMT's. Each waveform was 16,000 ns in length.

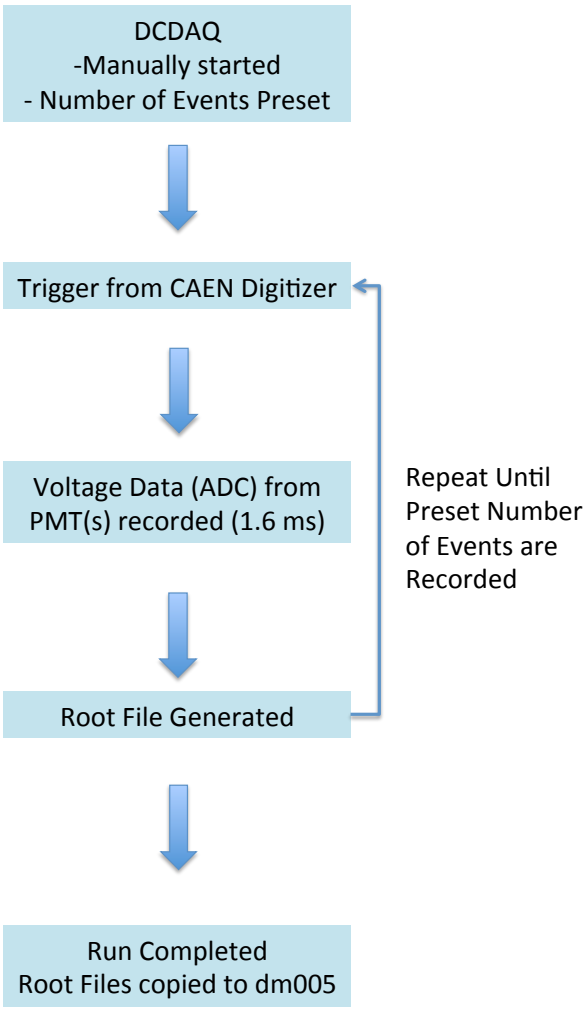

Figure 4.31: Flow chart of data acquisition during experimental runs.

4.6 Discussion

This chapter described the geometry model used in simulations and the detector set up. This included the DAQ system and the system monitoring. The following chapter details the three data acquisition runs that were performed.

Chapter 5

A Description of the Stability During Data Acquisition

Science's domain is the natural. If you want to understand the natural world and be sure you're not misleading yourself, science is the way to do it.

Dr. Francis Collins

5.1 Introduction

Data acquisition transpired over three different experimental runs. Each run took place at a different period in time and with a new supply of argon. The first run (Run 1) was used to make the measurement. The second two runs (Run 2 and Run 3) were to understand the contribution of reflection. This chapter includes a detailed description of each data run. This includes changes in the detector configuration and the motivations behind the detector alterations. The stability of the temperature, pressure, triplet lifetime, and PMT voltage is presented. As shown in Chapter 3, the Rayleigh scattering length is a sensitive function of temperature and pressure; therefore, ensuring detector stability is the first step in the analysis process. This section describes the criteria applied to select stable data.

These criteria are applied to low-level variables measured directly by detector pressure and temperature sensors, which are acquired in the slow-control data stream. The variables examined to determine detector stability are: temperature of the front and back of the internal detector and pressure.

As discussed in Chapter 2, the triplet lifetime is an indicative of the purity of the argon. The triplet lifetime was monitored over the length of the run using background data taken in the single PMT set up.

5.2 Parameters for Begining Data Acquisition After an Argon Fill

In each of the detector configurations, the data acquisition process began after the cooling and filling process was complete. At this point, the valves for the gas system were sealed. No additional argon was introduced to the system during the experimental runs. Table 5.1 summarizes the parameters and data acquired in each argon fill.

Argon Run	Front Aperture Size	Number of Untagged Data Positions	Number of Tagged Data Positions
1	4 cm	36	0
2	2 cm	4	14
3	0.5 cm	0	5

Table 5.1: Details of each of the argon runs. The number of untagged positions refers to the number of untagged data points taken with a ^{22}Na source and the number of tagged data points taken with ^{22}Na.

5.3 Acquiring Stability Variables

The stability of each run was determined by examining the temperature and pressure variations over course of data acquisition. This was extracted from the first pass analysis output file. The first pass analysis code was used to compile the time and the conditions in which the data was taken. The start and ending time was written into each data file. The start time recorded was the begining of data acquisition and the ending time was recorded was the time the file was written. This information was then used to extract the temperature and pressure information. The information from the temperature and pressure sensors for the length of time was extracted from the slow control. This includes the average temperature and pressure and the sigma on the average.

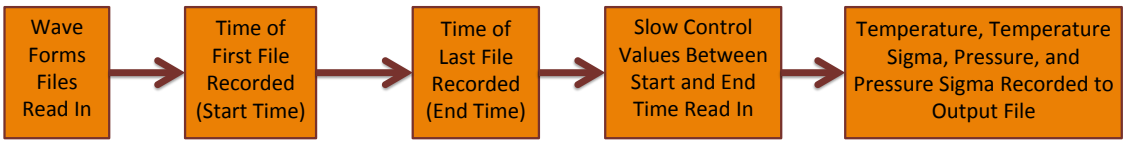

Figure 5.1: A flow chart showing the process of storing detector sensor data.

The stability of the PMT for each run was also recorded. The baseline voltage, or pedestal, of the PMT for each data run was taken by average the voltage of the first 1000 ns of each waveform. This is about 1500 ns before the average trigger time. This values is used to examine the stability of the PMT for each data run.

The triplet lifetime was measured by averaging the waveforms in a data file run. The pulse was shifted such that the peak was at 0 ns. The pulse was fit from 1000 ns to 5000 ns, the time of the waveform primarily impacted by the triplet lifetime. This fit was done

using

$$V(t) = Ae^{(-t/\tau_3)} \tag{5.1}$$

where V is the voltage reading on the PMT, A is a constant, t is the time in the waveform, and τ_3 is the triplet lifetime. An example is seen in Figure 5.2.

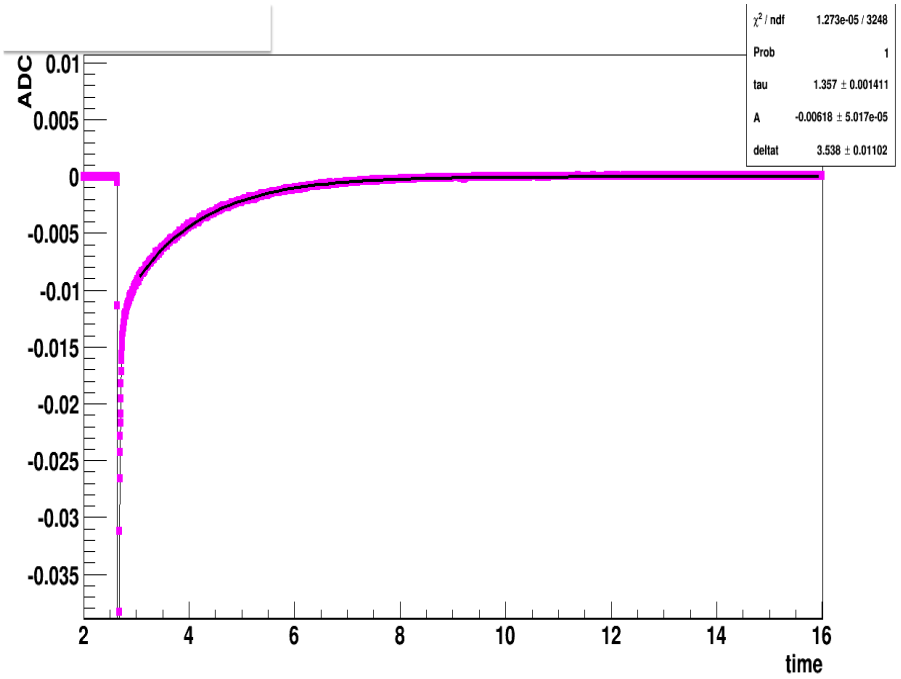

Figure 5.2: An example of fitting average waveforms for the triplet time constant. The x axis is time in ns and the y axis is in ACD. This has been fit with equation 5.1.

5.4 Radioactive Sources Used in the Data Acquisition

Calibration data was taken in the first argon fill using ^{137}Cs. To maximize the rate, 7 sources were used together with a combined rate 547 kBq, as shown in Table 5.2.

In the case of the ^{137}Cs, the rates for the sources used are in Table 5.2. The initial rates were obtained from the records of the radiation safety officer at RHUL. The present

day activity was calculated using the half-life of ^{137}Cs, 30.17 years [**?**] and equation

$$A = A_0 e^{-\lambda T}, \tag{5.2}$$

where A is the present activity, A_0 is the initial activity, λ is the half-life, and T is time.

Source Number	Purchase Date	Initial Activity	Activity on 04/2015
1	20/01/1984	37 kBq	18 kBq
2	20/01/1984	37 kBq	18 kBq
3	20/01/1984	37 kBq	18 kBq
4	20/01/1984	37 kBq	18 kBq
5	01/05/1975	370 kBq	147 kBq
6	20/07/1984	370 kBq	182 kBq
7	01/02/1974	377 kBq	146 kBq
Total			**547.55**kBq

Table 5.2: ^{137}Cs sources, purchase data, initial activity, and activity at the time of experiment. The purchase date and initial activity were obtained from the RHUL radiation safety officer the activity at the time of use was calculated using Equation 5.2.

The primary source used for data acquisition was a ^{22}Na source. ^{22}Na has a half life 2.602 years. This rate difference was taken into account for each data set. The rate for each data run is shown in table 5.3.

Source	Purchase Date	Original Activity	Activity Ar 1	Activity Ar 2	Activity Ar 3
Source 1	15 July 1996	573.5 MBq	3.925 MBq	3.755 MBq	3.252 MBq

Table 5.3: This is the activity of the sodium source used int the experiment.

5.5 Argon Fill 1

The primary distinguishing attributes of the first argon fill was the 4 centimeter baffle size and the use of a single PMT. An image of the external set up of the first argon fill is shown in figure 5.3.

Figure 5.3: An image of the collimator set up for the argon fill 1. This collimators and lead shielding were moved every five runs to get data at different positions.

Data Acquisition

Cs -137 Data Acquisition The first set of data points were taken using a ^{137}Cs source. Seven ^{137}Cs sources were used to maximize the activity. The activity of the combined sources was approximately 547.55 kBq. This is detailed in table 5.2 in Chapter 4. In this set up the, source was placed on top of a 5 cm collimator with 1 centimeter diameter. The collimator was placed on a movable cart. For each data acquisition point, an additional 9 cm of lead in the form of lead bricks was placed around the collimator. Five data points were taken using the ^{137}Cs source. Each data run, 200,000 waveforms of data were taken.

Na-22 Data Acquisition The next set of data was taken using a ^{22}Na source. The activity of the source was approximately 3.9 MBq. In this set up, the source was placed on top of a 10 cm lead collimator. In each run 200,000 waveforms were collected. Data was taken at 36 different points. In addition, 20 background runs were acquired, each with 200,000 waveforms. The background runs were taken over the course of the experiment.

5.5.1 Argon Fill 1 Data Stability

In the first argon run, we encountered problems with maintaining temperature stability. Throughout the experiment, we had to lower the temperature of the cold head gradually to maintain the same temperature. Upon dismantling the detector, it was discovered that the copper braid coupling the inner vessel with the cold head had become slack. This problem was solved in subsequent runs by adding additional hardware clamps to keep the inner vessel bonded with the copper braid.

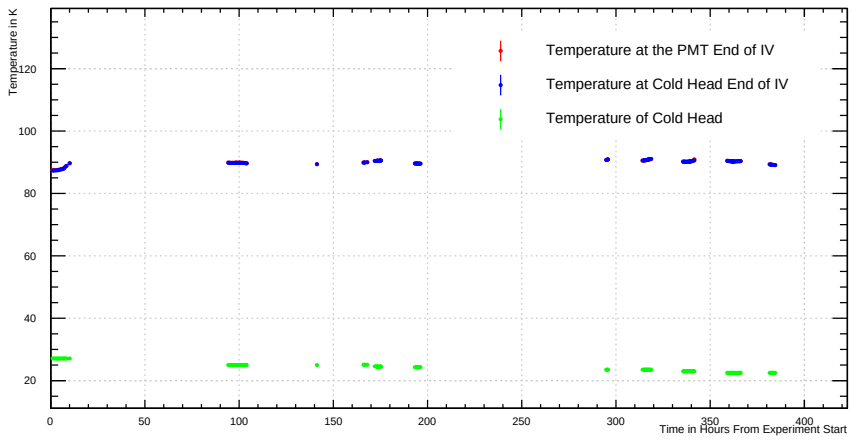

Figure 5.4: A plot of the temperature over the course of data acquisition. The x axis is in time in hours from the start of data acquisition, the y axis is temperature in Kelvin. The red points is the temperature on the outside of the inner vessel from the temperature sensor located near the PMT (underneath the blue), the blue point is the temperature on the outside of the inner vessel from the temperature sensor located on the outside of the inner vessel, and the green points is the temperature at the cold head.

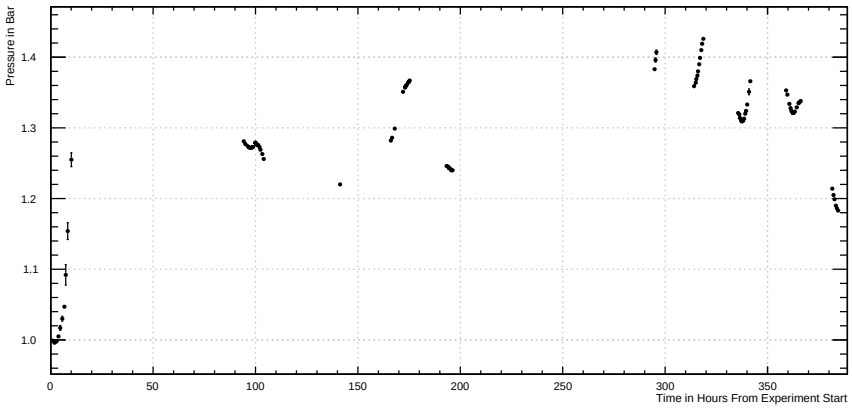

Figure 5.5: A plot of the pressure over the course of data acquisition. The x axis is time in hours from the start of data acquisition and the y axis is the pressure in bar.

The baseline voltage of the PMT remained stable throughout the data acquisition as seen in figure 5.7.

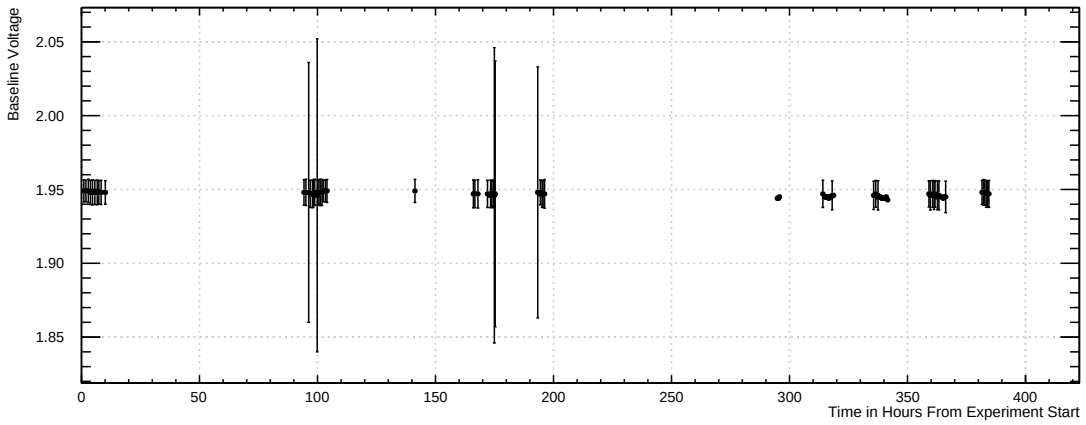

Figure 5.6: A plot of baseline voltage during data acquisition. This has been fit with first order polynomial. The slope of the line is -1.028×10^{-5} showing the stability of the baseline voltage over time.

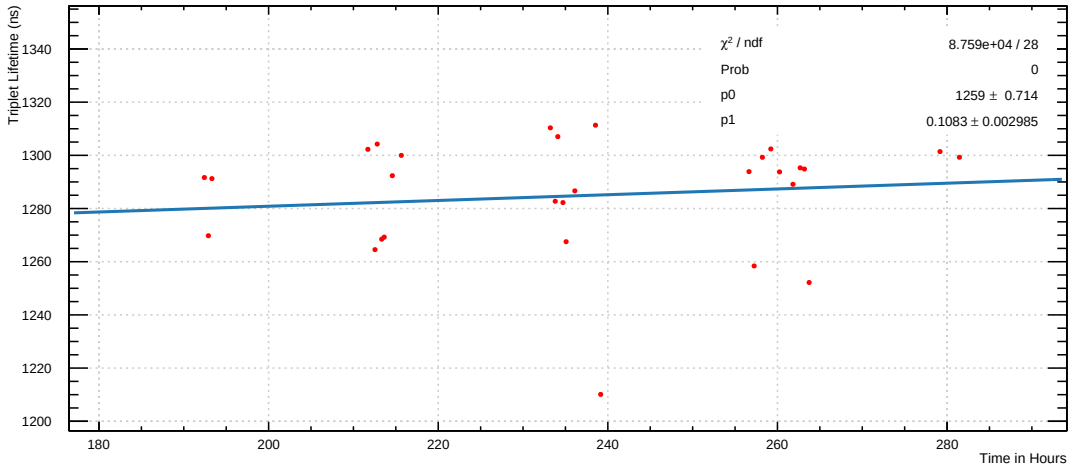

Figure 5.7: The triplet lifetime over time. The x axis is time in hours and the y axis is the triplet lifetime in ns.

5.6 Argon Fill 2

In this set up a front baffle with a 20 mm diameter was installed. The inner copper braiding that was used to couple the detector to the cold head was doubly secured for an improved thermal bond. The inner vessel was put at a downward angle so as to prevent any bubbles in the experimental region. In the second argon fill, both the single PMT set up and the tagging system were employed. An image of the second argon fill is shown in 5.8.

Figure 5.8: An image of the collimator set up for the argon fill 2. This collimators and lead shielding were moved every five runs to get data at different positions. The tag pmt is enclosed within the mobile dark box. The mobile dark box is shown on the right hand side, propped up and with a radiation safety sign attached.

Data Acquisition

This data run utilized the tag PMT set up. A 4MBq ^{22}Na source was placed on a collimator 10 cm in height with a 1 cm diameter opening. For this run data was acquired at 12 different positions. 50,000 events were recorded in each source run. Tagged background runs were taken overnight and had a variable number of events. The tagged background rate was less than 1 Hz.

5.6.1 Argon Fill 2 Data Stability

Untagged background was taken throughout the run. This was used to monitor the detector stability as well as to find the triplet lifetime constant.

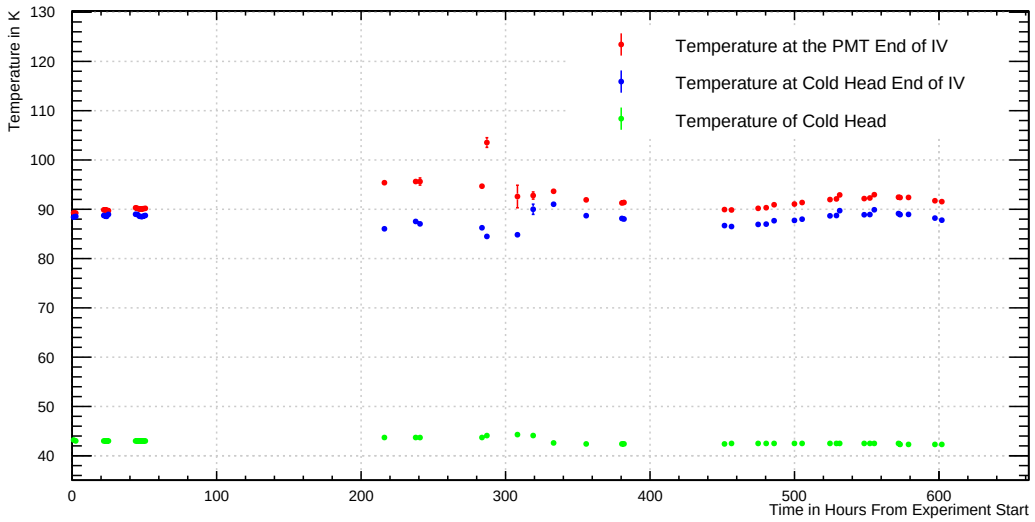

Figure 5.9: A plot of the temperature over the course of data acquisition. The x axis is in time in hours from the start of data acquisition, the y axis is temperature in Kelvin. The red points is the temperature on the outside of the inner vessel from the temperature sensor located near the PMT, the blue point is the temperature on the outside of the inner vessel from the temperature sensor located on the outside of the inner vessel, and the green points is the temperature at the cold head.

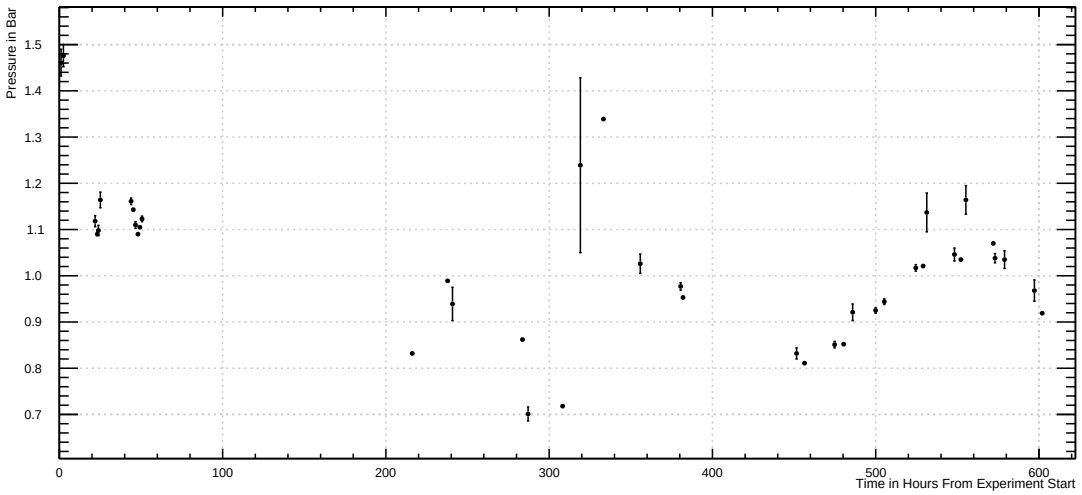

Figure 5.10: A plot of the pressure over the course of data acquisition. The x axis is time in hours from the start of data axquistion and the y axis is the pressure in bar.

The baseline voltage of the PMT remained stable throughout the data acquisition as seen in figure 5.11.

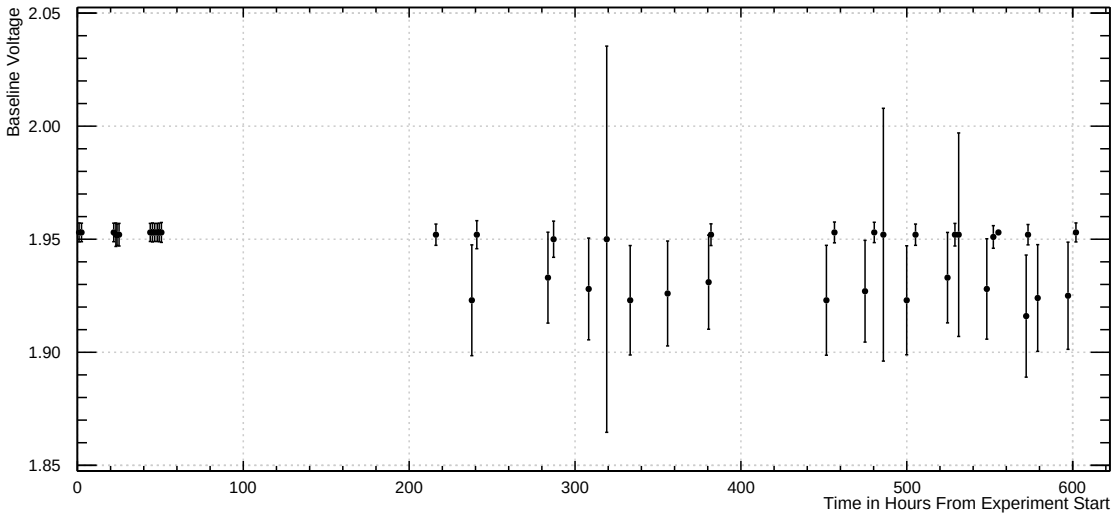

Figure 5.11: A plot of baseline voltage during data acquisition. This has been fit with first order polynomial. The slope of the line is -1.028×10^{-5} showing the stability of the baseline voltage over time.

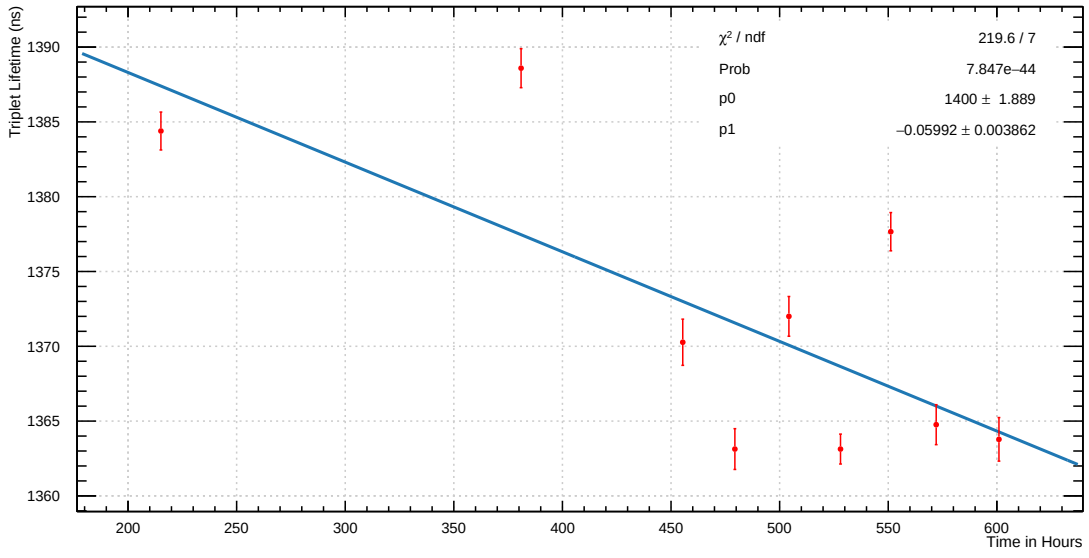

Figure 5.12: The triplet lifetime over time. The x axis is time in hours and the y axis is the triplet lifetime in ns.

5.7 Argon Fill 3

In the third argon fill, a 0.5 centimeter front baffle was installed. This done to restrict the impact of reflection from the sides of the detectors. This set up also utilized the ^{22}Na double PMT tag system. As with Argon Fill 2, a 10 centimeter in length collimator was used with 1 centimeter in diameter opening. Data was taken at 5 positions along the detector. The collimators and surrounding lead blocks were left in one place during data acquisition. 600,000 raw waveforms were taken at each position.

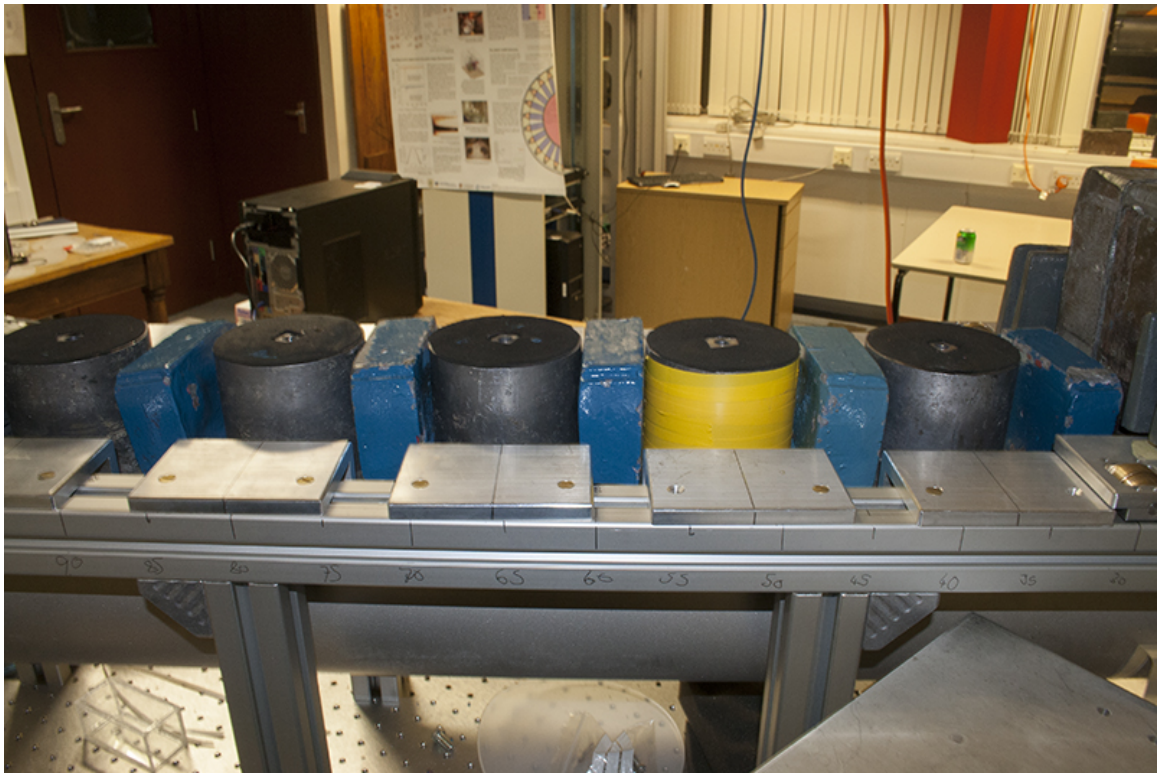

Figure 5.13: A top down image of the collimators set up in the argon fill 3 data acquisition.

5.7.1 Argon Fill 3 Data stability

The temperature and pressure conditions in the third argon fill were more stable. However, the power supply used during the data acquisition cased a drift in the baseline voltage reading on the PMT.

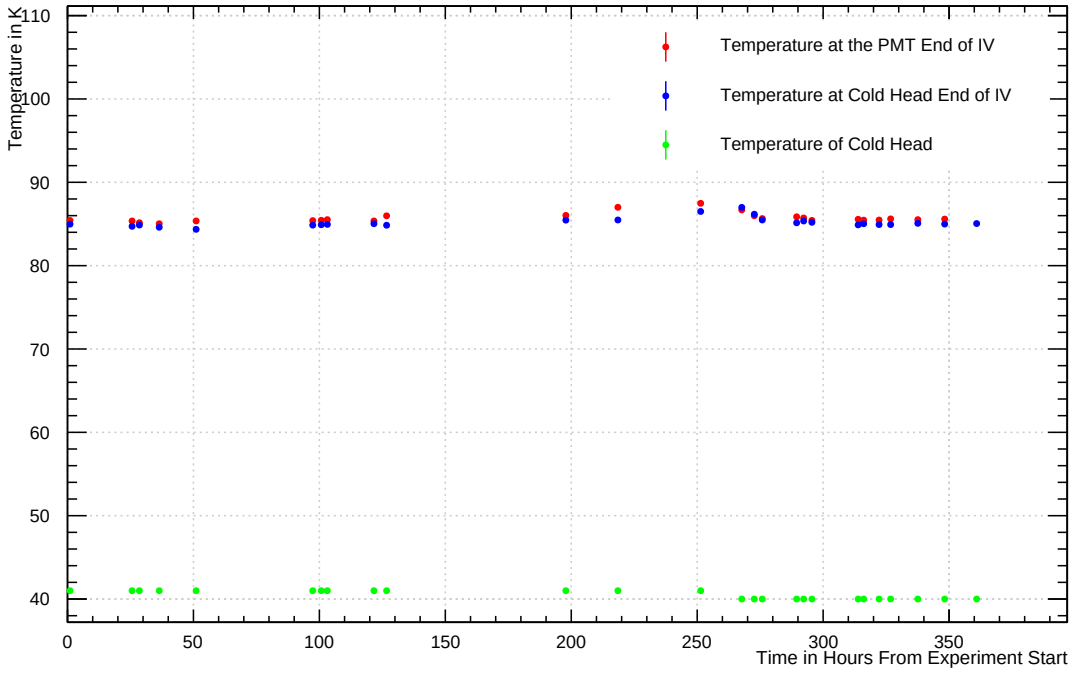

Figure 5.14: A plot of the temperature over the course of data acquisition. The x axis is in time in hours from the start of data acquisition, the y axis is temperature in Kelvin. The red points is the temperature on the outside of the inner vessel from the temperature sensor located near the PMT, the blue point is the temperature on the outside of the inner vessel from the temperature sensor located on the outside of the inner vessel, and the green points is the temperature at the cold head.

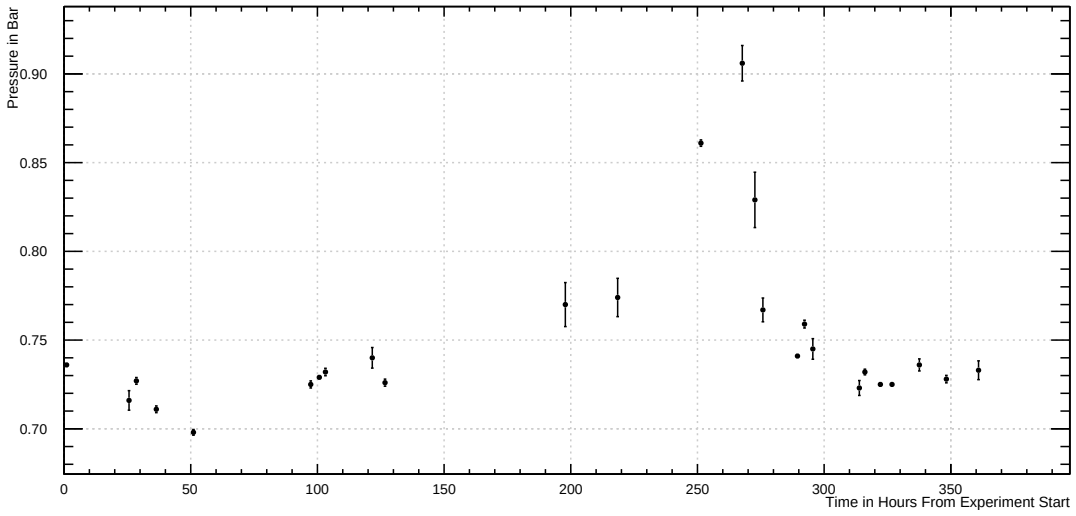

Figure 5.15: A plot of the pressure over the course of data acquisition. The x axis is time in hours from the start of data axquistion and the y axis is the pressure in bar.

The third argon fill used a different power supply. The baseline voltage was less stable as a result as shown in Figure 5.16.

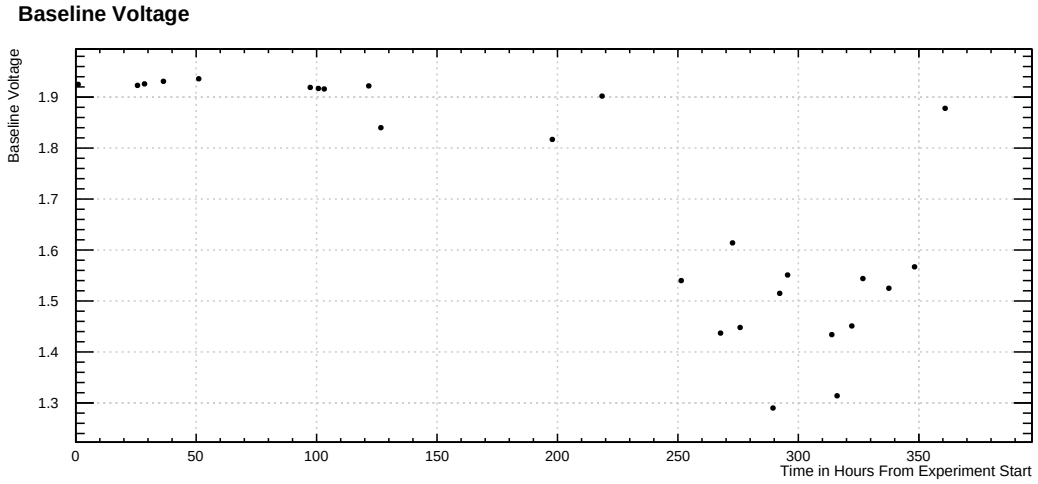

Figure 5.16: A plot of baseline voltage during data acquisition. This has been fit with first order polynomial. The slope of the line is -1.028$\times 10^{-5}$ showing the stability of the baseline voltage over time.

Data in the third argon fill had very low statistics due to the small front aperture. As a result only one measurement for the triplet lifetime was obtained The triplet lifetime of the third argon fill is 1458 $\pm$ 5 ns.

5.8 Discussion

The conditions in the first argon run, was the most stable, despite some temperature and pressure fluctuations. In the first argon run, the detector was cooled over six weeks and allowed to stabilized cold and full for three weeks before data acquisition.

The conditions in the second run were less stable in terms of state. There are some clear data points that were taken in mixed state conditions. This can be determined by examining the plot of pressure and temperature. In this experimental run, external variables necessitated that the detector be cooled quickly, (it was cooled in a week) and filled quickly, (it was filled in 1.5 weeks.) Data acquisition began immediately after the

fill.

The conditions in the third argon run were less stable. The baseline voltage drift on the PMT is likely attributed to using a different power supply, as the was the only change between the second and third fills. The temperature conditions were more stable.

These conditions are used in the follow chapter to determine the errors on the measurements.

Chapter 6

Scattering Length Analysis and Results

One must work; one must work. I have done what I could. - Louis Pasteur

6.1 Introduction

This chapter details the process of analysis, which includes data reduction, calibration, signal event selection criteria, background subtraction, and the fit to measure the Rayleigh scattering length.

6.2 First Pass Analysis

Once the data was collected, the raw waveforms were processed with the first pass analysis code. The first pass analysis code concatenates data acquired over many sub-runs, applies the digitizer and PMT calibration constants, finds PMT pulses, and calculates pulse characteristic variables. Two variations on the first pass analysis were used: one variation took data on a single PMT (Figure 6.1), and the second compiled data from two PMTs (Figure 6.2). The single PMT setup was used for the entirety of the first argon fill and for all untagged background data runs in all argon fills. The tagged PMT set up was used

in the second and third argon fill for source and background runs.

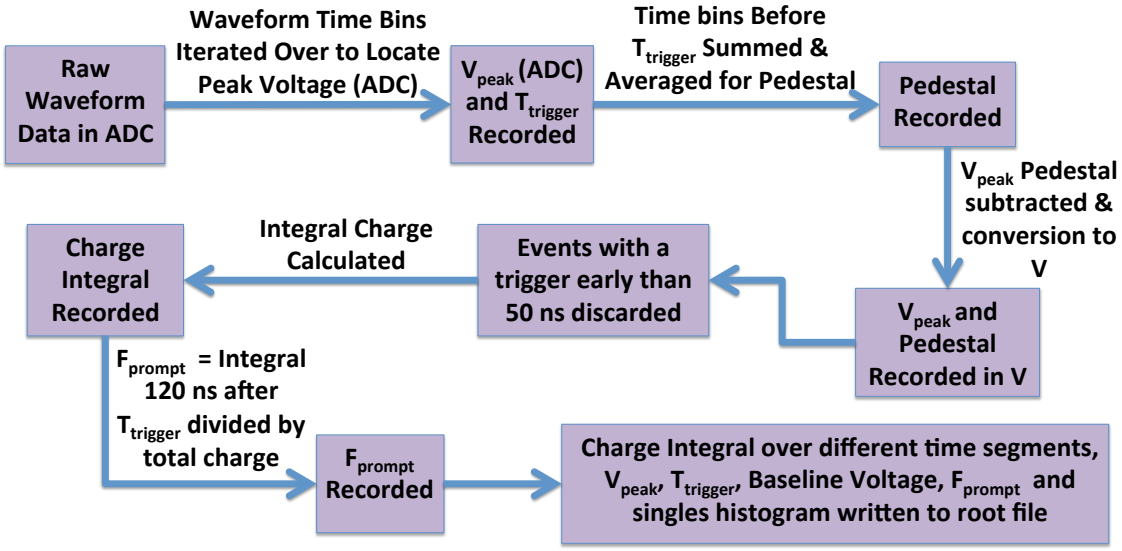

Figure 6.1: A flow chart depicting the data flow for the first pass analysis.

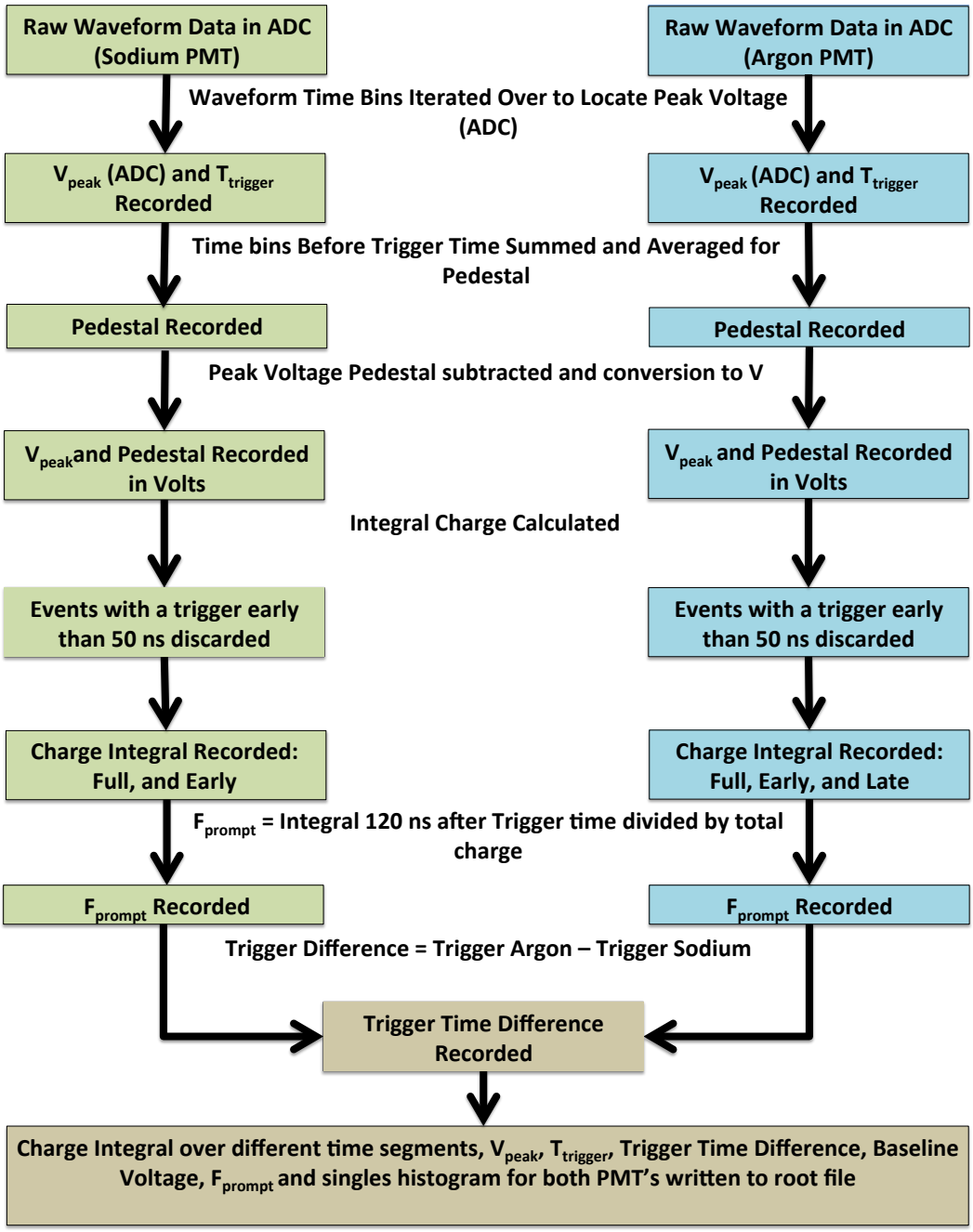

Figure 6.2: A flow chart depicting the data flow for the first pass analysis for the double PMT set up.

In each data set, the waveforms were recorded into 100 root files with an equal number

waveforms. The number of waveforms in each file depended on run type. The first pass analysis read in each file, extracted pulses and calculate variables to characterize each event waveform. This information was then written into a single root file to describe the full data run. The waveform characterization process is described in detail below.

6.2.1 Raw Data Conversion to Physical Units

Voltage data in the experiment was recorded in ADC counts. The conversion from ADC into volts is

$$V = \left(\text{ADC} \times \frac{2.0}{4096.0}\right)[-1], \tag{6.1}$$

where V is the value in volts. The result is multiplied by -1 to invert the negative-going PMT signal to positive. In the first pass analysis, this conversion was done prior to writing the information do the output file.

Each waveform was divided into 4000 time bins. Each time bin was 4 ns in size, limiting the timing resolution to 4 ns intervals. The conversion is

$$T[ns] = B_i(4), \tag{6.2}$$

where T is the time, B_i is the bin number.

6.2.2 Calculation of Waveform Properties Used for Pulse Finding

Pulses were identified based on deviation form the baseline voltage. The method for determining the baseline voltage is described below.

Baseline Voltage The pedestal or baseline voltage was calculated using the first 250 time bins (1000 ns) in the waveform and calculated the average voltage and the sigma on the average voltage. This value was stored and used to extract events that occurred above the baseline.

The baseline and baseline sigma was converted from ADC to voltage using Equation 6.1. These values were then written into the output file for each waveform.

Peak Voltage The peak voltage (V_{peak}) was found by iterating over the time bins in a waveform until the highest voltage value was located. This value was then pedestal subtracted before being recorded to the output file.

Trigger Time The signal trigger time corresponds to the time bin with the V_{peak}. This was done so that events where the largest pulse was outside of the trigger window could be discarded in future analysis.

Waveforms with an event trigger time of less than 50 ns were discarded after this step. An early trigger time indicates pile up in the early window from a previous event. This cut typically eliminated fewer than 0.1% of events.

Early Time Window The early time window ran from the first time bin to 4 time bins (12 ns) before the time when the voltage crossed 15% of the peak value. The early time window ending time was written on to the output file.

6.2.3 Calculation of Variables that Characterize Pulses

Pulse Finding Pulses within a waveform are identified by the deviation from the baseline voltage. Time bins with voltage entries with a value greater than three times the

baseline voltage are identified as pulses in the waveform and used in further analysis.

Charge The charge of waveform was calculated for different time segments of the waveform, early (Figure 6.4), late (Figure 6.5), and full (Figure 6.3), see Table 6.1. The charge was taken for pulses within the specified time window with voltage higher than three sigma above the baseline voltage. The charge was calculated at different time segments in the waveform.

Name	Time Window	Reason
Full Q_{tot} (Q_{tot})	Trigger Time to End of Waveform (16000 ns)	Used to calculate the total energy for an event
Early Time Window	Start of Waveform (0 ns) to Early Time	Used to detect pile up in the early window
Late Q_{tot}	5000 ns after Trigger Time to End of Waveform (16000 ns)	Used to detect late events

Table 6.1: Time windows within a waveform for which a charge Q_{tot} was calculated.

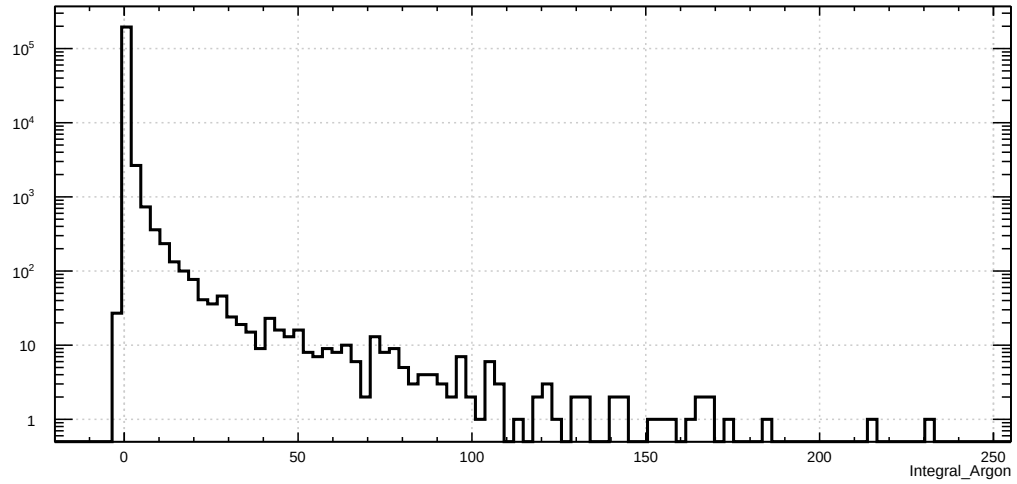

Figure 6.3: An example charge integral for the full window event. The x-axis is charge in V·ns and the y-axis is counts. This was taken using source data and is shown before any cuts were applied.

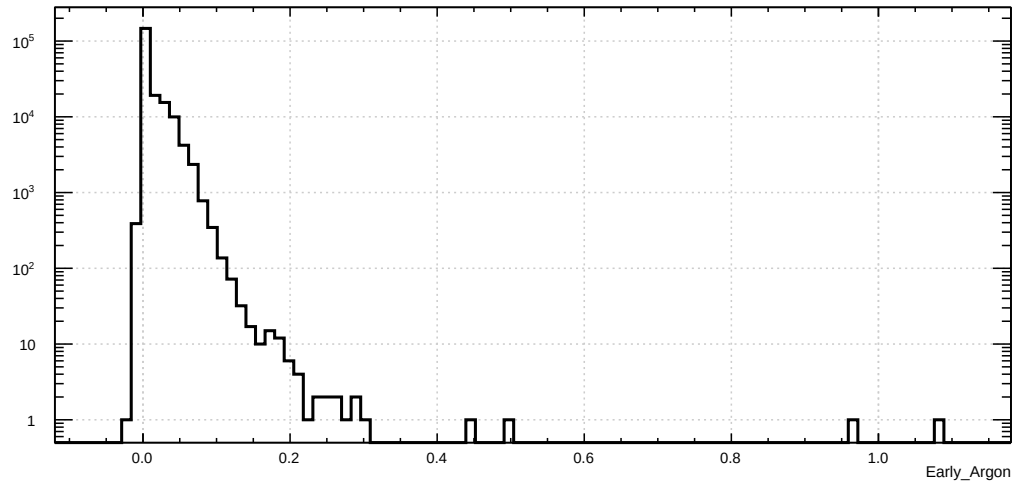

Figure 6.4: The charge integral for the early window event. The x-axis is charge in V·ns and the y-axis is counts. This was taken using source data and is shown before any cuts were applied.

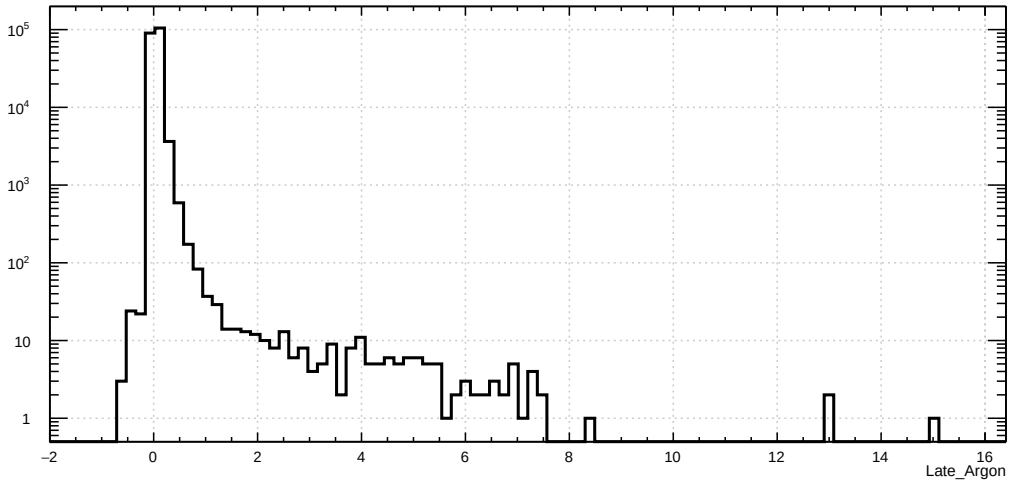

Figure 6.5: The charge integral for the late window event. The x-axis is charge in V·ns and the y-axis is counts. This was taken using source data and is shown before any cuts were applied.

6.2.4 Calculation of Variables that Characterize Events

Time Difference Between Events One consideration was the impact of pile up on interpreting data. One indication of pile up is if two events (waveforms) occurred within a short time period of each other. To quantify specifically, an event that occurred with 5 argon lifetimes of the event previous the trigger could be triggering on late light in the previous events instead of new event. To control for this, the event time of each waveform was recorded and the time difference was taken between this and subsequent event in ns. This was later used to make cuts.

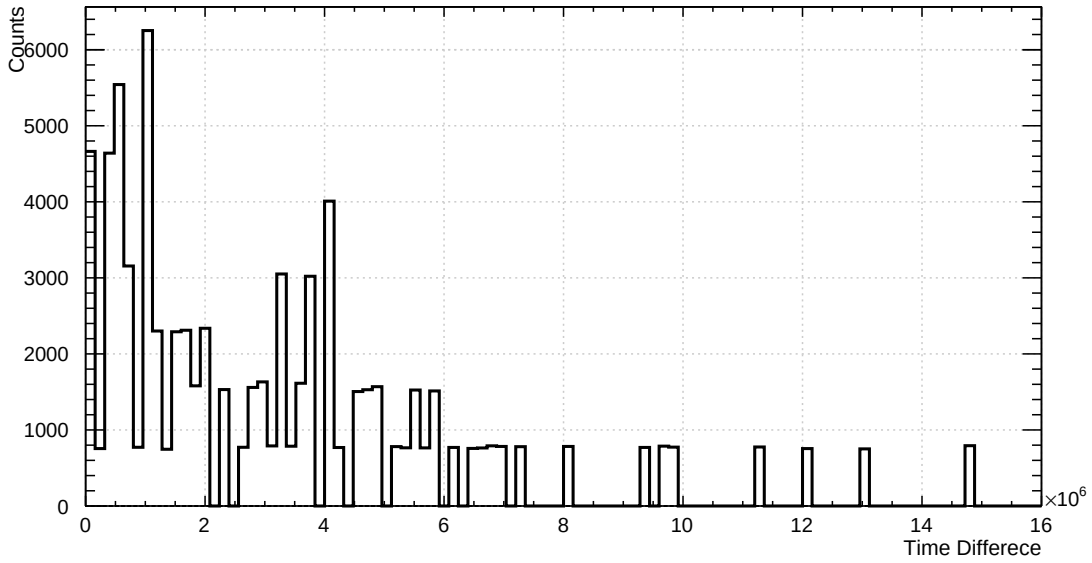

Figure 6.6: An example showing the time difference between waveform events. The x axis is the time difference in ns and the y axis is counts. This was taken from source data in the first data run.

Events Passing the Trigger Threshold in the Early Window To further understand pile up within the waveform, the events in the early and late waveforms that passed the trigger threshold were counted. The trigger threshold is defined using the CAEN data acquisition system. The number of bins with a threshold above the trigger threshold in the early window were counted. This was done by iterating through the bins starting at the begining of the waveform until a bin was found with a voltage above threshold. This triggered a counter. The next 5 time bins would be skipped and then the iteration would continue until the end of the early time window. The count of events above threshold were recorded. Several events in the early window indicates that the event was too noisy. An example of this was found in Figure 6.7. This was used both to make cuts and to identify how effective other cuts were at eliminating pile up.

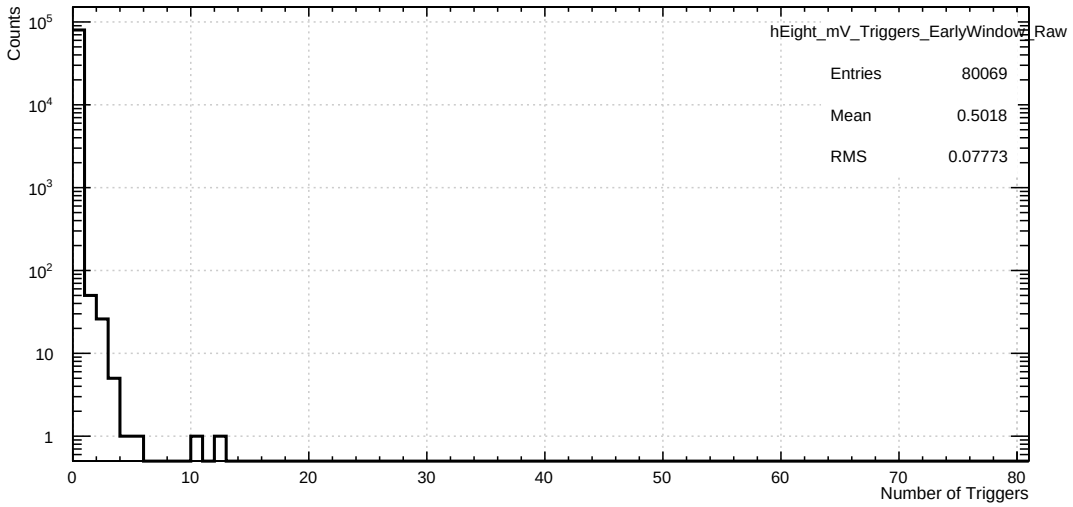

Figure 6.7: An example showing the number of events counted in the early window that passed the threshold voltage. The x axis is the number of events counted within a waveform above threshold and the y axis is how many times that number of counts was found within a run. This was taken from source data in the first data run.

Events Passing the Trigger Threshold in the Late Window To further understand pile up within the waveform, the events in the early and late waveforms that passed the trigger threshold were counted. The trigger threshold is defined using the CAEN data acquisition system. The number of bins with a threshold above the trigger threshold in the late window were counted. This was done by iterating through the bins starting at 5 lifetimes after the trigger time of the waveform until a bin was found with a voltage above threshold. This triggered a counter. The next 5 time bins would be skipped and then the iteration would continue until the end of the waveform. The count of events above threshold were recorded. Several events in the early window indicates that the event was too noisy. An example of this can be found in Figure 6.8 This was used both to make cuts and to identify how effective other cuts were at eliminating pile up.

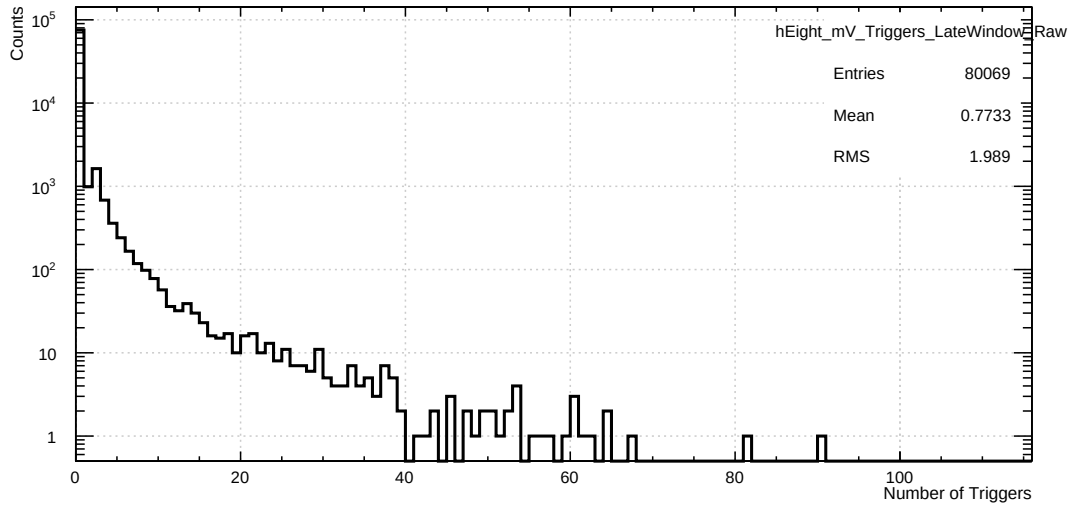

Figure 6.8: An example showing the number of events counted in the late window that passed the threshold voltage. The x axis is the number of events counted within a waveform above threshold and the y axis is how many times that number of counts was found within a run. This was taken from source data in the first data run.

Fraction of Prompt Light The fraction of prompt light (F_{prompt}) was calculated by taking the ratio of the charge that occurred within the first 120 ns after the trigger time to the total charge of the waveform:

$$F_{prompt} = \frac{C_E}{C_T}, \tag{6.3}$$

C_E is the charge in the early window (120 ns after the trigger time) and C_T is the total charge of the window (from trigger time to waveform end).

Parameters for the 2 PMT Set Up Only

Trigger Time Difference One additional parameter in this scheme is the trigger time difference between the two PMT's. This is calculated by using

$$T_{Diff} = T_{Argon} - T_{Sodium}, \tag{6.4}$$

where T_{Diff} is the trigger time difference, T_{Argon} is the trigger time for the argon PMT, and T_{Sodium} is the trigger time for the sodium PMT.

6.2.5 Calibration of PMT Pulses

Single Photoelectron Calculation

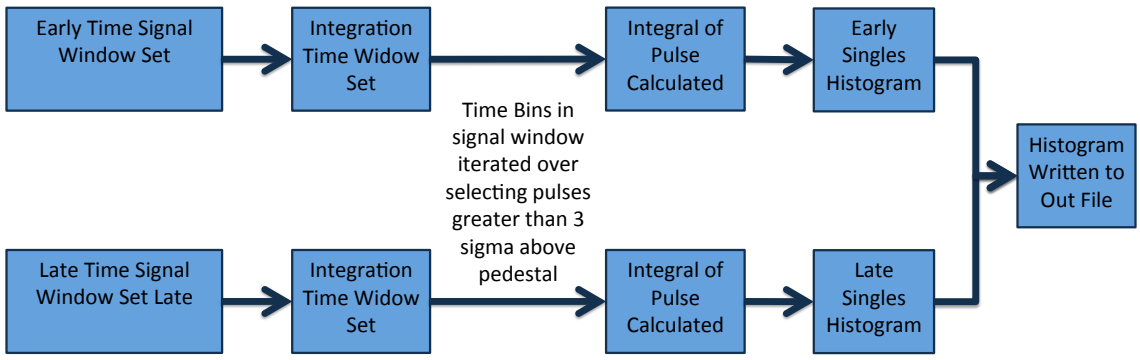

Figure 6.9: A flow chart depicting how singles were extracted from pulses in the first pass analysis. This is a subset of the processes in the first pass analysis.

In order to measure the charge of a single photoelectron, data needed to be obtained using samples where the signal is low light single events. This was done by sampling the waveforms in two places. The first pass analysis was used to extract singles pulses from the data taken to determine the single photoelectron (PE) charge, a process detailed in

Figure 6.9. The signal pulse occurs at around 2640 ns in each waveform. Data was taken in the pre-pulse region and the the post pulse region, 8000 ns after the trigger time. The post-pulse region was determined by the argon triplet lifetime by 5. An example of a waveform with a single PE pulse in the late charge window is shown in Figure 6.10 and Figure 6.11. To find singles, the code ran over the voltage isolating pulses with a charge greater than $3-\sigma$ of the baseline voltage. The Q_{tot} of these selected pulses was calculated and written out.

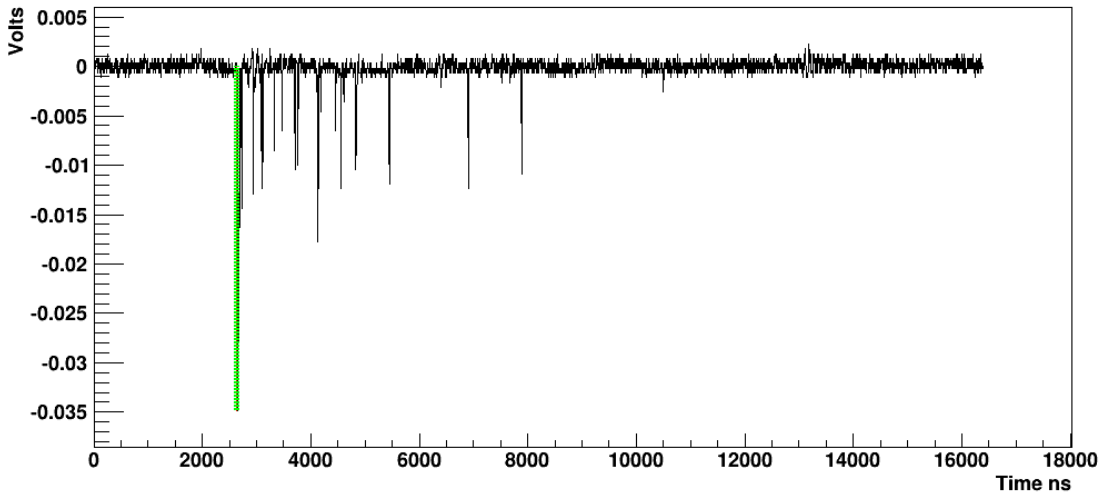

Figure 6.10: An example of waveform with a single photoelectron even in the late window. The x axis is time in microseconds and the y axis is voltage in Volts. The single event is just before the 8.0 microseconds and is 0.012 microseconds in length. The red and green vertical lines show the prompt window. A zoomed version of this single PE can be found in Figure 6.11.

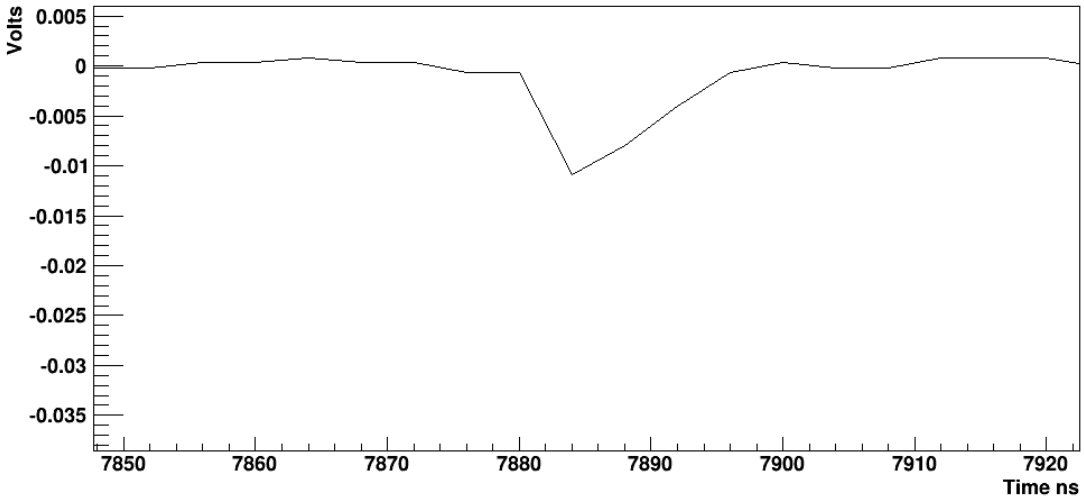

Figure 6.11: An zoomed view of the single PE pulse from above. The x axis is time in microseconds and the y axis is voltage in Volts. The single event is just past the 8.0 microseconds and is 0.012 microseconds in length. The red and green vertical lines show the prompt window.

The Q_{tot} of the single pulses was taken for varying time windows as seen in Figures 6.12 - 6.15 .The purpose of examining the different time integrations windows was to determine the window with cleanest signal of the single PE pulse. Longer time windows show more information about large events in the singles regions. The feature is the pedestal and the second is the singles peak.

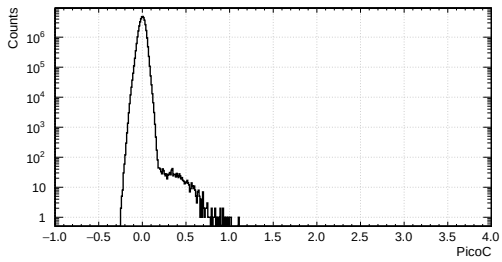

Figure 6.12: Singles calculated using 1 time bins on either side of the selected pulse. The x axis is pico-coloumbs and the y axis is counts.

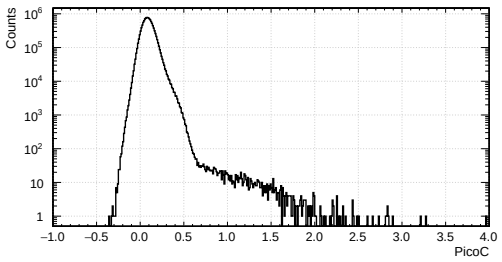

Figure 6.13: Singles calculated using 2 time bins on either side of the selected pulse. The x axis is pico-coloumbs and the y axis is counts.

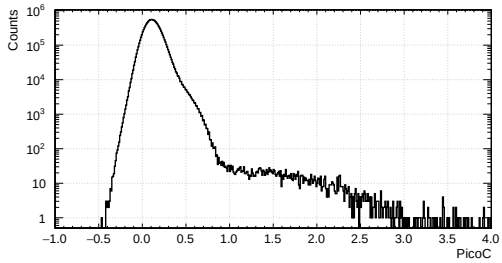

Figure 6.14: Singles calculated using 3 time bins on either side of the selected pulse. The x axis is pico-coloumbs and the y axis is counts.

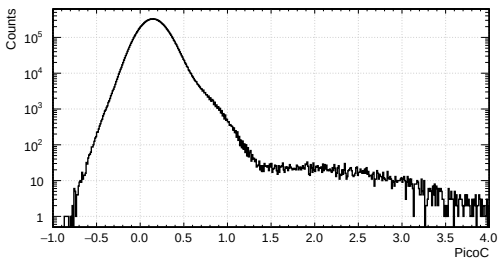

Figure 6.15: Singles calculated using 5 time bins on either side of the selected pulse. The x axis is pico-coloumbs and the y axis is counts.

Single PE Conversion

The PMT used in this experiment is a Hamamatsu R6091-Mod [165] with typical anode gain 5.0×10^6. Using the charge of an electron, 1.602×10^{-19} C, the single photon charge is calculated as

$$(1.602 \times 10^{-19}\, C)5.0 \times 10^6 = 8.01 \times 10^{-13}\, C = 0.801\, pC. \tag{6.5}$$

The measured PMT voltage is integrated over time to obtain charge in Volt-nanoseconds

(V·ns). This can be converted in Coulombs using,

$$Q = \int_{t_i}^{t_f} I dt, \tag{6.6}$$

where Q is charge and I is the current [166]. Substituting Ohm's Law [167],

$$V = IR \tag{6.7}$$

where V is voltage and R is resistance, Q becomes

$$Q = \frac{1}{R} \int_{t_i}^{t_f} V dt. \tag{6.8}$$

The resistance on the data acquisition set up was 50 Ω. Using this, the expected single photon charge in Volt-nanoseconds is 0.0400 V·ns.

In all three runs the single photoelectron charge was found to around 0.3 pC or 0.015 V·ns. This is less than half of the expected. The details of how these values were obtained are discussed in the following section.

Measuring Single PE Charge From Data

The argon run will be used an an example for the calculation of the single's pulse. In the first argon run, the PMT was run at voltage of 1500 V and the trigger threshold was set at -8 mV. The singles finding code was run over 20 files of untagged background data. Each data file contained 200,000 thousand waveforms. Figure 6.16 shows the results of the singles code run over the late waveform and Figure 6.17 shows the result of the singles code run over the first 800 ns. In both fits, the singles charge is 0.285 pC or 0.0143 V·ns. The residuals of the fits are found in Figures 6.18 and 6.19.

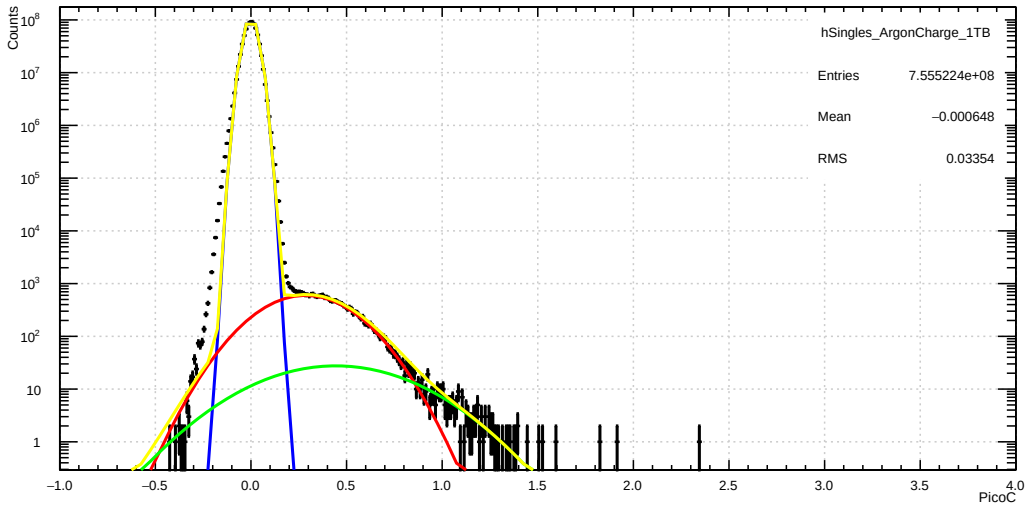

Figure 6.16: This details the singles found in the 8000 ns after the trigger time. The x axis is pC and the y axis is counts. This has been fit with three Gaussians. The mean of the first Gaussian (pedestal) shown in blue is -4.05e-04±5e-04 pC, the mean of the second Gaussian (single PE) shown in red is 2.85e-01 ±2e-01 pC, and the mean of the third Gaussian, shown in green is 4.44e-01 pC±3e-01. (The third gaussian is used to fit out the remaining features, there was enough data to get the double PE peak.) The sum of the three Gaussians is shown in yellow.

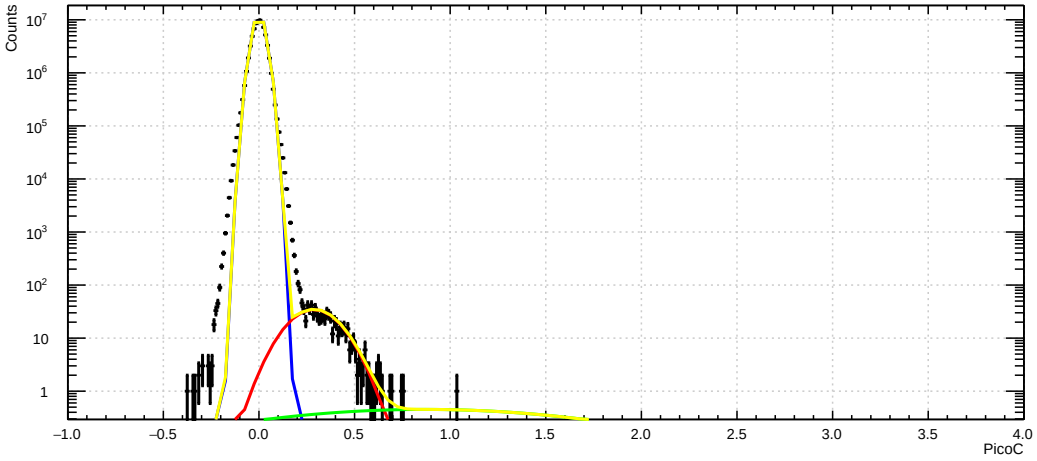

Figure 6.17: This details the singles found in the first 800 ns. The Q_{tot} is from the time of the event until the end of the window. The x axis is pC and the y axis is counts. This has been fit with three Gaussians. The mean of the first Gaussian (pedestal) shown in blue is 2.02e-04±9e-04 pC, the mean of the second Gaussian (single PE) shown in red is 2.87e-01±5e-01 pC, and the mean of the third Gaussian, shown in green is 8.69e-01±6e-01 pC. The sum of the three Gaussians is shown in yellow.

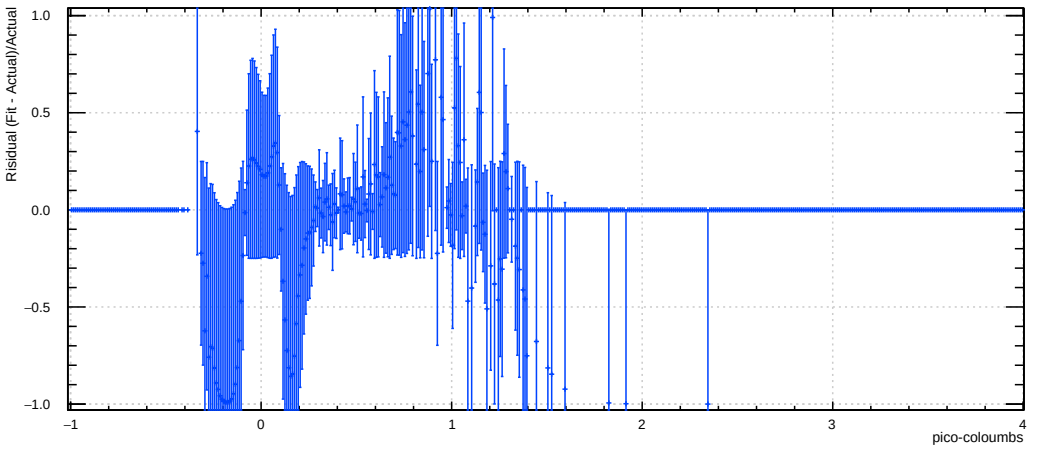

Figure 6.18: The residuals of the thee Gaussian fit of the singles obtained from late charge window of the first argon fill. The x axis is charge in pC and the y axis is are the residuals.

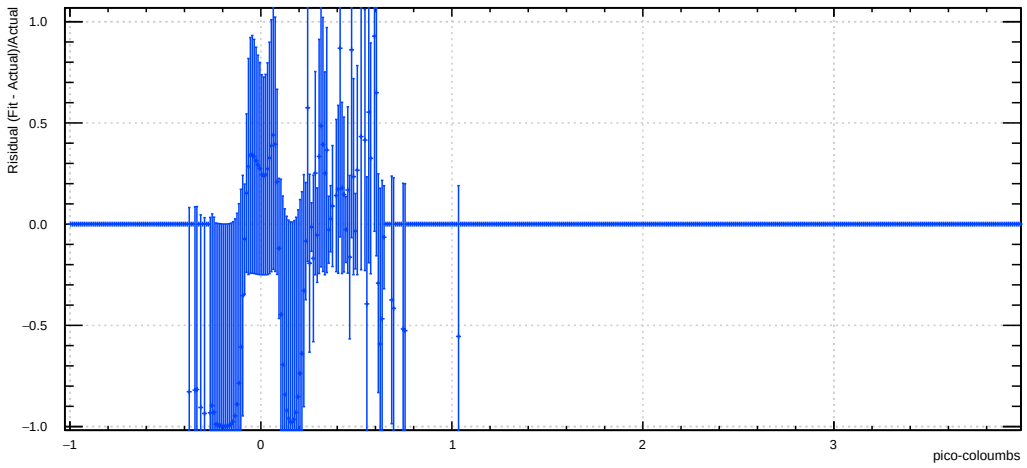

Figure 6.19: The residuals of the thee Gaussian fit of the singles obtained from early charge window of the first argon fill. The x axis is charge in pC and the y axis is are the residuals.

Single Pulse Charge For the Three Data Runs

In the second argon run, the PMT was run at voltage of 1500 V and the trigger threshold was set at 8 mV. The singles finding code was run over 14 files of untagged background data. Each file consisted of 200,000 waveforms. In the fit of late singles, the single photoelectron charge was 0.30 pC or 0.015 V·ns and the early singles had a fit of single charge of 0.34 pC or 0.017 V·ns.

In the third argon run, the PMT was run at voltage of 1650 V and the trigger threshold was set at 8 mV. In this case the mean of the single photoelectron peak is 0.33 pC or 0.0165 V·ns. This run had insufficient statistics to calculate a single's charge from the early window.

The values for the singles pulses for all the runs can be be found in Table 6.2.

Fill	Singles Charge (V·ns)	χ^2/ndf
Argon 1	2.85×10^{-1}	$3.0 \times 10^6/133$
Argon 2	2.96×10^{-1}	$1.0 \times 10^6/113$
Argon 3*	3.28×10^{-1}	$1.99 \times 10^{-5}/78$

Table 6.2: Single PE charge for each argon fill. The large χ^2/ndf was mostly impacted by the pedestal peak. In the third argon fill there were insufficient statistics, so a larger time window was used.

6.3 Second Pass Analysis

The second pass analysis ran over the first pass analysis file from both source runs and background runs. Data from both files were filtered through a variety cuts to eliminate junk events and non signal events. The remaining data was then rate normalized and back round subtracted. Figure 6.20 shows a flow chart of the basics of the first pass analysis. The data cuts are described in greater detail below.

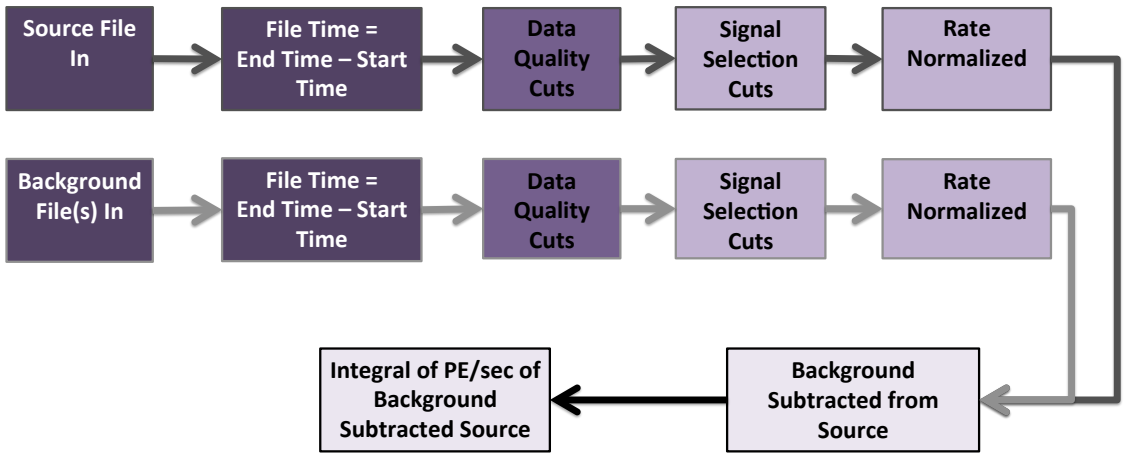

Figure 6.20: A flow chart depicting the data flow for the second pass analysis for the single PMT set up.

6.3.1 Data Quality Cuts

The cleaning cuts were used to eliminate events that were outside the signal region. This included saturated events, events with the V_{peak} outside of the trigger window. The data quality cuts were applied before background subtraction

Trigger Time Cut (Single PMT Set Up Only) The trigger time window was set at 2640 nanoseconds into the waveform via the data acquisition software. The trigger time for each waveform was set according to the time the largest voltage in the waveform was recorded. Events were kept that satisfied the condition of having the largest pulse occur between 2640 ns and 4140 ns. The 2640 ns was chosen from the DAQ system. The 4140 ns ending point is the turn on time plus the triplet lifetime. This cut was not used in the data with the tagging set up as the time difference between the two PMT's was to discriminate between source and background.

Trigger Time Difference Cut (Double PMT Set Up Only) The trigger time cut was not used in the double PMT set up. In its place, a condition for trigger time difference was used to discriminate against events not from the source. Figure 6.21 is an example of the trigger time difference between the argon PMT and the tagging PMT. The data acquisition was set to acquire when the trigger threshold was was met for both PMT's in a 120 ns time window regardless of order. A cut was placed to accept events with a time difference of 4 ns and 60 ns, Figure 6.21. This eliminates events where the argon PMT triggered first.

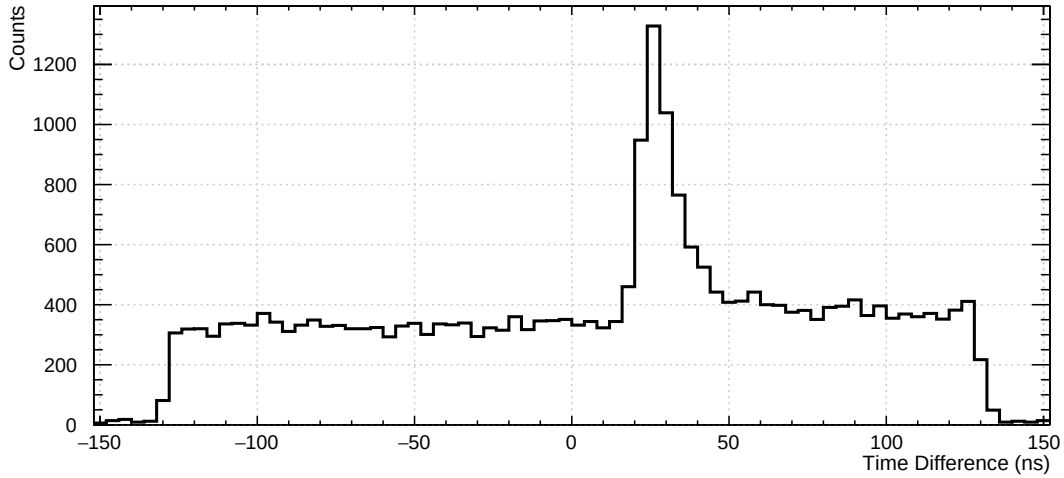

Figure 6.21: Trigger time difference between the argon PMT and the tagging PMT. The x axis is the time difference in ns and the y axis is the counts/bin.

Voltage Saturation Cut The maximum voltage detected by the PMT was 2 V. Events with a peak larger than 2 V were saturated and needed to be eliminated. We implemented a cut to remove events with a peak value lager than 1.8 V. The peak just before 2.0 V are the events with saturation. The voltage threshold for triggering was set to 8 mV. An additional cut in data was done to remove any events with a V_{peak} less than 8 mV, the trigger threshold.

Baseline Sigma Cut The baseline line sigma corresponds to the value of the calculated sigma for the baseline voltage. The baseline voltage are the voltage readings in the first 1000 nanoseconds. Events with values less than 0.4 mV and events with a value less than 0.7 mV where eliminated. This was determined by fitting the baseline distribution and including events within 7 sigma of the mean.

Charge Cut The Q_{tot} of each pulse was calculated from time the of the peak voltage until the end of the waveform. Events with a negative integral value were cut. The negative value resulted from the variability of the baseline voltage between pulses indicating noise.

Sodium PMT Cut Peak Value Cut The voltage from the tagging PMT, (the PMT that was tagging sodium events) was recorded in double PMT runs. This was used to discriminate events that triggered a tag not caused by the source. Figure 6.22 shows the sodium spectrum for the second argon fill. A cut was placed to eliminate events tagged by the sodium PMT with a threshold greater than 0.7V. This is the full range of the spectrum of events caused by something within the sodium spectrum on the tagging PMT. Figure6.23 details the spectrum on the tagging PMT when a source was not installed. The majority of the background triggering events would be caused by an event larger than the 0.7V.

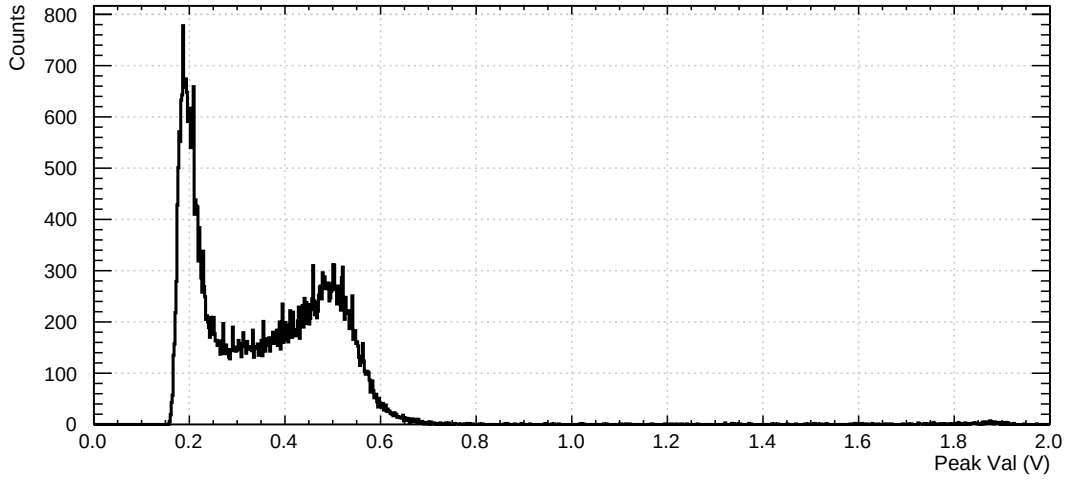

Figure 6.22: Sodium spectrum on the tagging PMT in the second argon fill. The x axis is peak voltage in V and the y axis is counts/bin. The 511 keV peak is around 0.2 V and the 1274 keV peak is around 0.5 V.

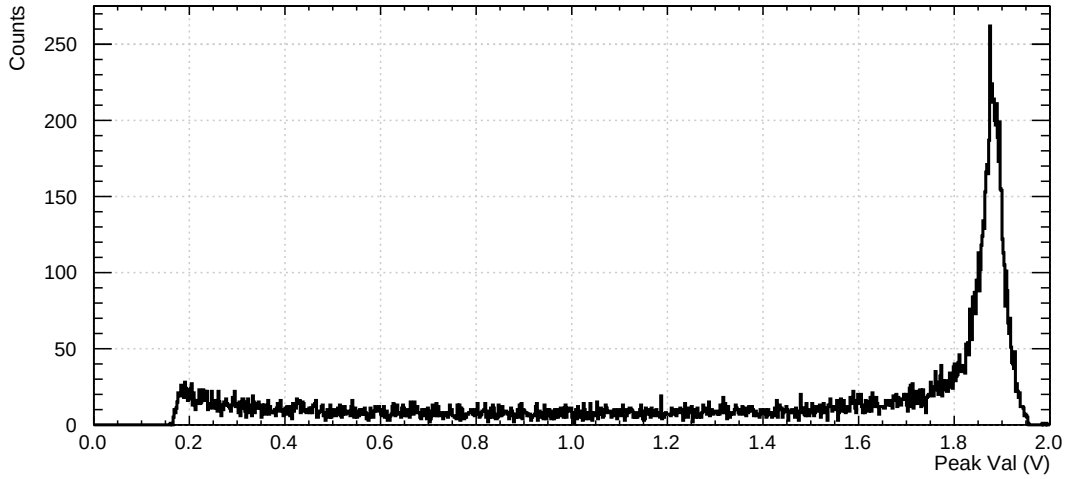

Figure 6.23: Background voltage spectrum for untagged background in the second argon fill. The x axis is peak voltage in V and the y axis is counts/bin. The lack of sodium source present means there is no spectrum. This demonstrates the majority of tagged background events were high voltage events (cosmic rays, etc.)

Figure 6.24 shows the sodium spectrum for the third argon fill. A cut was placed to eliminate events tagged by the sodium PMT with a threshold greater than 1.8 V. Figure 6.25 shows the spectrum on the tagging PMT when a source was not installed. It is clear that the majority of the background triggering events would be caused by an event larger than the 1.8 V.

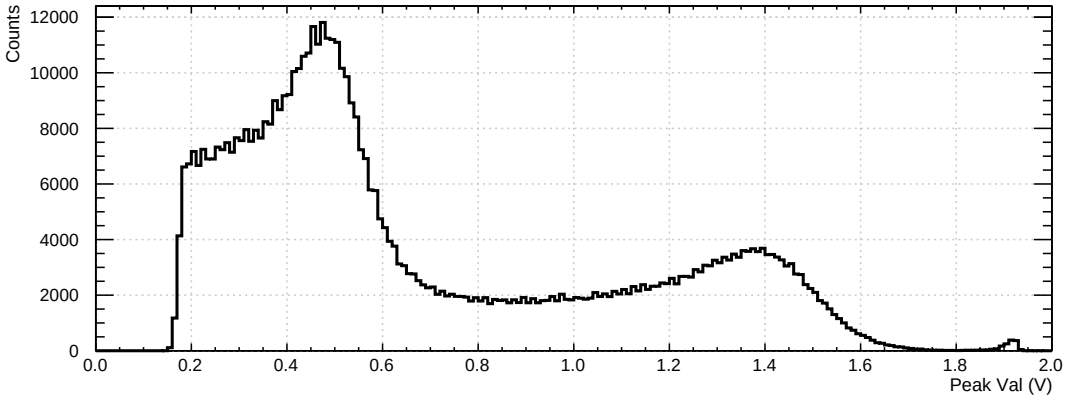

Figure 6.24: Sodium spectrum on the tagging PMT in the third argon fill. The x axis is peak voltage in V and the y axis is counts/bin.

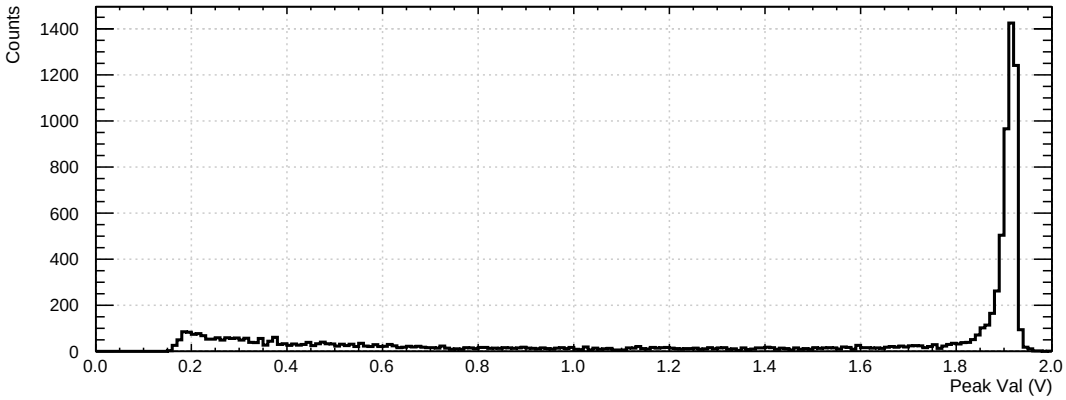

Figure 6.25: Background voltage spectrum for untagged background in the third argon fill. The x axis is peak voltage in V and the y axis is counts/bin.

6.3.2 Signal Section Cuts

The signal extraction cuts occurred after the the data quality cuts. The cuts were set by examining the data after these cuts. These cuts were used to extract signal that came from the radioactive source placed on the collimator.

Cuts Applied to Both the Single PMT Set-Up and the double PMT Set-Up

F_{prompt} Cut Gamma events in liquid argon cause electronic recoil events. Unlike nuclear recoil events, these have a lower F_{prompt} value. An example of the F_{prompt} with the electronic recoil and nuclear recoil peaks can be found in 6.26. This shows the F_{prompt} vs PE from several background runs taken in the first data run. The F_{prompt} cut was determined by fitting the electronic recoil peak for background subtracted data. The cut was then made to exclude events that were greater than three sigma from the mean. This resulted in discarding values with an F_{prompt} less than 0.1 and greater than 0.6.

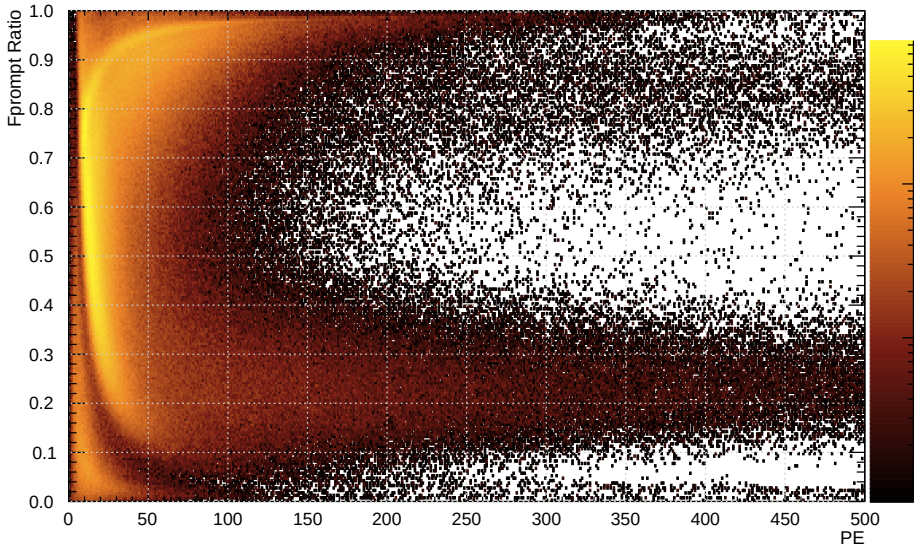

Figure 6.26: A plot comparing the photoelectrons in an event to the F_{prompt} ratio. This is untagged background data taken in the first data run. The x axis is the PE count, the y axis is the F_{prompt} ratio. The electronic recoil peak can be seen between the F_{prompt} values of 0.05 and 0.5. The nuclear recoil peak is between the values of 0.6 and 0.95.

Cut Based on the Relationship of Peak Voltage to Q_{tot} Charge The peak voltage was plotted against the Q_{tot} for each data run. This resulted in a distribution with two

populations. This is shown in Figure 6.27. The upper population events are signal events.

Figure 6.27 shows this relationship before cuts and Figure 6.28 shows this relationship after cuts were applied. The cuts removed the majority of events in the lower population. The remaining events were removed using the following method.

To make the cut, the upper population is fit with a first order polynomial,

$$V_{peak}(Q_{tot}) = (85.13Q_{tot} - 5.83). \tag{6.9}$$

Events with a values below the polynomial were removed. In the plots shown below (Figure 6.27 and Figure **??**), these are all the events below the blue line

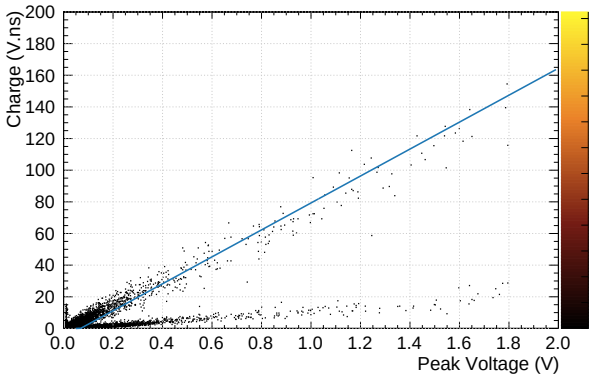

Figure 6.27: A plot showing the relationship of the V_{peak} to Q_{tot} charge value before data quality cuts. The x axis is V_{peak} in V and the y axis is charge in Volt-nanoseconds (V·ns). The signal population above the blue line.

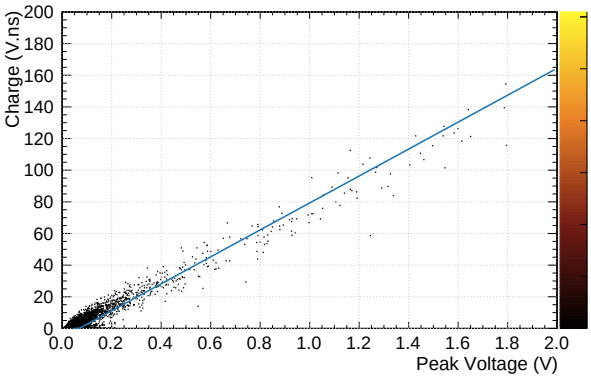

Figure 6.28: A plot showing the relationship of the V_{peak} to Q_{tot} charge value after data quality cuts. The x axis is V_{peak} in V and the y axis is charge in Volt-nanoseconds (V·ns). The signal population above the blue line.

6.3.3 Event Position Cuts (Based on Simulation)

Simulations were done to model the data that was taken during the experiments. (The details of simulation geometry and methods are described in detail in Chapter 4.) This was used to determine additional cuts. In order to use the simulation output as a comparison, it was subjected to cuts to mimic the cuts made in data.

6.3.4 Selection Cuts in Simulation

Peak Voltage The peak voltage in simulation was determined by iterated through all the voltage pulses in a waveform and locating the pulse with the largest voltage value. This was stored as the peak voltage, the time this occurred was stored as the trigger time, similar to the definition of the trigger time in data.

The first cut applied in simulation was a voltage cut. In simulation all events, including low voltage events, would be accepted. A cut was implement to remove low voltage events similar to DAQ voltage threshold. In simulation this cut was placed at 8×10^{-3} V. This was based on voltage scan on the PMT used in the experiment. Setting a threshold below 0.008 V resulted in a signal dominated by dark rate. Figure 6.29 depicts the voltage on the PMT before the threshold cut.

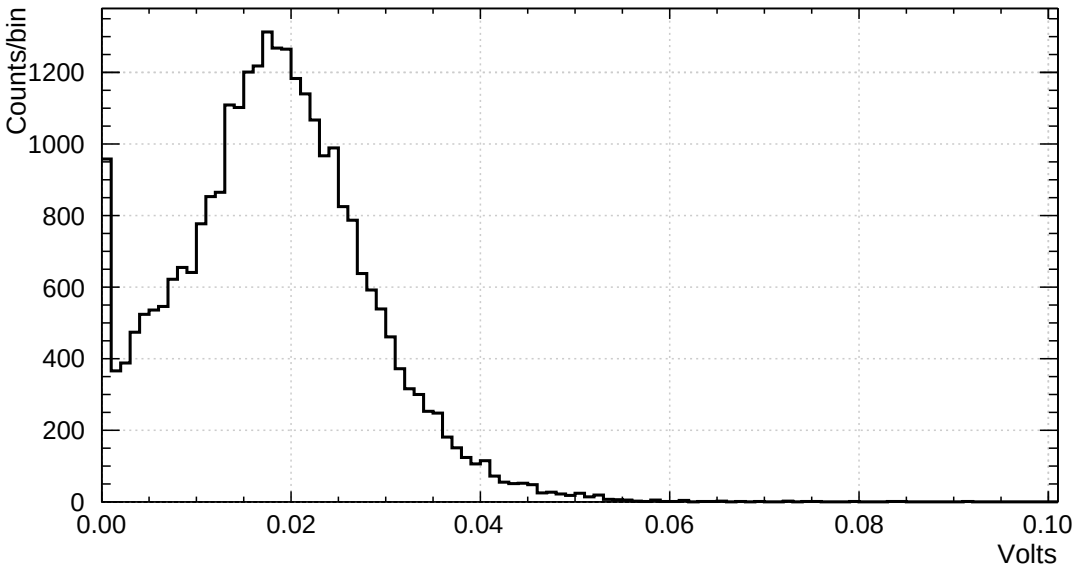

Figure 6.29: The simulation voltage before the threshold cut. The x axis is volts and the y axis is counts.

Event Trigger Time The trigger time of each event in simulation was determined using a similar method as the data analysis code. The charge pulses in each waveform were iterated through until the pulse with the largest voltage value was located. The simulation time of the waveform of the start of the event was recorded as the trigger time. A trigger time cut would later be applied in data, so it was applied in simulation. The was set to include events between 1044, the trigger window in simulation and 2564, the trigger window plus the triplet lifetime of liquid argon. Figure 6.30 depicts the trigger time spread in simulation prior to the trigger time cut.

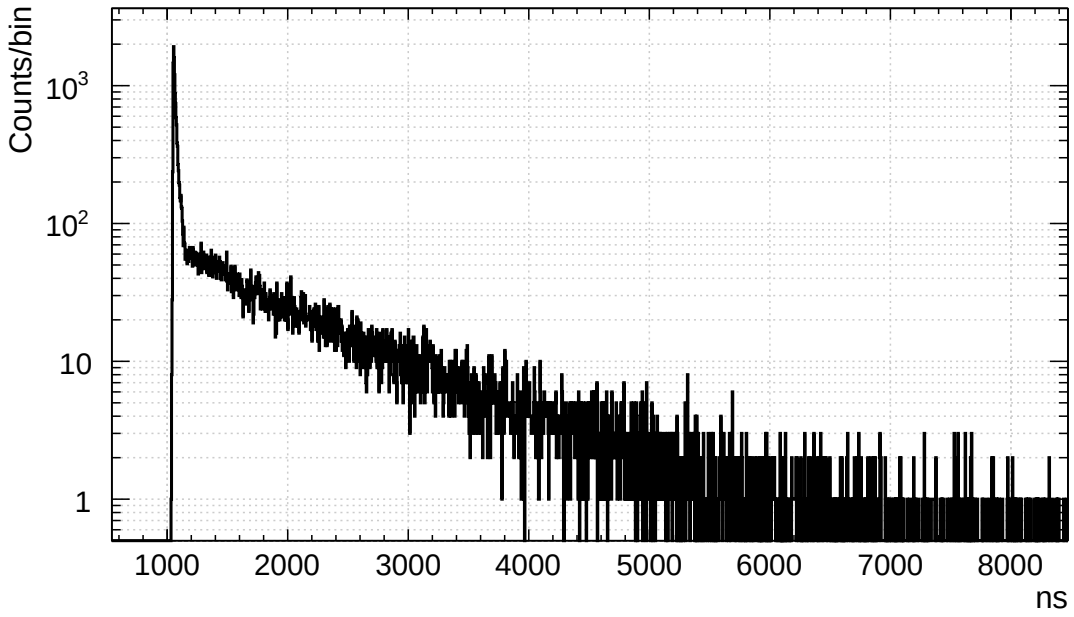

Figure 6.30: Simulation trigger time prior to cuts. The x axis is time in ns and the y axis is counts.

F_prompt The F_{prompt} in simulation was calculated by summing the charge in the pulse 120 ns after the peak pulse (the prompt window), and dividing by the total charge. Figure 6.31 depicts the F_{prompt} distribution in simulation prior to cuts. Cuts were made to eliminate events between less than 0.1 and 0.6. This was chosen as it is a generous estimation of the F_{prompt} region.

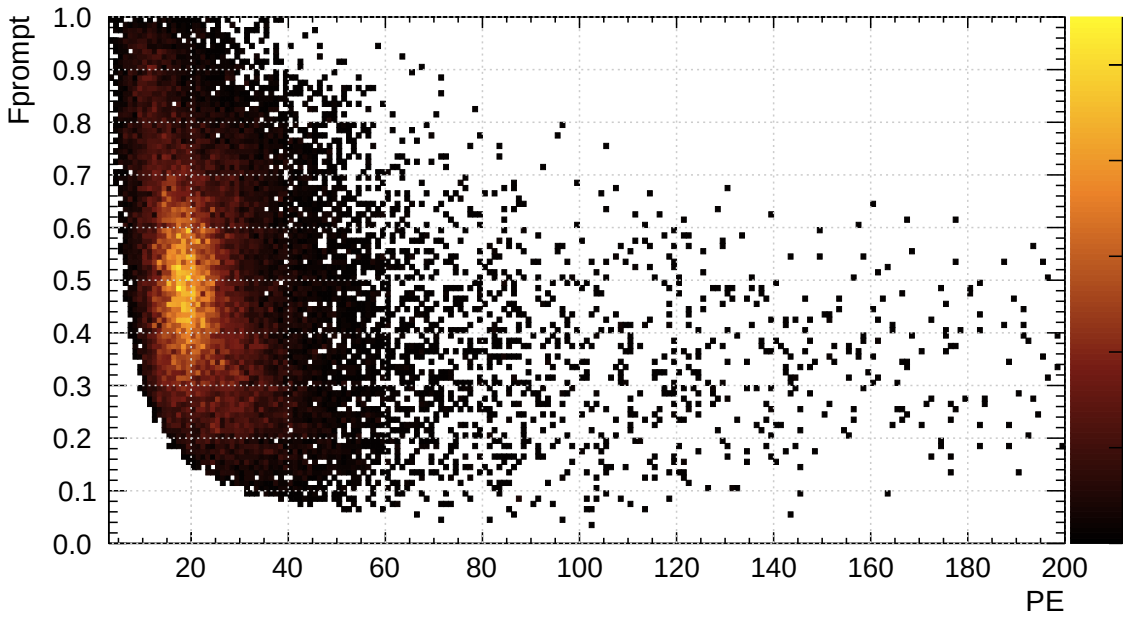

Figure 6.31: F_{prompt} in simulation, prior to cuts. The x axis is PE and the y axis is the F_{prompt} ratio.

PE Cuts Based on Position Events simulated using a collimated isotropic source were subjected to cuts based on the PE generated as function of position. Events with a larger number of PE occurred closer to the window and were outside of the simulated position. To demonstrate how this cut is done, as example is shown using a ^{137}Cs simulation at 21 cm. An example can be see in Figure 6.32

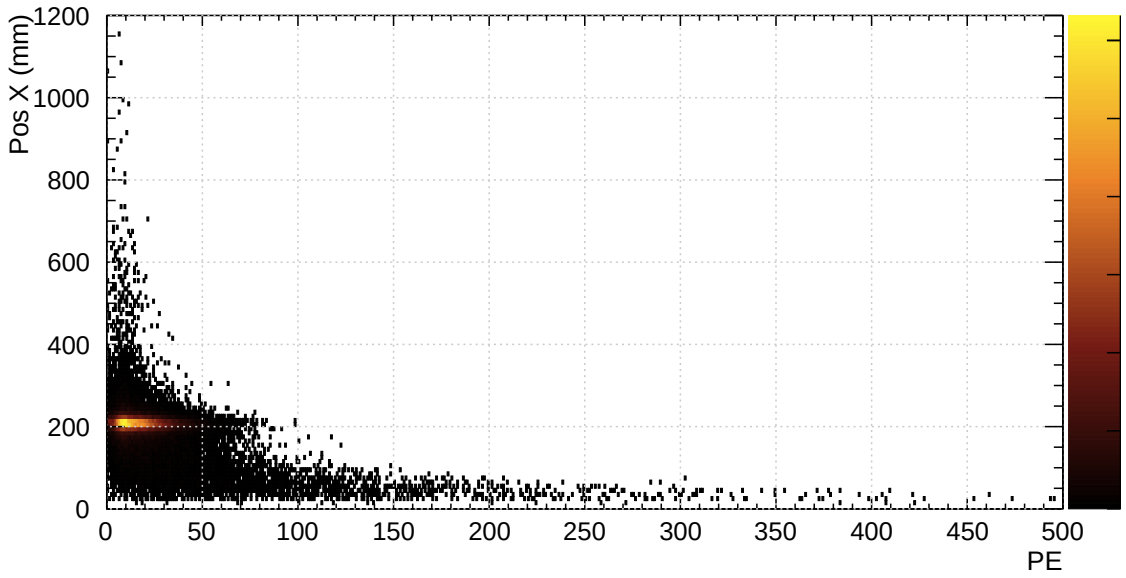

Figure 6.32: Position from the window in simulation at 21 cm using a ^{137}Cs energy (662 keV). The x axis is PE detected and the y axis is position the simulation event occurred from the window in cm.

To determine the position range to consider for the PE cut, the event position was plotted as a function of distance from the window. This is shown in Figure 6.33. The peak position was fit with Gaussian. The result of this Gaussian were used to cut events that did occur within 3 sigma of the mean of the Gaussian.

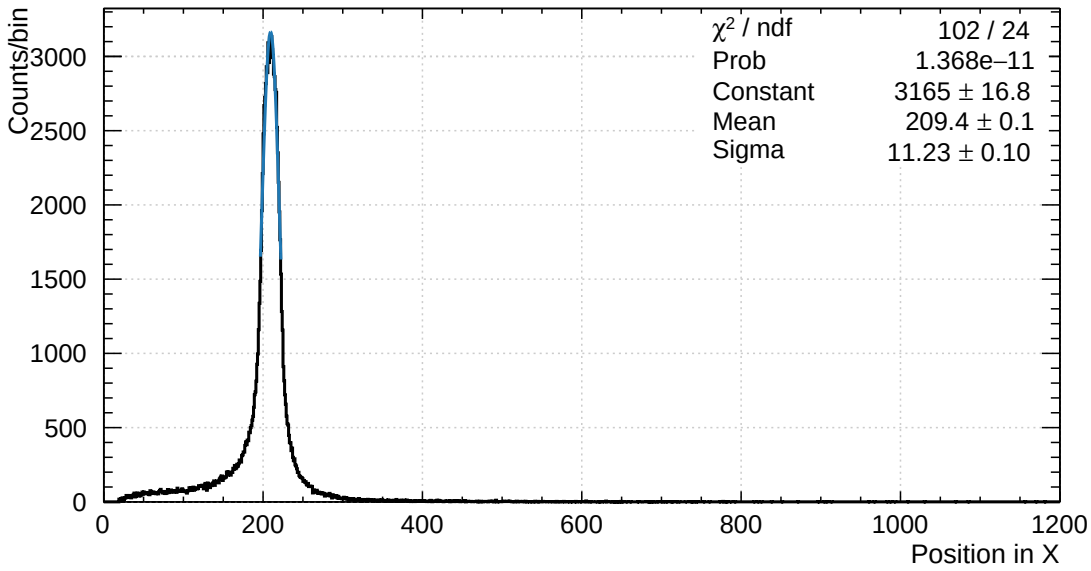

Figure 6.33: Position from the window in simulation. The x axis is distance from the window in cm and the y axis is counts. This has been fit with a Gaussian to determine the mean position.

The PE of the events that passed cut were then plotted. An example is shown in Figure 6.34 .The mean of this plot was fit with Gaussian and events with a PE greater than 5 sigma were cut in the final simulation analysis.

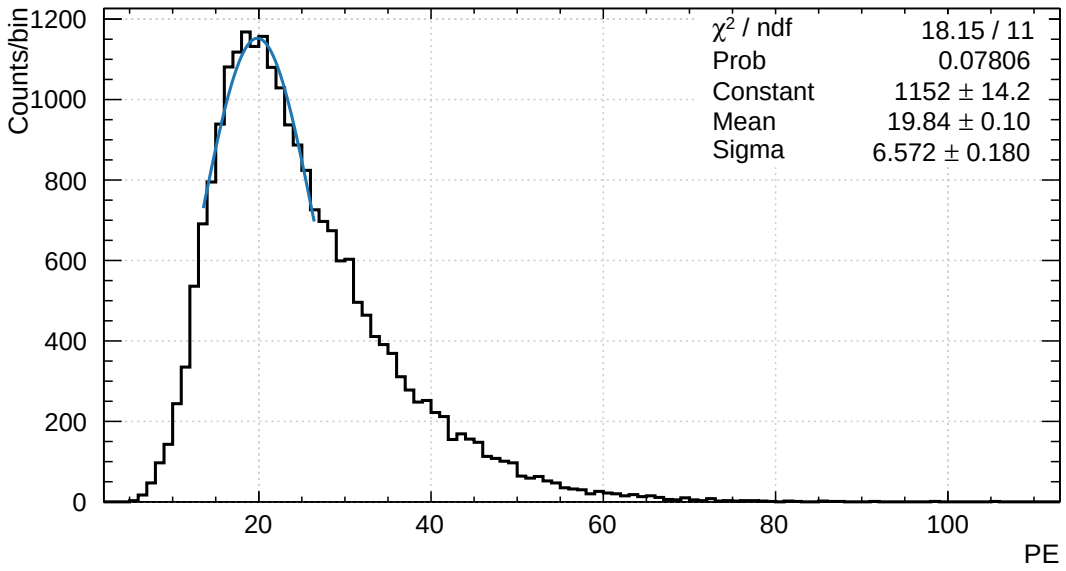

Figure 6.34: Position from the window in simulation. The x axis is distance from the window in cm and the y axis is counts. This has been fit with a Gaussian to determine the mean position.

6.3.5 Rate Normalizing Simulations

The simulations were rate normalized to match the rates of the gamma sources on campus. In the case of the ^{137}Cs, the rates for the sources used are in table 5.2 in Chapter 5.

In an isotropic gamma simulation, the events were rate scaled but dividing the total number of events simulated by simulation rate. For example, ^{137}Cs simulations were done with 100 million events. This was scaled using

$$t_S = \frac{S_{events}}{^{137}Cs_{Rate}} = \frac{1.0 \times 10^8 [events]}{5.4755 \times 10^5 [\frac{events}{s}]} = 182.6s. \tag{6.10}$$

An example of the rate normalized PE in simulation is found in Figure 6.35.

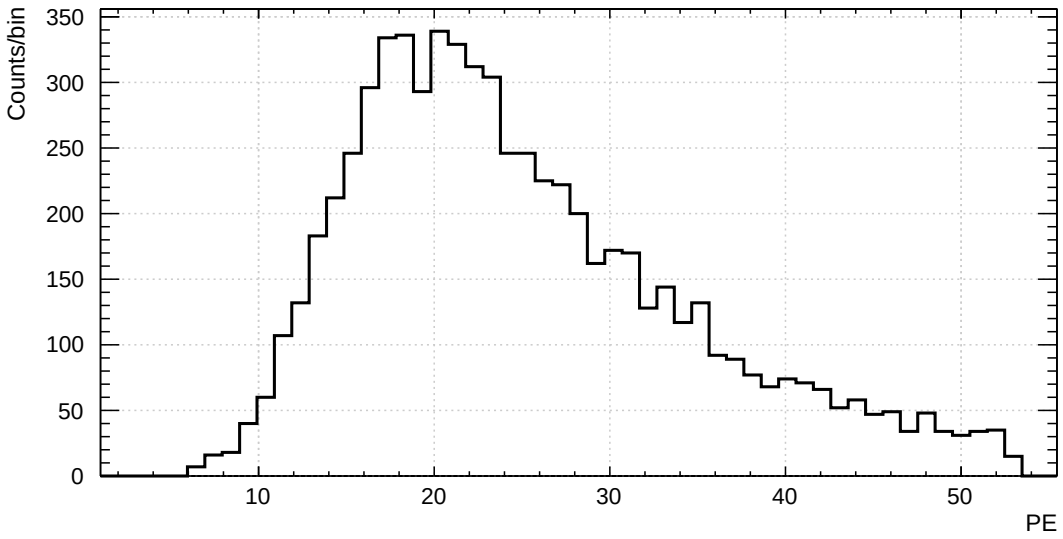

Figure 6.35: PE rate in simulation after cuts. The x axis PE and the y axis is counts/sec.

Comparing Simulation to Data

In order to use the simulation as a means to determine cuts, first the simulation had to be shown to describe the data acquired within error. The following details the process using ^{137}Cs simulations. The same process was also used for ^{22}Na simulations and data.

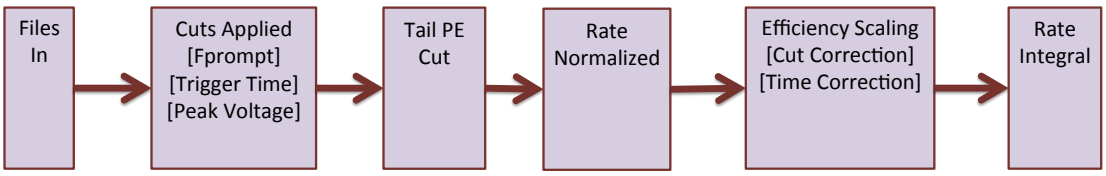

Figure 6.36: A flow chart detailing the processing of simulation data.

^{137}Cs was analyzed in the following way. Trigger time cuts, F_{prompt} cuts, and V_{peak} cuts were applied to match the cuts in data. Next the simulation was rate normalized.

This was done by scaling the number of events simulated to the rate of the source used in experiment. In the case of the ^{137}Cs simulations, the source rate used in the experiment is 548 kBq (table 5.2, Chapter 5). One hundred million events were isotropically simulated. This corresponds to

$$t_S = \frac{S_{events}}{^{137}Cs_{Rate}} = \frac{1.0 \times 10^8}{5 \times 10^5 [1/s]} = 180.0\, s. \tag{6.11}$$

This simulation time was used to rate normalize the events simulated.

Next the simulation was multiplied by two scaling factors. The first was to correct for a discrepancy between the data acquisition rate of the DAQ system with the rate events counted with the Arduino counter. The data system acquired 56% fewer events during a data run than measured by Arduino counter. The simulation rate would be similar to the rate the rate of the Arduino counter as no time was lost for file writing. Simulation was scaled by 0.44 to correct for this difference.

The cut efficiency in simulation did not match data. Table 6.3 demonstrates the difference between the survival rates by position of cuts applied in both simulation and in data. This difference was corrected by scaling the simulation to match the survival rate of the data.

Position	Other Cuts	V_{peak} Plus Previous	$T_{trigger}$ Plus Previous	Q_{tot} vs V_{peak} Plus Previous	F_{prompt} Plus Previous	PE Max Plus Previous
Data						
25 cm	96.58%	96.35%	71.98%	66.60%	18.45%	12.59%
30 cm	97.71%	97.59%	74.86%	67.37%	20.24%	12.69%
40 cm	96.72%	96.21%	73.00%	65.89%	18.83%	11.94%
50 cm	97.63%	97.20%	74.36%	66.75%	19.85%	11.77%
70 cm	96.88%	96.39%	73.42%	65.98%	19.29%	11.43%
Simulation						
25 cm	100.00%	100.00%	95.29%	95.29%	68.87%	63.84%
30 cm	100.00%	100.00%	93.69%	93.69%	67.02%	56.32%
40 cm	100.00%	100.00%	93.01%	92.85%	67.41%	52.32%
50 cm	100.00%	100.00%	78.84%	78.84%	66.68%	47.79%
70 cm	100.00%	100.00%	75.04%	75.04%	63.39%	46.10%

Table 6.3: Percent Survival for ^{137}Cs simulation and data. The data is background subtracted

Lastly the Q_{tot} of the rate was taken. This method is detailed in 6.36.

Next, the simulation was compared to data to ensure agreement in the peaks. This was necessary before using simulation output as a method for making data cuts. Data plotted with simulation can be found in 6.37. What to observe in this figure is the agreement of the means of the peaks.

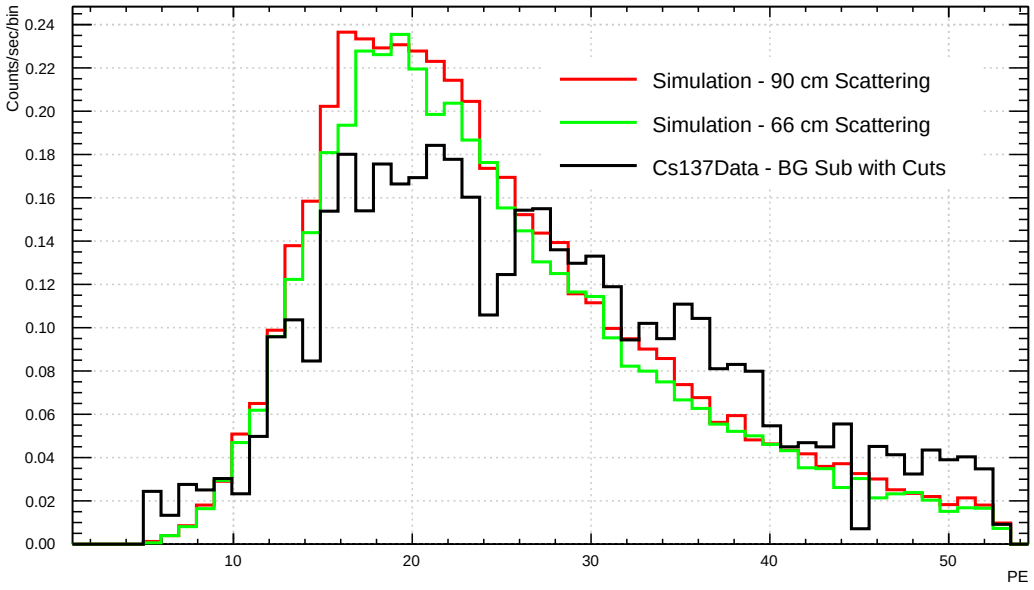

Figure 6.37: ^{137}Cs simulation compared to background subtracted data. The x axis is PE and the y axis is counts/sec. The red trace is simulation with 90 cm scattering, the green trace is simulation with 66 cm, and the black trace is background subtracted data. The simulation has been scaled and the plots have be area normalized to better compare the mean peaks.

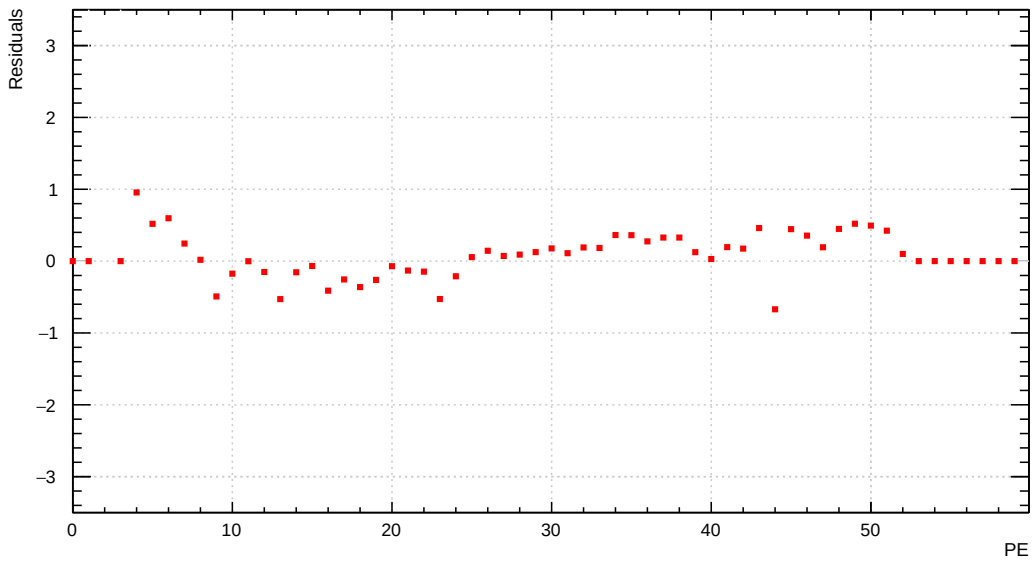

Figure 6.38: Normalized residuals comparing ^{137}Cs simulation with 66 cm to data. The x axis is PE and the y axis is normalized residuals. The χ^2/ndf is 5.7/48 = 0.12.

There was a difference in rates between the simulation and data. This is likely caused be a difference in the lead shielding in simulation as compared to data acquisition.

The PE of the peaks between simulation and data was compared for each position measured in ^{137}Cs. The results are in Table 6.4. For each position, the data and simulation are in agreement within error.

Position	Data Mean	Simulation Mean
21 cm	19.±7	19±6
30 cm	21±6	19±6
40 cm	20±11	19±5
50 cm	20±8	19±6
70 cm	19±8	20±5

Table 6.4: Comparison of simulation and data mean PE peaks by position. These were obtained by fitting the top of each peak with a Gaussian. The error is the sigma on the Gaussian.

Determining Cuts Based on Simulation

Cut were applied to the simulation to eliminate events outside of the position by doing a PE cut based on the PE generated at the position. This was done to eliminate background from the source that has occurred outside of position. Due to the nature of the solid angle, scintillation events that occur close to the window are more likely to be detected. This is also true for the ^{39}Ar background. This can be seen in Figure 6.39.

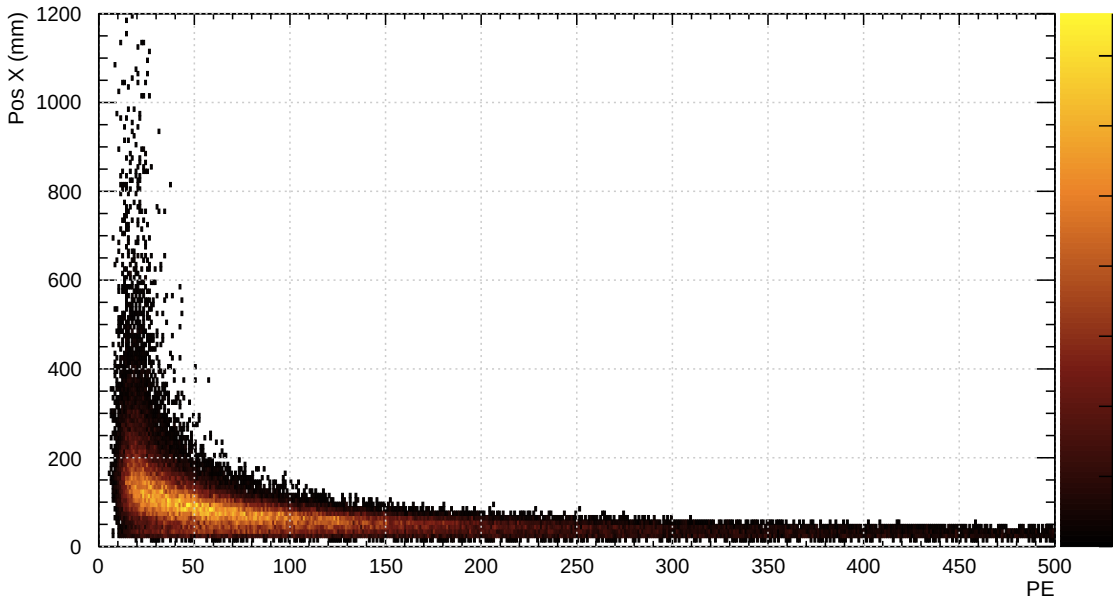

Figure 6.39: ^{39}Ar simulated in the detector plotted by event position. The x axis is PE and the y axis is position in the detector. Events with a greater number of PE occurs close to the window and are a source of background.

A cut was placed on the data for a maximum PE based on the position study in simulation.

6.4 Data Corrections

Once all of the cuts were applied to both the source and background file(s). The final step was to subtract the background from the source and take the integral of the result. The following plots show this for both ^{137}Cs and ^{22}Na for the first argon fill. Figure 6.40 and 6.41 shows the source rate after all the cuts had been applied, but before background subtraction in ^{137}Cs and ^{22}Na respectively.

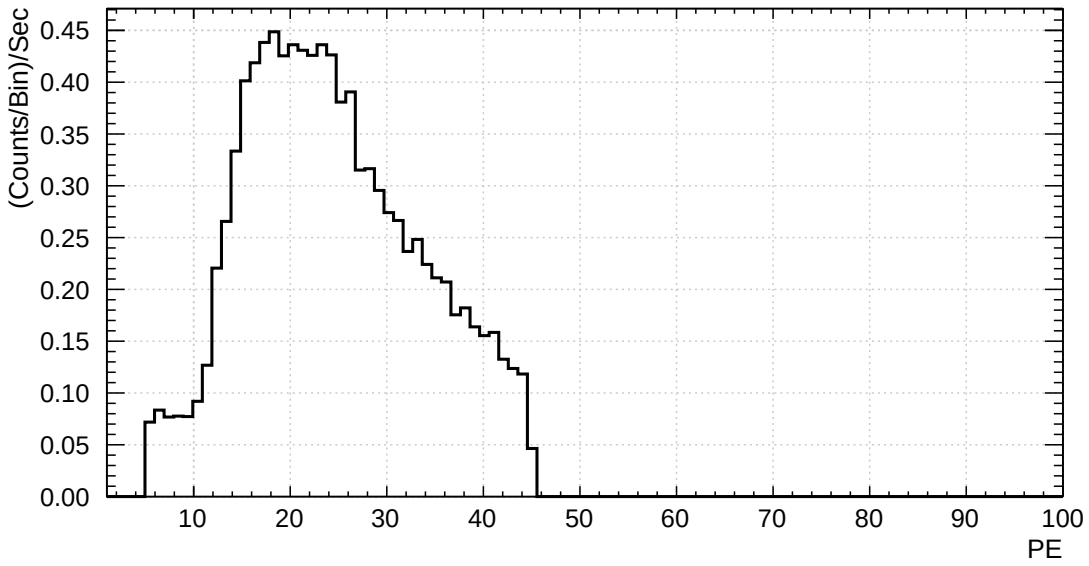

Figure 6.40: Rate normalized ^{137}Cs data after cuts and before background subtraction. The x axis is PE and the y axis is (counts/bin)/second. This is from the 40 cm position.

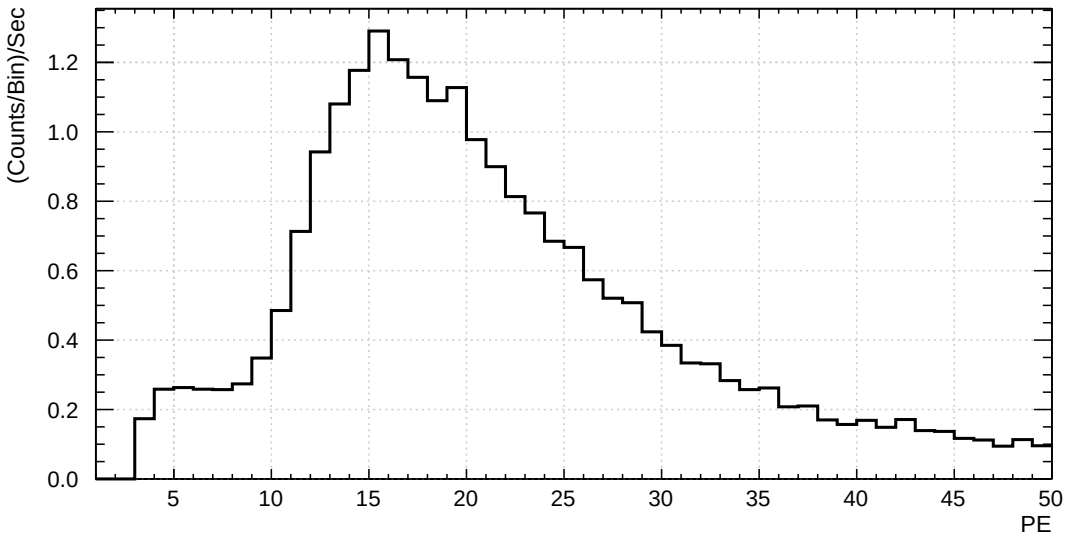

Figure 6.41: Rate normalized ^{22}Na data after cuts and before background subtraction. The x axis is PE and the y axis is (counts/bin)/second. This is from the 39cm position.

Figure 6.42 is the background data rate normalized with all the cuts applied. The rate of the ^{137}Cs was 25.0% higher than background at the 40 centimeter position. At the 39 cm, with the ^{22}Na source, the source rate was 74.5% higher than the background rate, as shown in figure 6.43.

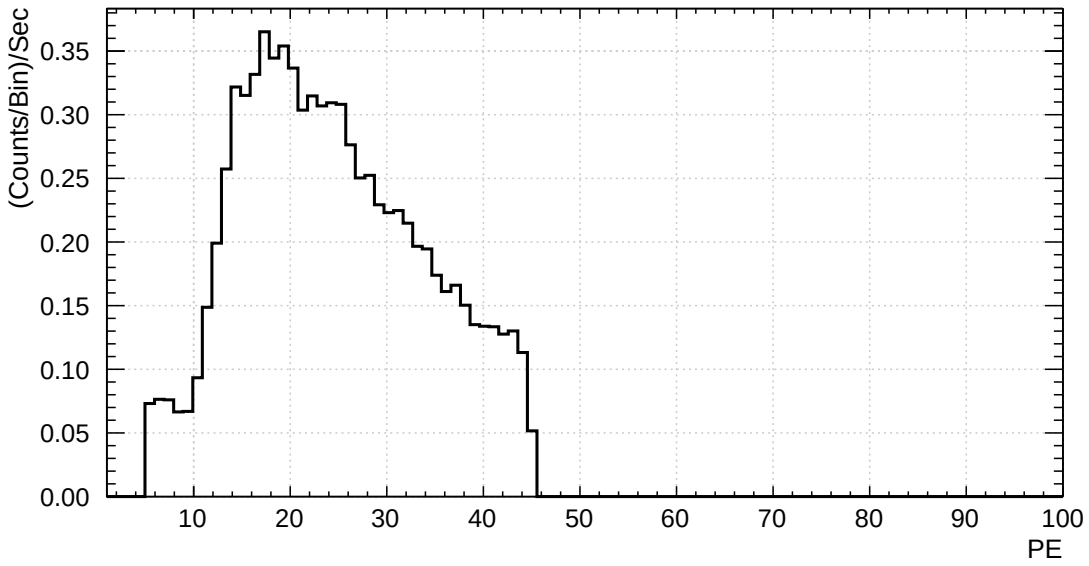

Figure 6.42: Rate normalized background data from the ^{137}Cs data acquisition after cuts. The x axis is PE and the y axis is (counts/bin)/second.

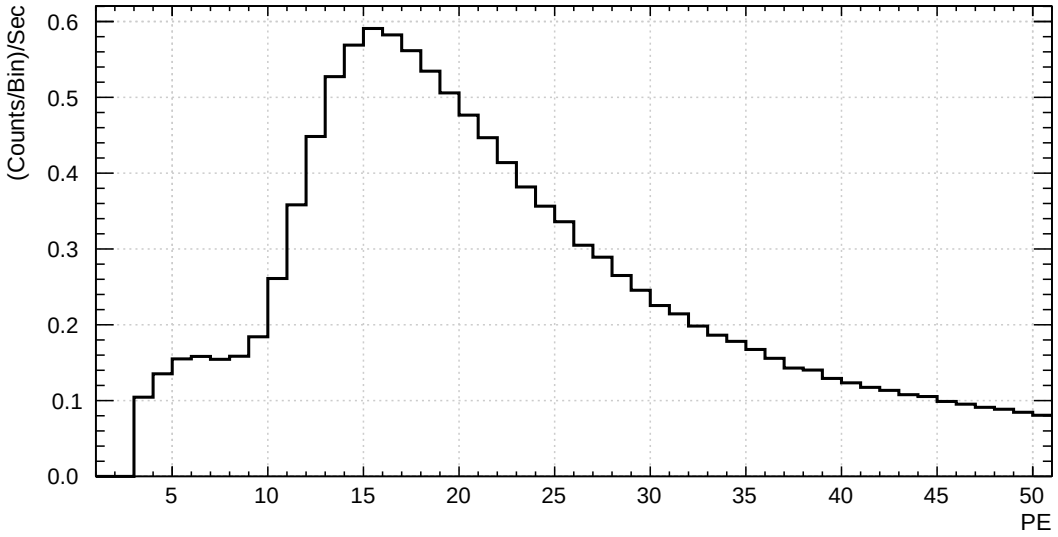

Figure 6.43: Rate normalized background data from the ^{22}Na data acquisition after cuts. The x axis is PE and the y axis is (counts/bin)/second.

The result of the background subtraction is shown in for ^{137}Cs in figure 6.44 and for ^{22}Na in figure 6.45.

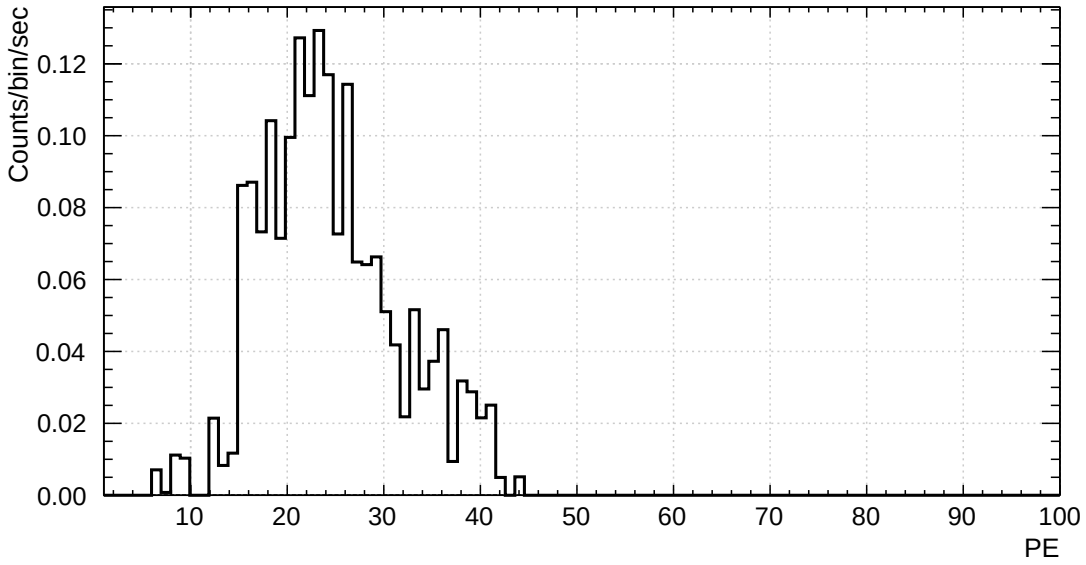

Figure 6.44: Rate normalized ^{137}Cs data with cuts and background subtracted. The x axis is PE and the y axis is (counts/bin)/second. This plot was used to calculate the integral. This is from the 40 cm position.

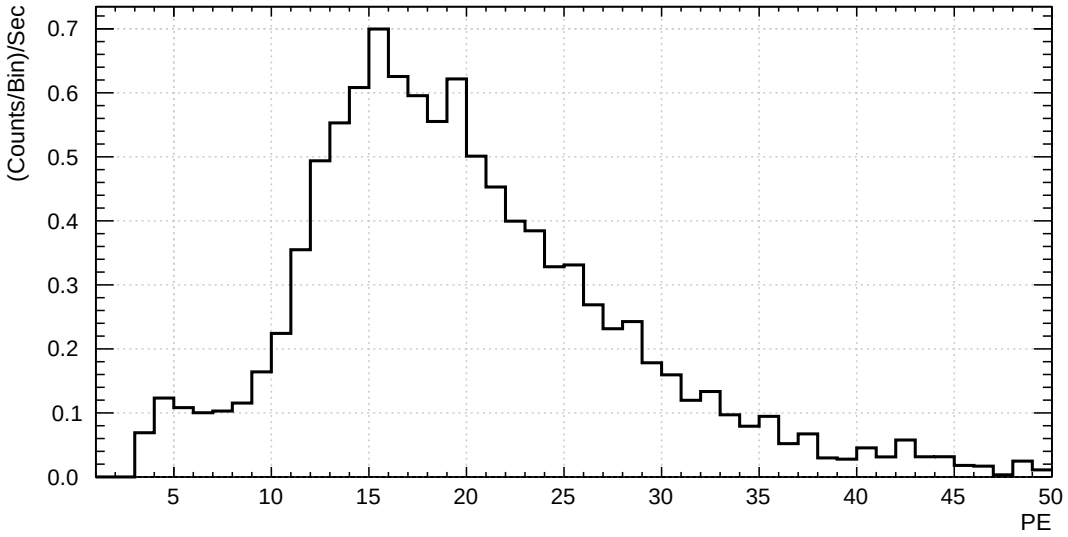

Figure 6.45: Rate normalized ^{22}Na data with cuts and background subtracted. The x axis is PE and the y axis is (counts/bin)/second. This plot was used to calculate the integral. This is from the 39 cm position.

Second and Third Argon Fills

The second and third argon fills were used to understand the background contribution better but implementing a tagging system, as well as adding an aperture to the front window. The third argon fill suffered from very low statistics due to the choice of such a small front aperture.

Figure 6.46 shows the PE rate after cuts and before background subtraction at 38.5 cm. The data runs in this argon fill had low statistics.

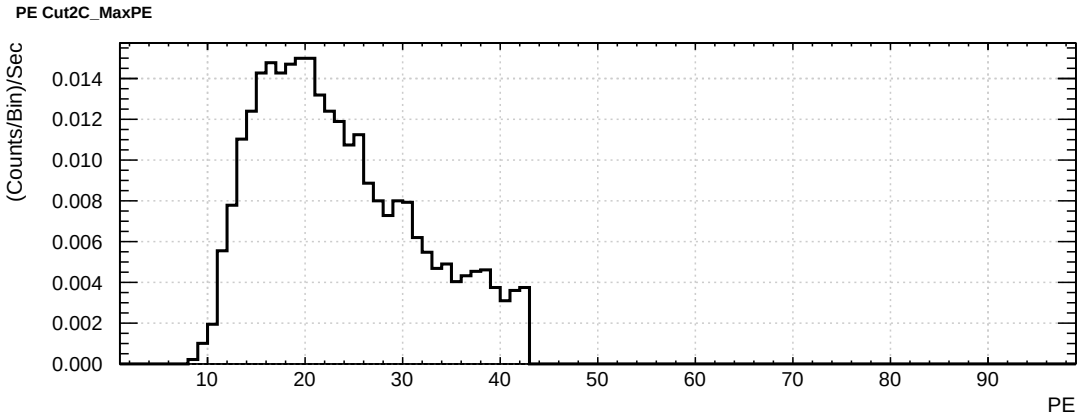

Figure 6.46: Rate normalized ^{22}Na data after cuts and before background subtraction at 38.5 cm in the second argon fill. The x axis is PE and the y axis is (counts/bin)/second.

Figure 6.46 shows the tagged background at 38.5 cm. The tagged source rate at the peak is 195% greater than the tagged background rate at the same location.

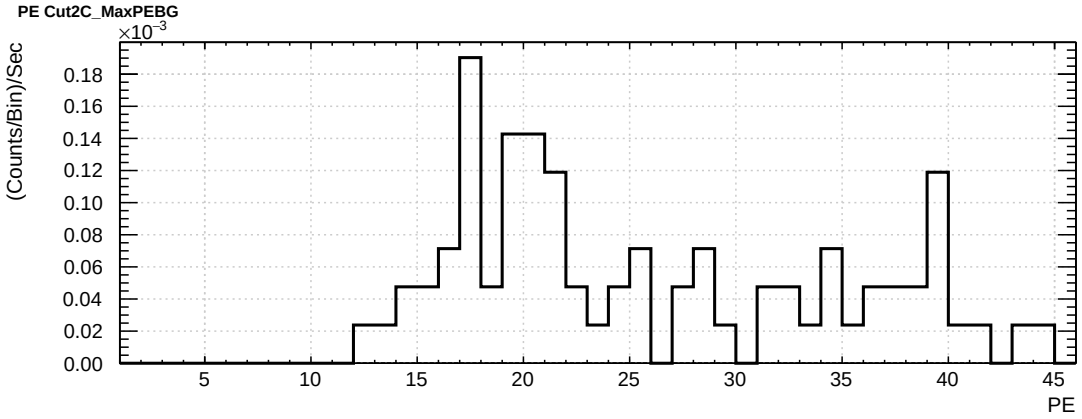

Figure 6.47: Rate normalized tagged background taken at 38.5cm in the second argon fill. The x axis is PE and the y axis is (counts/bin)/second.

Figure 6.48 shows the result of background subtracted data with all the cuts. This was used to calculate the rate integral.

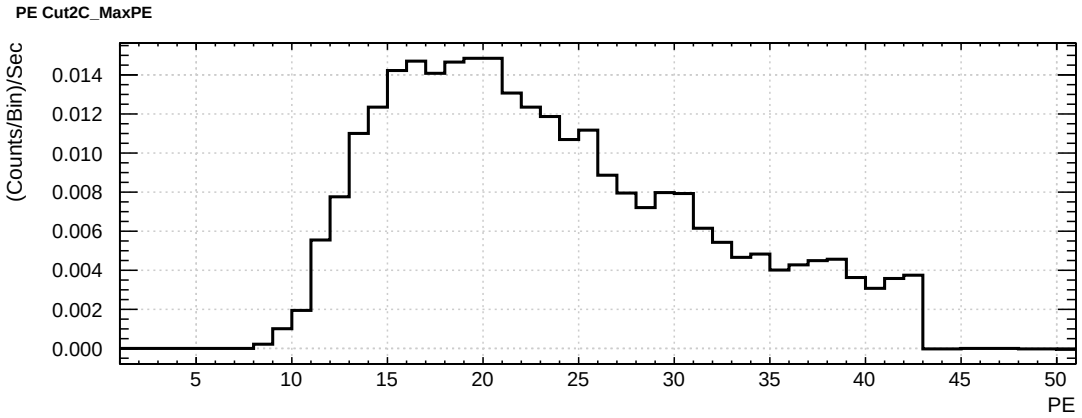

Figure 6.48: Rate normalized ^{22}Na data after cuts and and and rate normalized background subtraction at 38.5 cm in the second argon fill. The x axis is PE and the y axis is (counts/bin)/second.

Argon 3

Figure 6.49 shows the PE rate after cuts and before background subtraction at 37 cm.

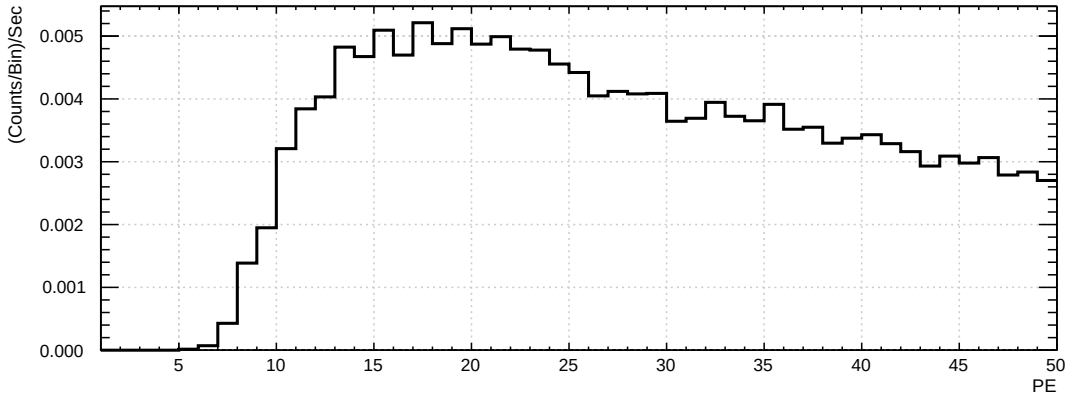

Figure 6.49: Rate normalized ^{22}Na data after cuts and before background subtraction at 37 cm in the third argon fill. The x axis is PE and the y axis is (counts/bin)/second.

Figure 6.50 shows the tagged background at 37 cm. The tagged source rate at the peak is 200% greater than the tagged background rate at the same location.

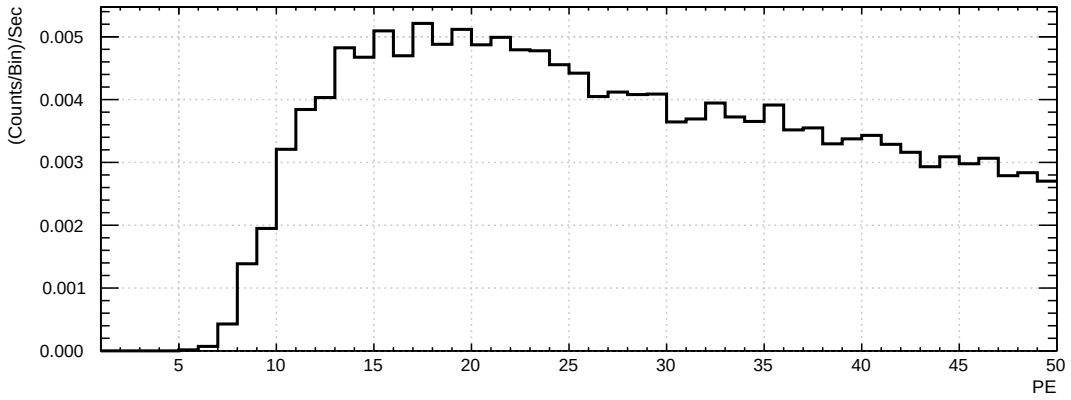

Figure 6.50: Rate normalized ^{22}Na data after cuts and before background subtraction at 37 cm in the third argon fill. The x axis is PE and the y axis is (counts/bin)/second.

Figure 6.51 shows the result of background subtracted data with all the cuts. This was used to calculate the rate integral.

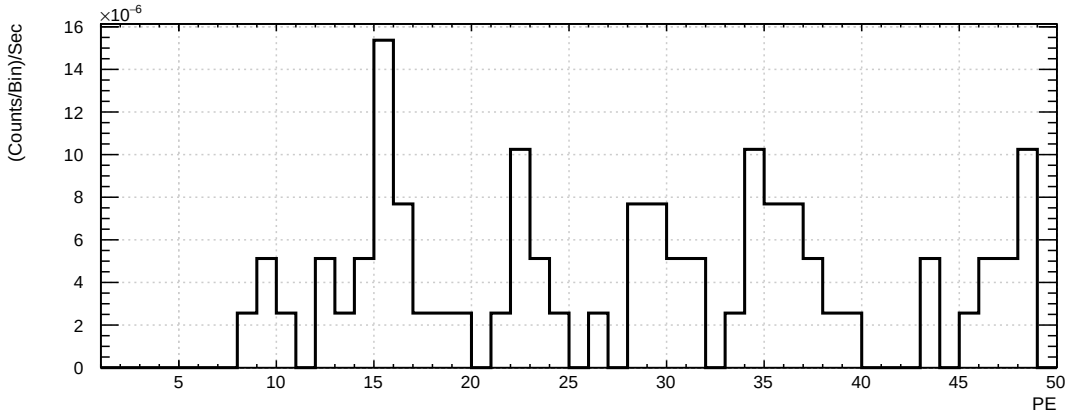

Figure 6.51: Rate normalized ^{22}Na data after cuts and before background subtraction at 37cm in the third argon fill. The x axis is PE and the y axis is (counts/bin)/second.

6.5 Rayleigh Scattering Fit

After all the cuts were applied to the data, the integral of the plots were taken for each position and plotted. These plots were then fit with Equation 4.5, from Chapter 4.

6.5.1 High Statistic Plot

The only data run with high enough statistics to make a fit was the first data run. The results from the second and third runs can be found in Appendix 2.

Time	PE Mean Position 39 cm	PE Mean Position 55 cm	PE Mean Position 71 cm
160 hr	16.9±4.8	No Data	No Data
168 hr	19.3±5.8	18.6±6.6	17.53±6.4
288 hr	18.0±8.0	17.01±5.3	15.75±5.1
309 hr	16.9±5.8	16.38±4.7	16.52±6.8

Table 6.5: PE over time in the first argon fill.

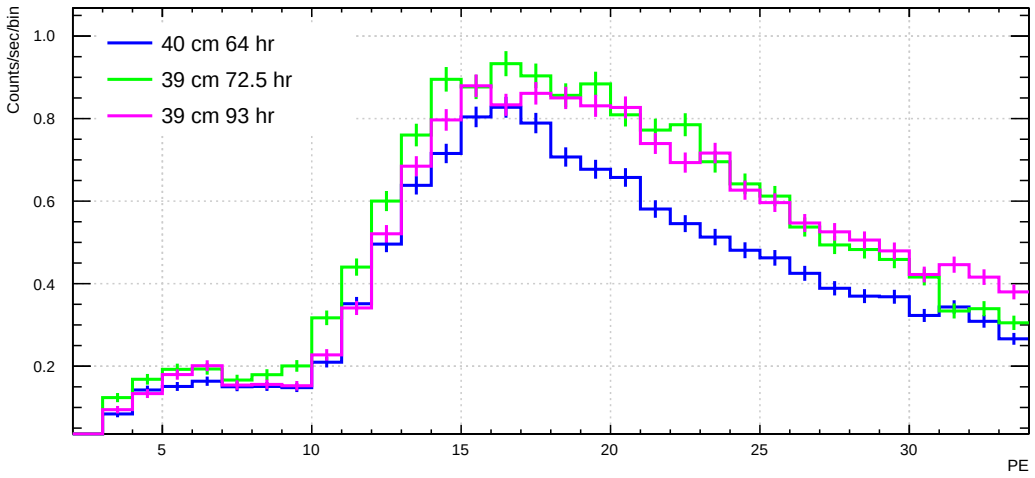

Figure 6.52: The rate integrals of data taken at 39 cm a different run times in the same argon fill (Run1). The x axis is position in centimeters and y axis is the rate integral of PE/s.

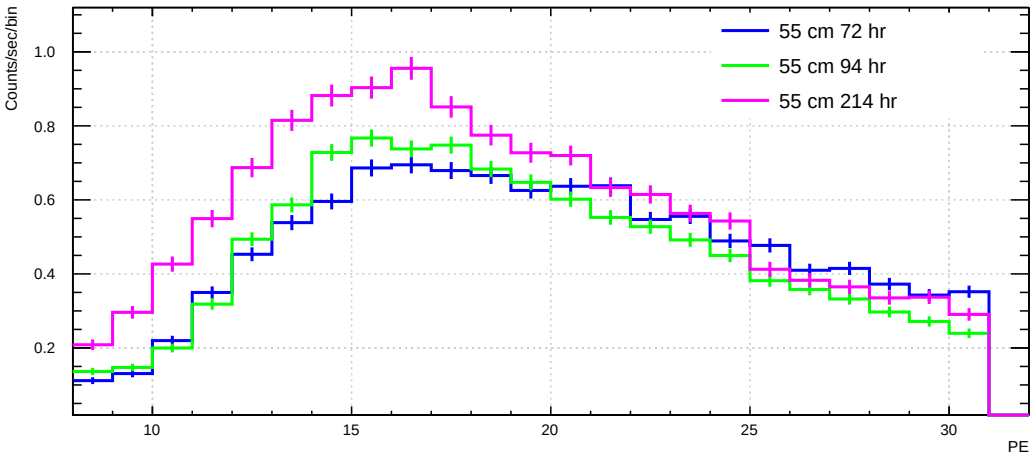

Figure 6.53: The rate integrals of data taken at 55 cm a different run times in the same argon fill (Run1). The x axis is position in centimeters and y axis is the rate integral of PE/s.

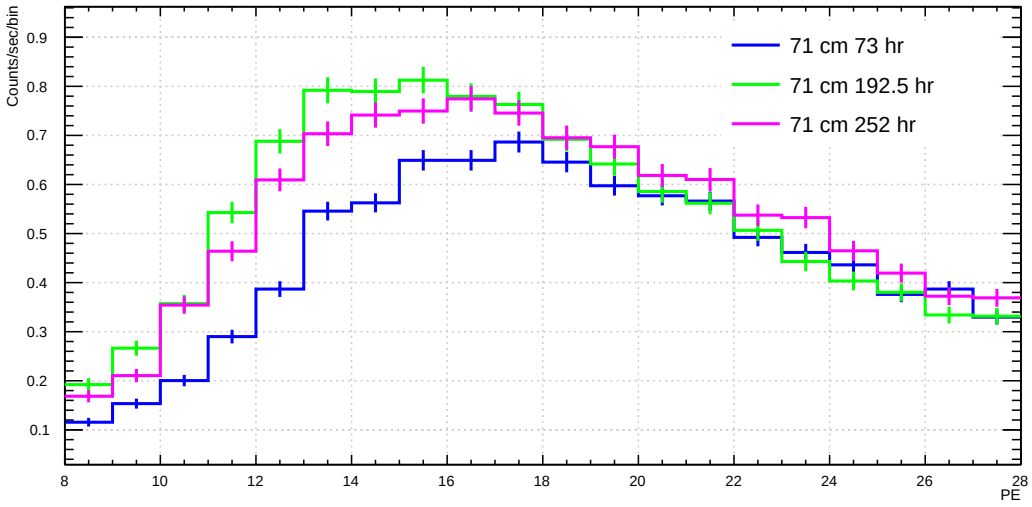

Figure 6.54: The rate integrals of data taken at 71 cm a different run times in the same argon fill (Run1). The x axis is position in centimeters and y axis is the rate integral of PE/s.

Data acquisition using an external, collimated ^{22}Na source took place over 300 hours in the first argon fill. The average temperature on the outside of the copper inner vessel was 90.19K with a range ± 1K. The average pressure was 1.317 bar with a range of ± 0.1 bar. The triplet lifetime varied 72 nanoseconds over the length of data acquisition. The error from this contribution was accounted for in the error bars on the final plot.

Thirty-three source data points and 20 background runs were acquired. The source data was filtered through a series of cuts, rate normalized, and background subtracted. The integral of this results is plotted in figure 6.55.

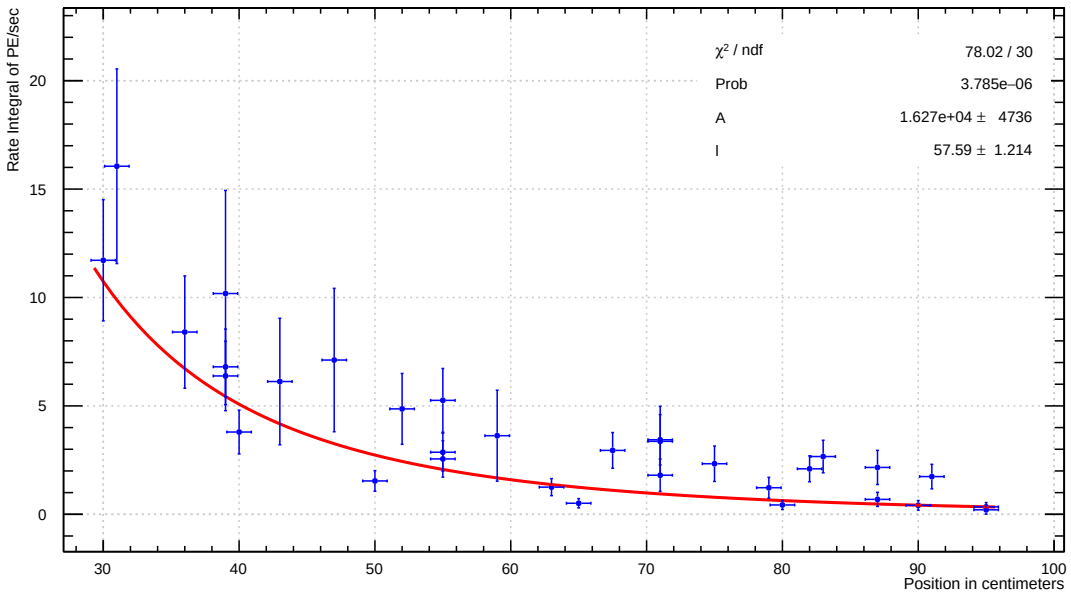

Figure 6.55: Sodium data from the first argon fill with a 4 cm front aperture. The x axis is position in centimeters and y axis is the rate integral of PE/s. This has been fit with $A/x^2e^{-l/x}$.

The error on each point was the summation of a few differentness contributions. The error on the integral from root was calculated In chapter 4, the reflection study with a 4 cm front aperture indicated a 4.3% contamination from reflection. The energy scaling varied over the run which would have result in a change in integral of 1% in the max PE cut. This is shown in Table 6.5. These errors were summed in quadrature for the error bars.

The high statistic run from the argon fill yielded a result of 58±1 cm. The χ^2/ndf of the fit is 78/30.

Chapter 7

Scattering Implications and Conclusions

When you can measure what you are speaking about, and express it in number, you know something about it.

Lord Kelvin

No one remembers the former generations, and even those yet to come will not be remembered by those who follow them.

Ecclesiastes 1:11

Thoughts are the shadows of our feelings - always darker, emptier and simpler.

Friedrich Nietzsche

7.1 Introduction

The Rayleigh scattering length of the scintillation light of liquid argon in recent scientific history was a number under contention. The measurements made by Ishida et al[122] did not agree with the calculation made by Seidel et al [104].The findings previously discussed in this thesis, both the calculation based on historical measurements and the update experimental measurement have shown the evidence needed to resolve the discrepancies. The

calculation from chapter 3 resulted in value of 60±6 cm for liquid argon. The measurement discussed in chapter 6 resulted in a value of 58±1 cm. These results are closer to the values measured by Ishida (66±3 cm) and agree within error of the value measured in situ by ArDM [133].

Source	Length
Calculations	
Seidel [104]	90cm
Chapter 3	60±6cm
Measurements	
Ishida [122]	66±3cm
ArDm [133]	52.1±5cm
Chapter 6	58± 1cm

Table 7.1: Table of Measured and Calculated Scattering Lengths

7.2 Implications of the Scattering Result in Liquid Argon Detectors

The impact of the Rayleigh scattering uncertainty is primarily in event reconstruction in argon detectors. One variable the is important to understand in both dark matter and neutrino experiments in the leakage of events from outside the the signal region to the radius that defines the signal region, or fiducial volume. A study using the DEAP detector geometry was preformed by Dr. J Walding. In this study, a RAT simulation of 20 keVee electrons were generated between 84 and 85 cm (near the detector edge) the fraction of events reconstructed in the fiducial volume ($> 55cm$) was examined. The fraction of events that reconstruct with R<55 cm varies from 0.610.04% with a Rayleigh scattering length of 90 cm (at 128 nm wavelength), to 0.48±0.04% with a Rayleigh scattering length of 66 cm. There is a fractional difference between the 90 cm and 66 cm case is 20%. The results can be seen in Figure 7.1. This can potentially improve the uncertainty in event

reconstruction by a factor of 2. This update measurement will impact the field of liquid argon detectors and event construction. In particular the detectors that are using the 90 cm scattering length.

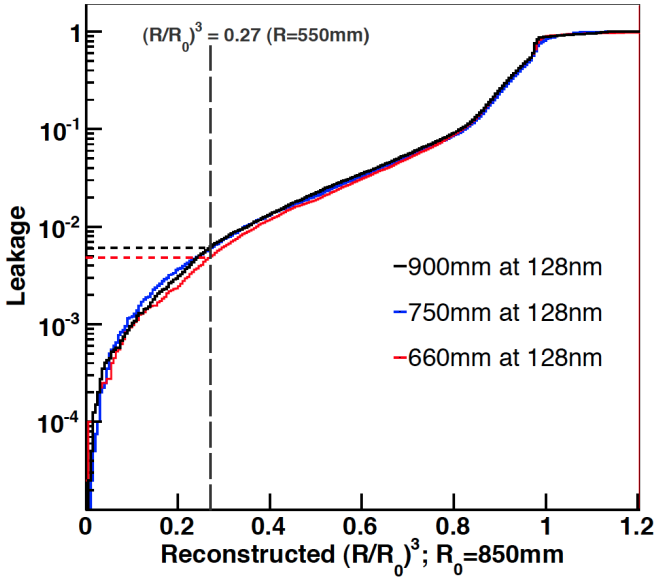

Figure 7.1: RAT simulation of 20 keV electron recoils in the DEAP-3600 detector. This details the fraction of events reconstructed inside the normalized fiducial volume radius $(R/R_0)^3$ (leakage) vs. $(R/R_0)^3$; recoils are uniformly distributed in 84-85 cm radius, for 660, 750, and 900 nm Rayleigh scattering lengths (R_0 = 85 cm). At the nominal fiducial $(R/R_0)^3$ of 0.27, the leakage differs by 20%. *Plot curtesy of J. Walding.*

7.3 Future Research

There is much to understand about the optical properties of the scintillation light of liquid argon. An additional measurement that could made is to repeat the experiment with better temperature control and to examine the scattering length at the triplet point of liquid argon. It would be interesting to understand the scattering length in a detector with a temperature gradient.

The impact of pressure and temperature on the light yield of liquid argon would be an important relationship to quantify. As liquid argon detectors grow in size, there will be a pressure gradient which could impact the signal if there is a pressure dependence for the light yield.

There is also more research to be done to understand the optical properties of solid argon. Argon can be frozen into a clear crystal with good light transmission. The light yield in solid argon is greater than liquid argon. There may interesting detector applications in the future using a solid argon medium.

7.4 Final Thoughts

In the *The Hitchhiker's Guide to the Galaxy* [168], Douglas Adams suggests that 42 is the answer to life the universe and everything. This statement is thought of as reflection of the nihilism that was pervasive throughout his writing influenced by the predominate philosophies of the past century. The readers are left to decide as to the meaning. So it is in this vane that I conclude. I have made a measurement. Its importance will be determined by the community, but any meaning it might have had outside my efforts will eventually fade. The race of which I am part of will one day die [169]. The planet we called home will eventually be destroyed [170]. The sun that gave us warmth will dim [171]. The universe that many have devoted their lives to studying will die a long and unobserved death [172]. If the physical is all there is, then nothing has meaning.

Bibliography

[1] A. C. Sinnock and B. L. Smith. Refractive indices of the condensed inert gases. *Phys. Rev.*, 181:1297–1307, May 1969.

[2] Sir Isaac Newton. *The Principia Mathematical Principles of Natural Philosophy*. University of California Press, 1999.

[3] Sir Isaac Newton. *Opticks*. Dover, 1952.

[4] M G Boulay and the Deap Collaboration. Deap-3600 dark matter search at snolab. *Journal of Physics: Conference Series*, 375(1):012027, 2012.

[5] P. Agnes et al. First results from the darkside-50 dark matter experiment at laboratori nazionali del gran sasso. *Physics Letters B*, 743:456 – 466, 2015.

[6] A Badertscher, F Bay, N Bourgeois, C Cantini, A Curioni, M Daniel, U Degunda, S Di Luise, L Epprecht, A Gendotti, et al. Ardm: first results from underground commissioning. *Journal of Instrumentation*, 8(09):C09005, 2013.

[7] Henning Back. Darkside-20k: A 20 ton liquid argon dark matter experiment. *Bulletin of the American Physical Society*, 2016.

[8] R Acciarri, MA Acero, M Adamowski, C Adams, P Adamson, S Adhikari, Z Ahmad, CH Albright, T Alion, E Amador, et al. Long-baseline neutrino facility (lbnf) and

deep underground neutrino experiment (dune) conceptual design report, volume 4 the dune detectors at lbnf. *arXiv preprint arXiv:1601.02984*, 2016.

[9] F. Zwicky. On the masses of nebulae and of clusters of nebulae. *Astrophysical Journal*, 86:217–246, 1937.

[10] Fritz Zwicky. Die rotverschiebung von extragalaktischen nebeln. *Helvetica Physica Acta*, 6:110–127, 1933.

[11] Edwin Powell Hubble. Distribution of luminosity in elliptical nebulae. *The Astrophysical Journal*, 71, 1930.

[12] Francis G Pease. The rotation and radial velocity of the spiral nebula ngc 4594. *Proceedings of the National Academy of Sciences*, 2(9):517–521, 1916.

[13] R. Clausius. Xvi. on a mechanical theorem applicable to heat. *Philosophical Magazine*, 40(265):122–127, 1870.

[14] L. Jenkins, A. Hornschemeier, et al. Dwarf galaxies in the coma cluster, 2015.

[15] W. K. Ford V. C. Rubin, N. Thonnard. Extended rotation curves of high-luminosity spiral galaxies. iv - systematic dynamical properties, sa through sc. *The Astrophysical Journal*, 1978.

[16] V. C. Rubin, W. K. J. Ford, and N. . Thonnard. Rotational properties of 21 SC galaxies with a large range of luminosities and radii, from NGC 4605 /R = 4kpc/ to UGC 2885 /R = 122 kpc/. *Astrophysical Journal*, 238:471–487, June 1980.

[17] Rubbia Andr. Ardm: a ton-scale liquid argon experiment for direct detection of dark matter in the universe. *Journal of Physics: Conference Series*, 39(1):129, 2006.

[18] A Einstein. Grundlage der Allgemeinen Relativittstheorie. *Annalen der Physik*, 49:769 – 822, 1916.

[19] Frank W Dyson, Arthur S Eddington, and Charles Davidson. A determination of the deflection of light by the sun's gravitational field, from observations made at the total eclipse of may 29, 1919. *Philosophical Transactions of the Royal Society of London A: Mathematical, Physical and Engineering Sciences*, 220(571-581):291–333, 1920.

[20] D. Walsh, R. F. Carswell, and R. J. Weymann. 0957 + 561 A, B - Twin quasistellar objects or gravitational lens. *Nature*, 279:381–384, May 1979.

[21] J. Anthony Tyson, Greg P. Kochanski, and Ian P. Dell'Antonio. Detailed mass map of cl 0024+1654 from strong lensing. *The Astrophysical Journal Letters*, 498(2):L107, 1998.

[22] Douglas Clowe, Marua Brada, Anthony H. Gonzalez, Maxim Markevitch, Scott W. Randall, Christine Jones, and Dennis Zaritsky. A direct empirical proof of the existence of dark matter. *The Astrophysical Journal Letters*, 648(2):L109, 2006.

[23] M. Markevitch. Chandra observation of the most interesting cluster in the Universe. In *http://arxiv.org/pdf/astro-ph/0511345v1.pdf*, November 2005.

[24] Simon DM White, Julio F Navarro, August E Evrard, and Carlos S Frenk. The baryon content of galaxy clusters: a challenge to cosmological orthodoxy. *Nature*, 366(6454):429–433, 1993.

[25] M Fukugita, CJ Hogan, and PJE Peebles. The cosmic baryon budget. *The Astrophysical Journal*, 503(2):518, 1998.

[26] NASA. The matter of the bullet cluster, 2006.

[27] G. F. Smoot, C. L. Bennett, A. Kogut, E. L. Wright, J. Aymon, N. W. Boggess, E. S. Cheng, G. de Amici, S. Gulkis, M. G. Hauser, G. Hinshaw, P. D. Jackson, M. Janssen, E. Kaita, T. Kelsall, P. Keegstra, C. Lineweaver, K. Loewenstein, P. Lubin, J. Mather, S. S. Meyer, S. H. Moseley, T. Murdock, L. Rokke, R. F. Silverberg, L. Tenorio, R. Weiss, and D. T. Wilkinson. Structure in the COBE differential microwave radiometer first-year maps. *Astrophysical Journal*, 396:L1–L5, September 1992.

[28] C. L. Bennett, D. Larson, J. L. Weiland, N. Jarosik, G. Hinshaw, N. Odegard, K. M. Smith, R. S. Hill, B. Gold, M. Halpern, E. Komatsu, M. R. Nolta, L. Page, D. N. Spergel, E. Wollack, J. Dunkley, A. Kogut, M. Limon, S. S. Meyer, G. S. Tucker, and E. L. Wright. Nine-year wilkinson microwave anisotropy probe (wmap) observations: Final maps and results. *The Astrophysical Journal Supplement Series*, 208(2):20, 2013.

[29] PAR Ade, N Aghanim, C Armitage-Caplan, M Arnaud, M Ashdown, F Atrio-Barandela, J Aumont, C Baccigalupi, AJ Banday, RB Barreiro, et al. Planck 2013 results. xxiii. isotropy and statistics of the cmb. *Astronomy & Astrophysics*, 571:A23, 2014.

[30] G Hinshaw, D Larson, E Komatsu, DN Spergel, CL Bennett, J Dunkley, MR Nolta, M Halpern, RS Hill, N Odegard, et al. Nine-year wilkinson microwave anisotropy probe (wmap) observations: cosmological parameter results. *The Astrophysical Journal Supplement Series*, 208(2):19, 2013.

[31] Robert R Caldwell. A phantom menace? cosmological consequences of a dark energy component with super-negative equation of state. *Physics Letters B*, 545(1):23–29, 2002.

[32] M. Milgrom. A modification of the Newtonian dynamics as a possible alternative to the hidden mass hypothesis. *Astrophysical Journal*, 270:365–370, July 1983.

[33] B Qin, XP Wu, and ZL Zou. An attempt to empirically evaluate the gravitational deflection of light in the modified newtonian dynamics. *Astronomy and Astrophysics*, 296:264, 1995.

[34] Stacy S McGaugh. A tale of two paradigms: the mutual incommensurability of λcdm and mond 1. *Canadian Journal of Physics*, 93(2):250–259, 2014.

[35] Ch Alcock, RA Allsman, D Alves, TS Axelrod, AC Becker, DP Bennett, KH Cook, KC Freeman, K Griest, J Guern, et al. The macho project: limits on planetary mass dark matter in the galactic halo from gravitational microlensing. *The Astrophysical Journal*, 471(2):774, 1996.

[36] Cecile Renault, C Afonso, E Aubourg, P Bareyre, F Bauer, S Brehin, C Coutures, C Gaucherel, JF Glicenstein, B Goldman, et al. Observational limits on machos in the galactic halo. *arXiv preprint astro-ph/9612102*, 1996.

[37] Bohdan Paczynski. Gravitational microlensing by the galactic halo. *The Astrophysical Journal*, 304:1–5, 1986.

[38] Ch Alcock, RA Allsman, D Alves, R Ansari, E Aubourg, TS Axelrod, P Bareyre, J-Ph Beaulieu, AC Becker, DP Bennett, et al. Eros and macho combined limits on

planetary-mass dark matter in the galactic halo. *The Astrophysical Journal Letters*, 499(1):L9, 1998.

[39] Donald Perkins. *Particle Astrophysics*. Oxford University Press, 2nd edition, 2013.

[40] Wolfgang Pauli. On the conservation of the lepton charge. *Il Nuovo Cimento (1955-1965)*, 6(1):204–215, 1957.

[41] Frederick Reines and Clyde L Cowan Jr. Free antineutrino absorption cross section. i. measurement of the free antineutrino absorption cross section by protons. *Physical Review*, 113(1):273, 1959.

[42] Raymond Davis Jr, Don S Harmer, and Kenneth C Hoffman. Search for neutrinos from the sun. *Physical Review Letters*, 20(21):1205, 1968.

[43] John N Bahcall, Neta A Bahcall, and Giora Shaviv. Present status of the theoretical predictions for the cl 37 solar-neutrino experiment. *Physical Review Letters*, 20(21):1209, 1968.

[44] V Gribov and B Pontecorvo. Neutrino astronomy and lepton charge. *Physics Letters B*, 28(7):493–496, 1969.

[45] D Griffiths. *Introduction to Elementary Particles*. Wiley-VCH, 2 edition, 2008.

[46]

[47] AG Doroshkevich, M Yu Khlopov, RA Sunyaev, AS Szalay, and Ya B Zeldovich. Cosmological impact of the neutrino rest mass. *Annals of the New York Academy of Sciences*, 375(1):32–42, 1981.

[48] Ia B Zeldovich, J Einasto, and SF Shandarin. Giant voids in the universe. *Nature*, 300:407–413, 1982.

[49] Simon DM White, CS Frenk, and Marc Davis. Clustering in a neutrino-dominated universe. *The Astrophysical Journal*, 274:L1–L5, 1983.

[50] Motoi Endo, Masahiro Yamaguchi, and Koichi Yoshioka. Bottom-up approach to moduli dynamics in heavy gravitino scenario: Superpotential, soft terms, and sparticle mass spectrum. *Physical Review D*, 72(1):015004, 2005.

[51] Michael Dine, Willy Fischler, and Mark Srednicki. A simple solution to the strong cp problem with a harmless axion. *Physics letters B*, 104(3):199–202, 1981.

[52] Marc Kamionkowski and John March-Russell. Planck-scale physics and the peccei-quinn mechanism. *Physics Letters B*, 282(1):137–141, 1992.

[53] Dan Hooper and Lisa Goodenough. Dark matter annihilation in the galactic center as seen by the fermi gamma ray space telescope. *Physics Letters B*, 697(5):412–428, 2011.

[54] Patrick J Fox, Roni Harnik, Joachim Kopp, and Yuhsin Tsai. Missing energy signatures of dark matter at the lhc. *Physical Review D*, 85(5):056011, 2012.

[55] Antonio Boveia, Oliver Buchmueller, Giorgio Busoni, Francesco D'Eramo, Albert De Roeck, Andrea De Simone, Caterina Doglioni, Matthew J Dolan, Marie-Helene Genest, Kristian Hahn, et al. Recommendations on presenting lhc searches for missing transverse energy signals using simplified s-channel models of dark matter. *arXiv preprint arXiv:1603.04156*, 2016.

[56] Ulrich Haisch, Felix Kahlhoefer, and James Unwin. The impact of heavy-quark loops on lhc dark matter searches. *arXiv preprint arXiv:1208.4605*, 2012.

[57] P Cushman, C Galbiati, DN McKinsey, H Robertson, TMP Tait, D Bauer, A Borgland, B Cabrera, F Calaprice, J Cooley, et al. Snowmass cf1 summary: Wimp dark matter direct detection. *arXiv preprint arXiv:1310.8327*, 2013.

[58] Tarek Saab. An introduction to dark matter direct detection searches & techniques. *arXiv preprint arXiv:1203.2566*, 2012.

[59] Z Ahmed, DS Akerib, S Arrenberg, CN Bailey, D Balakishiyeva, L Baudis, DA Bauer, PL Brink, T Bruch, R Bunker, et al. Dark matter search results from the cdms ii experiment. *Science (New York, NY)*, 327(5973):1619–1621, 2010.

[60] B Censier. Final results of the edelweiss-i dark matter search with cryogenic heat-and-ionization ge detectors. *Nuclear Instruments and Methods in Physics Research Section A: Accelerators, Spectrometers, Detectors and Associated Equipment*, 559(2):381–383, 2006.

[61] Craig E Aalseth, PS Barbeau, NS Bowden, B Cabrera-Palmer, J Colaresi, JI Collar, S Dazeley, P De Lurgio, James E Fast, N Fields, et al. Results from a search for light-mass dark matter with a p-type point contact germanium detector. *Physical Review Letters*, 106(13):131301, 2011.

[62] Godehard Angloher, M Bauer, I Bavykina, A Bento, C Bucci, C Ciemniak, G Deuter, F von Feilitzsch, D Hauff, P Huff, et al. Results from 730 kg days of the cresst-ii dark matter search. *The European Physical Journal C*, 72(4):1–22, 2012.

[63] Wei Zhao, Qian Yue, Ke-Jun Kang, JP Cheng, YJ Li, ST Lin, Y Bai, Y Bi, JP Chang, N Chen, et al. First results on low-mass wimps from the cdex-1 experiment at the china jinping underground laboratory. *Physical Review D*, 88(5):052004, 2013.

[64] R Bernabei, P Belli, F Cappella, R Cerulli, CJ Dai, A d?Angelo, HL He, A Incicchitti, HH Kuang, XH Ma, et al. New results from dama/libra. *The European Physical Journal C*, 67(1-2):39–49, 2010.

[65] S Archambault, E Behnke, P Bhattacharjee, S Bhattacharya, X Dai, M Das, A Davour, F Debris, N Dhungana, J Farine, et al. Constraints on low-mass wimp interactions on 19 f from picasso. *Physics Letters B*, 711(2):153–161, 2012.

[66] E Behnke, J Behnke, SJ Brice, D Broemmelsiek, JI Collar, A Conner, PS Cooper, M Crisler, CE Dahl, D Fustin, et al. First dark matter search results from a 4-kg cf 3 i bubble chamber operated in a deep underground site. *Physical Review D*, 86(5):052001, 2012.

[67] C Amole, M Ardid, David M Asner, D Baxter, E Behnke, P Bhattacharjee, H Borsodi, Manuel Bou-Cabo, SJ Brice, D Broemmelsiek, et al. Dark matter search results from the pico-2l c 3 f 8 bubble chamber. *Physical review letters*, 114(23):231302, 2015.

[68] E Aprile, M Alfonsi, K Arisaka, F Arneodo, C Balan, L Baudis, B Bauermeister, A Behrens, P Beltrame, K Bokeloh, et al. Dark matter results from 225 live days of xenon100 data. *Physical review letters*, 109(18):181301, 2012.

[69] DS Akerib, HM Araujo, X Bai, AJ Bailey, J Balajthy, S Bedikian, E Bernard, A Bernstein, A Bolozdynya, A Bradley, et al. First results from the lux dark matter

experiment at the sanford underground research facility. *Physical Review Letters*, 112(9):091303, 2014.

[70] DC Malling, DS Akerib, HM Araujo, X Bai, S Bedikian, E Bernard, A Bernstein, A Bradley, SB Cahn, MC Carmona-Benitez, et al. After lux: the lz program. *arXiv preprint arXiv:1110.0103*, 2011.

[71] P. Agnes et al. Results from the first use of low radioactivity argon in a dark matter search. *Phys. Rev. D*, 93:081101, Apr 2016.

[72] A Marchionni, C Amsler, A Badertscher, V Boccone, A Bueno, MC Carmona-Benitez, J Coleman, W Creus, A Curioni, M Daniel, et al. Ardm: a ton-scale lar detector for direct dark matter searches. In *Journal of Physics: Conference Series*, volume 308, page 012006. IOP Publishing, 2011.

[73] Keith Rielage, M Akashi-Ronquest, M Bodmer, R Bourque, B Buck, A Butcher, T Caldwell, Y Chen, K Coakley, E Flores, et al. Update on the miniclean dark matter experiment. *Physics Procedia*, 61:144–152, 2015.

[74] DN McKinsey, Mini-CLEAN Collaboration, et al. The mini-clean experiment. *Nuclear Physics B-Proceedings Supplements*, 173:152–155, 2007.

[75] P Gorel. Search for dark matter with liquid argon and pulse shape discrimination: Results from deap-1 and status of deap-3600. *arXiv preprint arXiv:1406.0462*, 2014.

[76] Lord Rayleigh and William Ramsay. Argon, a new constituent of the atmosphere. *Proceedings of the Royal Society of London*, 57(340-346):265–287, 1894.

[77] E R Dobbs and G O Jones. Theory and properties of solid argon. *Reports on Progress in Physics*, 20(1):516, 1957.

[78] P.J. Linstrom and W.G. Mallard. *NIST Chemistry WebBook, NIST Standard Reference Database*. National Institute of Standards and Technology, 69 edition, 2016.

[79] Jeffrey L Briesacher, Charles H Applegarth, and H Lorimer D'Arcy. Method and apparatus for removing residual hydrogen from a purified gas, August 24 1993. US Patent 5,238,469.

[80] Jeffrey L Briesacher, Masakazu Nakamura, and Tadahiro Ohmi. Gas purification and measurement at the ppt level. *Journal of the Electrochemical Society*, 138(12):3717–3723, 1991.

[81] Saes Pure Gas Inc. Monotorr brochure: Heated getter gas purifiers, 2010.

[82] M.K. Harrison, W.H. Lippincott, D.N. McKinsey, and J.A. Nikkel. Use of activated charcoal for the purification of neon in the {CLEAN} experiment. *Nuclear Instruments and Methods in Physics Research Section A: Accelerators, Spectrometers, Detectors and Associated Equipment*, 570(3):556 – 560, 2007.

[83] E. Aprile, A.E. Bolotnikoc, A.I. Bolozdynaya, and T. Doke. *Noble Gas Detectors*. Wiley-VCH, 1 edition, 2006.

[84] Joshua Jortner, Lothar Meyer, Stuart A. Rice, and E. G. Wilson. Localized excitations in condensed ne, ar, kr, and xe. *The Journal of Chemical Physics*, 42(12):4250–4253, 1965.

[85] Chemicool Periodic Table. Elements, 2012.

[86] H.H. Loosli. A dating method with 39 ar. *Earth and Planetary Science Letters*, 63(1):51 – 62, 1983.

[87] R. W. Stoenner, O. A. Schaeffer, and S. Katcoff. Half-lives of argon-37, argon-39, and argon-42. *Science*, 148(3675):1325–1328, 1965.

[88] A. R. Brosi, H. Zeldes, and B. H. Ketelle. argon^{39} beta-spectrum. *Phys. Rev.*, 79:902–902, Sep 1950.

[89] A. Gedanken, J. Jortner, B. Raz, and A. Szöke. Electronic Energy Transfer Phenomena in Rare Gases. *The Journal of Chemical Physics*, 57:3456–3469, October 1972.

[90] Tadayoshi Doke, Akira Hitachi, Jun Kikuchi, Kimiaki Masuda, Hiroyuki Okada, and Eido Shibamura. Absolute scintillation yields in liquid argon and xenon for various particles. *Japanese Journal of Applied Physics*, 41(3R):1538, 2002.

[91] Akira Hitachi, Tan Takahashi, Nobutaka Funayama, Kimiaki Masuda, Jun Kikuchi, and Tadayoshi Doke. Effect of ionization density on the time dependence of luminescence from liquid argon and xenon. *Phys. Rev. B*, 27:5279–5285, May 1983.

[92] M.G. Boulay and A. Hime. Technique for direct detection of weakly interacting massive particles using scintillation time discrimination in liquid argon. *Astroparticle Physics*, 25(3):179 – 182, 2006.

[93] DN McKinsey and JM Doyle. Liquid helium and liquid neon-sensitive, low background scintillation media for the detection of low energy neutrinos. *Journal of Low Temperature Physics*, 118(3-4):153–165, 2000.

[94] JS Adams, YH Kim, RE Lanou, HJ Maris, and GM Seidel. Scintillation and quantum evaporation generated by single monoenergetic electrons stopped in superfluid helium. *Journal of low temperature physics*, 113(5-6):1121–1128, 1998.

[95] W.G Richards, H.P. Trivedi, and D.L. Cooper. *Spin-Orbit Coupling in Molecules*. Clarendon Press, 1981.

[96] T. Doke, H. J. Crawford, A. Hitachi, J. Kikuchi, P. J. Lindstrom, K. Masuda, E. Shibamura, and T. Takahashi. Let dependence of scintillation yields in liquid argon. *Nuclear Instruments and Methods in Physics Research A*, 269:291–296, June 1988.

[97] W.H. Lippincott et al. Scintillation time dependence and pulse shape discrimination in liquid argon. *Phys. Rev.*, C78:035801, 2008. [Erratum: Phys. Rev.C81,039901(2010)].

[98] Lord Rayleigh. On the transmission of light through an atmosphere containing small particles in suspension, and on the origin of the blue of the sky. *Philos Mag.*, 47, 1899.

[99] L.D Landau and E.M. Lifshitz. *Electrodynamics of Continuous Media*, volume 8. Pergamon Press, 1960.

[100] A Morel. Optical properties of pure water and pure sea water. *Optical aspects of oceanography*, 1, 1974.

[101] Marcel Nicolet. On the molecular scattering in the terrestrial atmosphere: An empirical formula for its calculation in the homosphere. *Planetary and Space Science*, 32(11):1467–1468, 1984.

[102] Hans Naus and Wim Ubachs. Experimental verification of rayleigh scattering cross sections. *Optics Letters*, 25(5):347–349, 2000.

[103] A. Einstein and L. Hopf. Statistische Untersuchung der Bewegung eines Resonators in einem Strahlungsfeld. *Annalen der Physik*, 338(16):1105–1115, 1910.

[104] G.M Seidel, R.E Lanou, and W Yao. Rayleigh scattering in rare-gas liquids. *arXiv:hep-ex/0111054v2*, 2002.

[105] H. A. Lorentz. Ueber die Beziehung Zwischen der Fortpflanzungsgeschwindigkeit des Lichtes und der Krperdichte. *Wiedem. Ann.*, 9:641–665, 1880.

[106] L Lorenz. Ueber das leitungsvermögen der metalle für wärme und electricität. *Annalen der Physik*, 249(7):422–447, 1881.

[107] M Born and E Wolf. *Principles of Optics*. Cambridge University Press, 7 edition, 1999.

[108] Gustav Mie. Beitrge zur Optik trber Medien, Speziell Kolloidaler Metallsungen. *Annalen der Physik*, 330(3):377–445, 1908.

[109] E. Clementi, D.L. Rainmondi, and W.P. Reinhardt. Atomic screening constants from scf functions. ii. atoms with 37 to 86 electrons. *Journal of Chemical Physics*, 38:2686, 1963.

[110] J.C. Slater. Atomic Radii in Crystals. *Journal of Chemical Physics*, 41:3199–3204, November 1964.

[111] Alexander Fladerer and Reinhard Strey. Homogeneous nucleation and droplet growth in supersaturated argon vapor: The cryogenic nucleation pulse chamber. *The Journal of chemical physics*, 124(16):164710, 2006.

[112] R. E. Huffman, Y. Tanaka, and J. C. Larrabee. Absorption coefficients of krypton in the 600 to 886 å wavelength region. *Appl. Opt.*, 2(9):947–953, Sep 1963.

[113] Giancarlo Baldini. Ultraviolet absorption of solid argon, krypton, and xenon. *Phys. Rev.*, 128:1562–1567, Nov 1962.

[114] K Mavrokoridis et al. Argon Purification Studies and a Novel Liquid Argon Recirculation System. In *arxiv.org/pdf/1106.5226v1.pdf*, June 2011.

[115] P. Govoni, P.S. Marrocchesi, F.-L. Navarria, M. Paganoni, A. Perrotta, R. Acciarri, M. Antonello, B. Baibussinov, M. Baldo-Ceolin, P. Benetti, F. Calaprice, E. Calligarich, M. Cambiaghi, N. Canci, F. Carbonara, F. Cavanna, S. Centro, A.G. Cocco, F. Di Pompeo, G. Fiorillo, C. Galbiati, V. Gallo, L. Grandi, G. Meng, I. Modena, C. Montanari, O. Palamara, L. Pandola, F. Pietropaolo, G.L. Raselli, M. Roncadelli, M. Rossella, C. Rubbia, E. Segreto, A.M. Szelc, F. Tortorici, S. Ventura, and C. Vignoli. 11th topical seminar on innovative particle and radiation detectors (iprd08) effects of nitrogen and oxygen contamination in liquid argon. *Nuclear Physics B - Proceedings Supplements*, 197(1):70 – 73, 2009.

[116] R Acciarri, M Antonello, B Baibussinov, M Baldo-Ceolin, P Benetti, F Calaprice, E Calligarich, M Cambiaghi, N Canci, F Carbonara, F Cavanna, S Centro, A G Cocco, F Di Pompeo, G Fiorillo, C Galbiati, V Gallo, L Grandi, G Meng, I Modena, C Montanari, O Palamara, L Pandola, G B Piano Mortari, F Pietropaolo, G L Raselli, M Roncadelli, M Rossella, C Rubbia, E Segreto, A M Szelc, F Tortorici, S Ventura, and C Vignoli. Oxygen contamination in liquid argon: combined effects on ionization electron charge and scintillation light. *Journal of Instrumentation*, 5(05):P05003, 2010.

[117] W. M. Burton and B. A. Powell. Fluorescence of tetraphenyl-butadiene in the vacuum ultraviolet. *Appl. Opt.*, 12(1):87–89, Jan 1973.

[118] Trinh Thi Hoang Mai and R Drouin. Relative quantum efficiencies of some ultraviolet scintillators. *Applied optics*, 10(1):207_1–208, 1971.

[119] R Francini, RM Montereali, E Nichelatti, MA Vincenti, N Canci, E Segreto, F Cavanna, F Di Pompeo, F Carbonara, G Fiorillo, et al. Vuv-vis optical characterization of tetraphenyl-butadiene films on glass and specular reflector substrates from room to liquid argon temperature. *Journal of Instrumentation*, 8(09):P09006, 2013.

[120] N. Ishida, M. Chen, T. Doke, K. Hasuike, A. Hitachi, M. Gaudreau, M. Kase, Y. Kawada, J. Kikuchi, T. Komiyama, K. Kuwahara, K. Masuda, H. Okada, Y.H. Qu, M. Suzuki, and T. Takahashi. Attenuation length measurements of scintillation light in liquid rare gases and their mixtures using an improved reflection suppresser. *Nuclear Instruments and Methods in Physics Research Section A: Accelerators, Spectrometers, Detectors and Associated Equipment*, 384(23):380 – 386, 1997.

[121] P. A. Amaudruz et al. First results from the DEAP-3600 dark matter search with argon at SNOLAB. 2017.

[122] N. Ishida et al. Measurement of the attenuation length of scintillation light in liquid xenon. *Nuclear Instruments and Methods in Physics Research*, A327, 1993.

[123] Kevin J. Coakley and Daniel N. McKinsey. Spatial methods for event reconstruction in {CLEAN}. *Nuclear Instruments and Methods in Physics Research Section A: Accelerators, Spectrometers, Detectors and Associated Equipment*, 522(3):504 – 520, 2004.

[124] M.G. Boulay, A. Hime, and J. Lidgard. Design constraints for a WIMP dark matter and pp solar neutrino liquid neon scintillation detector. 2004.

[125] The MicroBooNE Collaboration. The microboone technical design report. Technical report, FermiLab, 2012.

[126] Jose Ocariz. The NA48 liquid krypton calorimeter description and performances. 1999.

[127] P Schiebener, Johannes Straub, JMH Levelt Sengers, and JS Gallagher. Refractive index of water and steam as function of wavelength, temperature and density. *Journal of physical and chemical reference data*, 19(3):677–717, 1990.

[128] B.L. Smith. *Density and Refractive Index of the Condensed Inert Gases*. PhD thesis, Queen Mary's, University of London, 1960.

[129] V.N Solovov, V Chepel, M.I Lopes, A Hitachi, R Ferreira Marques, and A.J.P.L Policarpo. Measurement of the refractive index and attenuation length of liquid xenon for its scintillation light. *Nuclear Instruments and Methods in Physics Research Section A: Accelerators, Spectrometers, Detectors and Associated Equipment*, 516(23):462 – 474, 2004.

[130] A. Bideau-Mehu. Measurement of refractive indices of neon, argon, krypton and xenon in the 253.7 140.4 nm wavelength range. dispersion relations and estimated oscillator strengths of the resonance lines. *Journal of Quantitative Spectroscopy and Radiative Transfer*, 25:395–402, may 1981.

[131] LM Barkov, AA Grebenuk, NM Ryskulov, P Yu Stepanov, and SG Zverev. Measurement of the refractive index of liquid xenon for intrinsic scintillation light. *Nuclear*

Instruments and Methods in Physics Research Section A: Accelerators, Spectrometers, Detectors and Associated Equipment, 379(3):482–483, 1996.

[132] Akira Hitachi, Vitaly Chepel, M. Isabel Lopes, and Vladimir N. Solovov. New approach to the calculation of the refractive index of liquid and solid xenon. *The Journal of Chemical Physics*, 123(23):–, 2005.

[133] J Calvo, C Cantini, P Crivelli, M Daniel, S DiLuise, A Gendotti, S Horikawa, L Molina-Bueno, B Montes, W Mu, et al. Measurement of the attenuation length of argon scintillation light in the ardm lar tpc. *arXiv preprint arXiv:1611.02481*, 2016.

[134] H.J. Achtermann et al. Experimental determination of the refractivity virial coefficients of atomic gases. *Chemical Physics*, 98, 1993.

[135] Arthur L. Lane and Aron Kuppermann. Argon resonance line lamp for vacuum ultraviolet photochemistry. *Review of Scientific Instruments*, 39(1):126–127, 1968.

[136] Shigeyoshi Arai, Takefumi Oka, Masuhiro Kogoma, and Masashi Imamura. Near infrared absorptions of neon, argon, krypton, and xenon excited diatomic molecules. *The Journal of Chemical Physics*, 68(10):4595–4603, 1978.

[137] Joel Tellinghuisen. Statistical error propagation. *Journal of Physical Chemistry A*, 105:3917 – 3921, 2001.

[138] A Beer. Determination of the absorption of red light in colored liquids. *Ann. Phys. Chem*, 86:78–88, 1852.

[139] J. van Bokhoven and C. Lamberti. *X-Ray Absorption and X-Ray Emission Spectroscopy: Theory and Applications*. Wiley, 1 edition, 2017.

[140] LLC MDC Vacuum Products. Mdc viewports: 4-5/8 inch od, 2014.

[141] D.N. McKinsey, C.R. Brome, J.S. Butterworth, R. Golub, K. Habicht, P.R. Huffman, S.K. Lamoreaux, C.E.H. Mattoni, and J.M. Doyle. Fluorescence efficiencies of thin scintillating films in the extreme ultraviolet spectral region. *Nuclear Instruments and Methods in Physics Research Section B: Beam Interactions with Materials and Atoms*, 132(3):351 – 358, 1997.

[142] LLC MDC Vacuum Products. Mdc viewports: Sapphire transmission curve, 2014.

[143] LLC MDC Vacuum Products. Mdc viewports: Glass transmission curve, 2014.

[144] Valley Design. Optical transmission of sapphire windows and disks, 2015.

[145] T. Bromwich. Tpb evaporations and sensitivity plots for the deap-3600 dark matter detector. Master's thesis, University of Sussex, 2014.

[146] Acktar Advanced Coating. Spectral black coated foil, 2014.

[147] J.H. Hubbell and S.M. Seltzer. Tables of x-ray mass attenuation coefficients and mass energy-absorption coefficients from 1 kev to 20 mev for elements z = 1 to 92 and 48 additional substances of dosimetric interest. *NIST X-ray Attenuation Databases*, 2004.

[148] S. R. Seibert. *A Low Energy Measurement of the 8B Solar Neutrino Spectrum at the Sudbury Neutrino Observatory.* PhD thesis, The University of Texas at Austin, 2008.

[149] Ren Brun, Fons Rademakers, and Cern Collaboration. Root data analysis framework: User's guide, 2014.

[150] Geant4 Collaboration. Introduction to geant4, 2015.

[151] LakeShore Cryotronics. Germanium rtd specifications, 2016.

[152] LakeShore Cryotronics. Cryogenic temperaturecontroller, 2016.

[153] AGA: A Member of Linde Group. Hiq argon 6.0 data sheet, 2016.

[154] BOC: A Member of the Linde Group. Industrial gases uk: Cylinder manifolds, 2016.

[155] Swagelok. Swagelok metering valve, 2016.

[156] Cryomech. Cryomech model pt415 cryogenic refrigerator: Installation, operation, and routine maintenance manual, 2006.

[157] Hamamatsu Photonics K. K. *Photomultiplier Tube Principle to Application: Photon is Our Business*. Hamamatsu, 1 edition, 1994.

[158] Electron Tubes. 52 mm (2") photomulitplier 9954b series data sheet, 2007.

[159] C.A.E.N. Technical information manual: Mod n625 quad linear fan in / fan out, 2004.

[160] C.A.E.N. Technical information manual: Mod n417 8 channel low threshold discriminators, 1996.

[161] C.A.E.N. Technical information manual: V1720 digitizer, 2014.

[162] D. Cester, G. Nebbia, L. Stevanato, G. Viesti, F. Neri, S. Petrucci, S. Selmi, and C. Tintori. High rate read-out of labr(ce) scintillator with the caen v1720 fadc. *AIP Conference Proceedings*, 1423(1):441–445, 2012.

[163] LeCory Corporation. 365al dual 4-fold majority logic unit, 465 triple 4-fold logic unit, 622 quad 2 input logic unit, 1996.

[164] ORTEC. Electronics standards and definitions., 2016.

[165] H Farrar, AK Dasgupta, and RH Tomlinson. Half-life of cs137. *Canadian Journal of Chemistry*, 39(3):681–683, 1961.

[166] Hamamatsu. Photomultiplier tube r6091, 2016.

[167] D Griffiths. *Introduction to Electrodynamics*. PHI Learning Private Limited, 3 edition, 1999.

[168] W.R. Leo. *Techniques for Nuclear and Particle Physics Experiments: A How-to Approach*. Springer-Verlag, 2 edition, 1994.

[169] D. Adams. *The Hitchhiker's Guide to the Galaxy*. Hitchhiker's Guide to the Galaxy. Random House Publishing Group, 2007.

[170] Nick Bostrom. Existential risks: Analyzing human extinction scenarios and related hazards. 2002.

[171] Oleg Georgievich Sorokhtin, George Varos Chilingarian, and Nikolaĭ Sorokhtin. *Evolution of Earth and its climate: birth, life and death of Earth*.

[172] Kip S Thorne. Gravitational collapse and the death of a star. *Science*, 150(3704):1671–1679, 1965.

[173] Valerio Faraoni. Possible end of the universe in a finite future from dark energy with w¡- 1. *Physical Review D*, 68(6):063508, 2003.

Appendix A

Sinnock et al Data

A.1 Argon

T					λ (nm)				$\rho \times 10^{-2}$
(K)	643.9	578.0	546.1	508.6	475.3	435.8	406.3	361.2	(mol/cm^3)
Solid									
20	1.2895	1.2903	1.2910	1.2918	1.2926	1.2938	1.2950	1.2975	4.416
30	1.2879	1.2887	1.2894	1.2901	1.2909	1.2921	1.2934	1.2959	4.385
40	1.2854	1.2862	1.2869	1.2876	1.2885	1.2896	1.2909	1.2931	4.343
50	1.2822	1.2831	1.2838	1.2845	1.2853	1.2865	1.2878	1.2903	4.293
60	1.2786	1.2795	1.2801	1.2809	1.2817	1.2829	1.2841	1.2863	4.235
70	1.2742	1.2751	1.2757	1.2765	1.2773	1.2785	1.2797	1.2820	4.170
80	1.2693	1.2702	1.2708	1.2716	1.2704	1.2716	1.2728	1.2750	4.093
83.81	1.2673	1.2681	1.2688	1.2695	1.2704	1.2716	1.2728	1.2753	4.061
Liquid									
83.81	1.2321	1.2328	1.2334	1.2341	1.2349	1.2361	1.2372	1.2395	3.549
86	1.2295	1.2303	1.2308	1.2316	1.2324	1.2336	1.2347	1.2370	3.513
88	1.2274	1.2282	1.2287	1.2295	1.2303	1.2315	1.2326	1.2346	3.481
90	1.2256	1.2264	1.2269	1.2277	1.2285	1.2297	1.2308	1.2326	3.449

Table A.1: Argon Data from Sinnock and Smith [1]

A.2 Krypton

T	λ (nm)								$\rho \times 10^{-2}$
(K)	643.9	578.0	546.1	508.6	475.3	435.8	406.3	361.2	(mol/cm^3)
Solid									
67	1.3648	1.3664	1.3674	1.3688	1.3704	1.3727	1.3749	1.3787	3.542
75	1.3622	1.3638	1.3648	1.3662	1.3678	1.3701	1.3723	1.3761	3.511
85	1.3587	1.3602	1.3612	1.3627	1.3642	1.3666	1.3688	1.3726	3.471
95	1.3547	1.3562	1.3572	1.3587	1.3603	1.3626	1.3648	1.3686	3.429
105	1.3498	1.3514	1.3524	1.3538	1.3554	1.3578	1.3600	1.3638	3.383
115.95	1.3436	1.3451	1.3462	1.3476	1.3492	1.3515	1.3537	1.3576	3.330
Liquid									
115.95	1.3011	1.3024	1.3032	1.3042	1.3056	1.3074	1.3090	1.3120	2.926
118	1.2986	1.2999	1.3008	1.3017	1.3031	1.3049	1.3065	1.3095	2.906
122	1.2939	1.2952	1.2960	1.2970	1.2984	1.3002	1.3018	1.2048	2.868
126	1.2893	1.2906	1.2915	1.2924	1.2938	1.2957	1.2973	1.3003	2.829

Table A.2: Krypton Data from Sinnock and Smith [1]

A.3 Xenon

T	λ (nm)										$\rho \times 10^{-2}$
(K)	643.9	578.0	546.1	508.6	480.6	470.0	435.8	406.3	365.0	361.2	(mol/cm^3)
Solid											
80	1.4808	1.4833	1.4854	1.4882	1.4906	1.4917	1.4954	1.4995	1.5080	1.5091	2.771
90	1.4775	1.4800	1.4821	1.4848	1.4873	1.4884	1.4921	1.4962	1.5047	1.5058	2.750
100	1.4740	1.4765	1.4786	1.4814	1.4838	1.4849	1.4886	1.4927	1.5012	1.5024	2.730
110	1.4701	1.4727	1.4748	1.4775	1.4800	1.4811	1.4848	1.4889	1.4974	1.4986	2.709
120	1.4660	1.4686	1.4706	1.4734	1.4759	1.4770	1.4807	1.4848	1.4934	1.4945	2.687
130	1.4616	1.4641	1.4662	1.4690	1.4715	1.4726	1.4763	1.4804	1.4890	1.4901	2.664
140	1.4569	1.4594	1.4616	1.4643	1.4668	1.4679	1.4716	1.4757	1.4843	1.4855	2.640
150	1.4520	1.4545	1.4566	1.4594	1.4619	1.4629	1.4667	1.4708	1.4794	1.4805	2.615
161.35	1.4461	1.4486	1.4507	1.4535	1.4560	1.4571	1.4608	1.4650	1.4736	1.4747	2.585
Liquid											
161.35	1.3876	1.3900	1.3918	1.3937	1.3957	1.3967	1.4001	1.4041	1.4103	1.4111	2.272
166	1.3830	1.3853	1.3871	1.3891	1.3911	1.3921	1.3955	1.3995	1.4057	1.4065	2.244
170	1.3790	1.3814	1.3832	1.3851	1.3872	1.3882	1.3916	1.3956	1.4017	1.4025	2.221
174	1.3748	1.3772	1.3790	1.3809	1.3830	1.3840	1.3874	1.3914	1.3976	1.3984	2.198
178	1.3708	1.3732	1.3750	1.3770	1.3790	1.3800	1.3834	1.3874	1.3936	1.3944	2.176

Table A.3: Xenon Data from Sinnock and Smith [1]

Appendix B

Data from Additional Data Runs

B.1 Other Data Runs

Additional data was taken which was useful in better understanding the result.

B.1.1 Untagged

In the first argon fill, the initial data acquisition was done with the ^{137}Cs source. This source did not have a high enough activity rate compared to the background rate in the far end of the detector. However it was useful to check the energy comparison of simulation. The results agreed with the data in the high statistics data run as seen in Figure B.1.

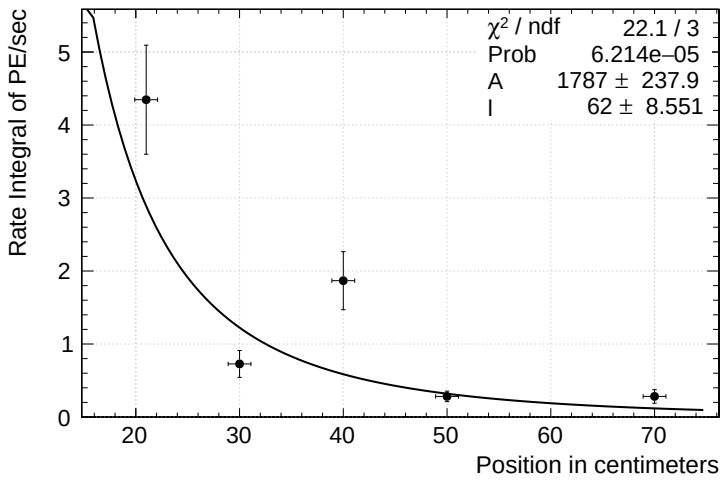

Figure B.1: ^{37}Cs Data From Second Argon Fill. The x axis is position in cm and the y axis is integral of PE/sec.

Before taking tagged data in the second argon fill, 4 untagged data points were taken with the 2cm baffle. This is useful to see if they untagged data in the second argon fill had the same form of the high statistic data run. It did have the same form as seen in Figure B.2

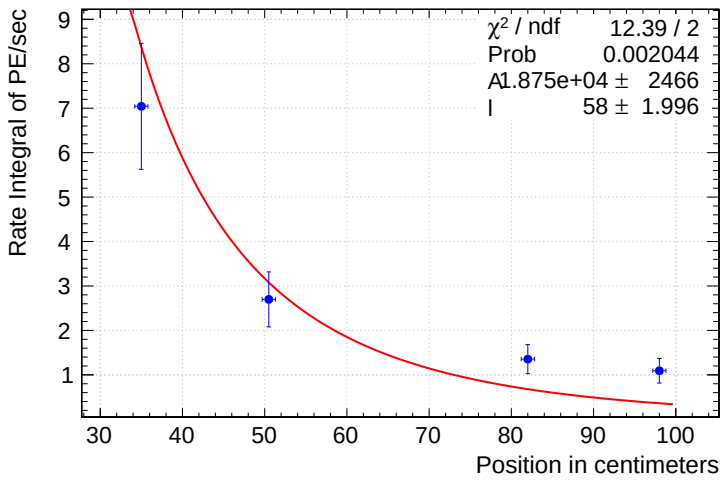

Figure B.2: ^{22}Na Data From Second Argon Fill. The x axis is position in cm and the y axis is integral of PE/sec.

B.1.2 Tagged

The tagging runs were used to better stand background contributions. After cuts, only 3% of events survived. This data points contained 50,000 waveforms instead of 200,000. So the statistics were insufficient to make a fit. However these runs were useful in understanding the cosmic ray background. This served as a further motivation to eliminate events with a high PE count, as these corresponded to the signal of a tagged background event. The tagged results from the second argon fill are found in B.3.

The tagged data in the third argon fill also had a low survival rate for cuts. Only 2% of events survived cuts. The small baffle greatly reduced the signal from each data set. Further, there a large spread in rate over time. This may have been caused by the instability of the voltage of the power supply. The results are in B.4. To improve the result, the experiment could be repeated with a different supply and more data.

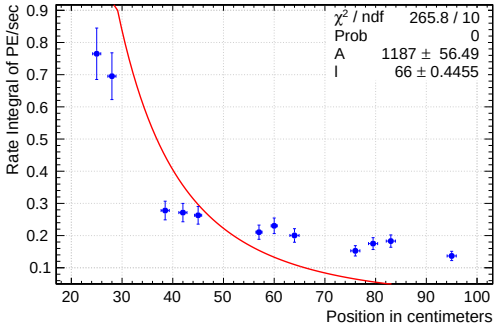

Figure B.3: Tagged data from the second argon fill with a 2cm baffle. The x axis is position in cm and the y axis is integral of PE/sec.

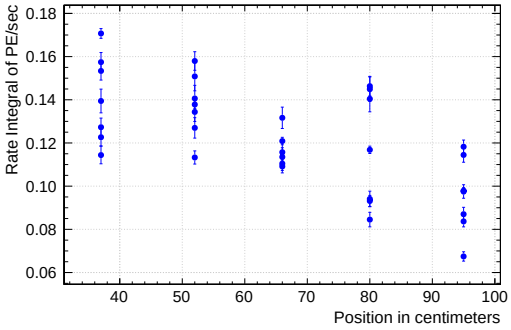

Figure B.4: Tagged data from the third argon fill with 0.5 cm baffle. The x axis is position in cm and the y axis is integral of PE/sec.